Integration and Performance of the Newtonian Calibrator and IWAVE for Exploring the Laser Interferometer Gravitational Wave Observatory Data.

Timesh Mistry

A thesis presented for the degree of Doctor of Philosophy

Supervisor: Professor Edward J. Daw
LIGO Research Group
The University of Sheffield
United Kingdom
30 March 2022

Integration and Performance of the Newtonian Calibrator and IWAVE for Exploring the Laser Interferometer Gravitational Wave Observatory Data.

Timesh Mistry

Abstract

Upgrades to IWAVE, a frequency tracking tool invented by Edward J. Daw at the University of Sheffield, has expanded the utility of the tool. Resonant characteristics observed in the Laser Interferometer Gravitational Wave Observatories - such as violin modes, test mass body modes and calibration signals - can be resolved accurately, even in tightly packed regions of frequency space using a multi-line tracker in real-time on the LIGO front end.

Furthermore, using IWAVE to develop test mass thermometers, real-time estimates of the test mass temperature is available, useful for thermal tuning of LIGO. This is achieved by tracking and calibrating test mass body modes, a coupling between the laser TEM modes and the mechanical response of the optics. The test mass thermometers can be extrapolated into a larger thermal monitoring pipeline useful for current and future gravitation wave observatory thermal modelling.

The LIGO calibration is a complicated folding of the many control systems noise sources that affect the interferometer. Presented here is the installation, commissioning and successful operation of the LIGO Hanford Newtonian Calibrator - a new R&D effort with the University of Washington that uses a spinning constellation of masses - to induce length changes in the interferometer arms by applying a small force to the test mass. These forces are modelled with three realisations of Newton Law of Gravity and all show good agreement to one another.

Statement of Work

The overarching bulk of the work is the demonstration of and improvements of IWAVE resulting in the publication Daw et al.. This involved writing custom C scripts for upgrading IWAVE on the LIGO front end, using IWAVE to track various instrument resonances - both in real-time and using stored FRAME data on the LIGO data grid - and enveloping IWAVE into larger instrumentation analysis. The latter has resulted in the development of test mass thermometer of which I calibrated that are useful for thermal modelling for current and future GW observatories for room temperature and cryogenic operations.

Some of my time spent at the observatory involved assisting with day to day operation of the interferometers as well as maintenance. Mainly, these efforts were spent on weekly maintenance and R&D of the PCal; taking calibration measurements and processing the data for the calibration working group and helping the commissioners investigate lock-losses. These efforts are folded into Sun et al. and Buikema et al..

At LIGO Hanford I installed, commissioned and operated the NCal which resulted in the publication Ross et al.. This process involved working with mechanical engineers to design and evaluate the NCal mount structure as well as assist in the physical installation. Furthermore, I was tasked with configuring the electronics and software integration which involves working alongside the LHO site electronics and software engineers. In addition, working with Jason Oberling at LHO, I was able to provide an accurate measure of the NCal installed location within the LIGO global co-ordinate space and evaluated the distance of the NCal to the X-End test mass. Moreover, it was my responsibility to request interferomter time and run the NCal injection which involved liaising with LIGO commissioners, operators, run co-ordinators to ensure minimal impact with the wire group of activities and science observation time.

Acknowledgements

Joining the LIGO collaboration soon after the two breakthrough discoveries was an exciting time to join the collaboration. It has been a great privilege to spend time at both observatories and it was a truly enjoyable and humbling experience. This was possible through the LIGO Fellows program and I am grateful for the support provided by Caltech and Rick Savage. There are many great experiences of not only working at the sites, but also exploring Louisiana and Washington that will remain as fond memories for the rest of my life. It was a pleasure to work alongside the commissioners, operators, engineer, facility and outreach site staff and I would like to thank all of them for making my experience very enjoyable. I have made a great deal of friends throughout the LIGO collaboration.

In addition, would like to thank Jimmy and Denise in Louisiana. Their passion for blues music and expertise on the guitar has certainly rubbed off and I hope one day I can revisit you and hold my own in a jam session. Moreover, I cannot ignore the many wonderful Louisianian cuisines you introduced me to and I certainly will never forget my first crayfish boil.

It was a privilege to work with Carl Blair and Jeff Kissel, sharing their expertise in GW interferometery as well as experimental physics. Not only were you both solid mentors in LIGO calibration and hardware engineering but also in leadership, problem solving and professionalism as well as being a great friends. I could not have made it to the end without your support, both for mental health and professional support.

I would also like to give a special mention to the Sheffield University Staff Cricket Club. You made me feel very welcome from day one and, despite only having spent one season with the club, I feel as if I've been part of the club for years. I will carry the honour of "*Net bowler of the century*" with pride.

I would also like to thank my supervisor, Ed Daw, and I am extremely grateful for the opportunity that this PhD has brought. Your wealth of expertise has been a great source of inspiration and has been an interesting journey navigating LIGO instrument science under your tutelage.

Finally, I would like to thank my Mum, Dad and Brother who have always supported me thought my life journey and this PhD was no exception. You have always been there to offer support and guidance and you have taught me so much and I have a lot more to learn from you. Thank you for always being there for me.

Contents

List of Figures

List of Tables

Chapter 1

Theory and Sources of Gravitational Waves

> If time travel is possible, where are the tourists from the future?
>
> Steven Hawking

The Newtonian theory of gravity [14] is a remarkably simple description of gravity that can aptly explain much of the observable universe. However there remained a fundamental flaw with this theory, which became known as *action at a distance*, whereby an observer could instantaneously measure the effect of changing gravitation fields at any point in space (even light-years away) [15]. This highlights one of the peculiar nature of Newtons theory of gravity which, unlike theories for other physical systems, does not contain waves [15].

Laplace is often credited as one of the first to attempt to describe the action of gravity with a delay. His description required a fluid that can limit the propagation of gravity to a finite speed and would induce orbital decays through friction [15]. The theory was abandoned when Laplace concluded that for such a fluid to exist, the speed of gravity would be much greater than the speed of light and that orbital decays of planets did not fit his model [15].

In this chapter, we will recap the Newtonian Laws of Gravity before exploring the Einstein description of gravity. Here we will introduce the famous *Einstein Field Equations* from the General Relativity and show how the propagation of gravitational waves arises. Furthermore, since the generation of gravitational waves requires immense energy, we will explore some of the cosmological engines that produce gravitational radiation.

1.1 Gravity

1.1.1 Newtonian

In the Newtonian theory, gravity is created by mass [15, 16]. Published in 1687, Newton stated that **"Every particle of matter in the universe attracts every other particle with a force that is directly proportional to the product of the masses of the particles and inversely proportional to the square of the distance between them"** [14, 17]. This is more recognisable as the equation:

$$F = -\frac{Gm_a m_b}{r^2} \tag{1.1}$$

Where F is the force, m_a is the mass of the primary body, m_b is the mass of the secondary body and r is the distance between the bodies. G is the gravitational constant, 6.67430×10^{-11} $\mathrm{m^3 kg^{-1} s^{-2}}$ whose value has been determined experimentally. Newton's law of gravity successfully explained Kepler's observations of the dynamics of the planets of the solar system and, are sufficient for most observed gravitational dynamics in astrophysics.

However, there remained problems with Newtonian gravity. One of which was the orbit of Mercury did not fit with the model. This became known as the perihelion of Mercury problem and was solved when Einstein introduced his general theory of relativity. Another problem with Newtonian theory of gravity is that there was no metric to connect space and time. Newton's law of gravity applies the instantaneous propagation of information about gravitational forces, which is a contradiction with Einstein Special Theory of Relativity. Einstein was aware of the contradiction when publishing Special Relativity and the General Theory of Relativity was his solution to the contradiction.

1.1.2 General Relativity

The General Theory of Relativity is a an elegant description of the dynamic universe. Here we will look at the key equations derived by Einstein following the conventions in Schutz [16], Misner et al. [18], Poisson and Will [19], Daw [20]. Einstein broke with convention and proposed that the universe was not flat and static but was dynamic and curved. In order to understand how gravitational waves propagate though space-time, we will briefly look at how space-time can be express as manifolds. A *manifold* is a term used to express a continuous space that appears locally flat [15, 16]. With the help of many maths professors, Einstein learned the subject of *Riemann* differential geometry such that, space and time can be related to matter and energy expressed in orders of a symmetric rank 2 tensor $\boldsymbol{g}$. The rank of a tensor is simply the number of indices there are for example, $g_{\mu\nu}$ has two subscripts therefore is of rank 2. Here the tensor field $\boldsymbol{g}$ is also known as the metric tensor (or metric for short) and this will contain the information on the structure of the manifold which can be solved to work out the trajectories of particles in the presence of gravitational fields [18]. It is possible to solve the Einstein equations for waves for which, the form of the waves if governed by the observer we choose. The choice of observer, known in the theory as a *gauge* of the metric, is the co-ordinate system we impose to describe the metric. The choice of manifold, metric and gauge is important as it can greatly simplify the mathematics as we shall see later.

From the special theory of relativity, we learn that different observers will measure different distances and times depending on their relative velocity. These are the laws of length contraction and time dilation respectively. Therefore, in the construction of a general theory of relativity, we must be able to express any observable physics in a manner that is independent of the observer coordinate system. This is known as gauge freedom and for the class of solutions we are interested in, solving for waves, we express the solutions in the *Lorentz* frame. This frame is one that is at rest such that there are no external forces acting on the observer or test particle. Einstein Field Equations are expressed in terms of tensors because the effect of changing observer on the components of the tensors are well understood.

The Einstein Field Equations has profound implications on the structure of the universe. John Wheeler famously said *"The Einstein Field Equations tell space-time how to curve and tells matter how to move"*. The field equations are a set of sixteen second order partial differential equations, contained in the metric tensor $g_{\mu\nu}$ however, this can already be simplified to ten equations since the metric is symmetric (the indices can be interchanged freely). The curvature of space-time is

given by the Einstein curvature metric $\mathcal{G}_{\mu\nu}$. The *stress-energy tensor*, $\mathcal{T}_{\mu\nu}$ contains the information about the source and how matter behaves with the curvature of space-time. Thus, the Einstein Field Equations can be elegantly written on one line as:

$$\mathcal{R}_{\mu\nu} - \frac{1}{2}g_{\mu\nu}R + \Lambda g_{\mu\nu} = \frac{8\pi G}{c^4}\mathcal{T}_{\mu\nu} \tag{1.2}$$

where $\mathcal{R}_{\mu\nu}$ is the Ricci tensor, R is the Ricci scalar, c is the speed of light and G is the universal gravitational constant. The Ricci tensor and the Ricci scalar both describe the curvature of space-time therefore, we can combine these into a single tensor in the form of the Einstein Curvature tensor $\mathcal{G}_{\mu\nu} = \mathcal{R}_{\mu\nu} - \frac{1}{2}g_{\mu\nu}R$. Therefore, we re-write Equation 1.2 as:

$$\mathcal{G}_{\mu\nu} + \Lambda g_{\mu\nu} = \frac{8\pi G}{c^4}\mathcal{T}_{\mu\nu} \tag{1.3}$$

The cosmological constant Λ was often regarded by Einstein as a mistake and was included to balance the stress-energy tensor $T_{\mu\nu}$ in order to create a static universe. It was later removed by Einstein after his first publication of Equation 1.2 however, when Hubble discovered the universe was expanding [21–23], Einstein later re-instated Λ. Whilst Λ was considered by Einstein as his *"biggest blunder"*, over extreme cosmological distances, Λ has been modelled as non-zero although, locally it can be ignored. Therefore, we can further simplify the Einstein Field Equations with $\Lambda = 0$ to obtain:

$$\mathcal{G}_{\mu\nu} = \frac{8\pi G}{c^4}\mathcal{T}_{\mu\nu} \tag{1.4}$$

General relativity is written in the mathematical language of *tensors*, where we define a tensor as a fixed relationship between two vectors. This is important to understand since, one of the properties of tensors is that, if the value of a tensor is true for a given frame of reference, it is true for all frames of references.

1.1.3 Linearised Theory of Gravity

We seek to solve the Einstein Field Equations with a solution that propagates waves. Therefore, we will employ constraints over the field equations in order to simplify them. First, we will construct a mathematical description of a space-time. In flat space-time, from the Special Theory of Relativity, we can express the space-time interval between two points, ds, as:

$$ds^2 = -c^2dt^2 + dx^2 + dy^2 + dz^2 \tag{1.5}$$

where c is the speed of light in a vacuum, t is time and x, y, z are Cartesian spacial co-ordinates. An important subtlety to note is that Greek subscripts and superscripts, such as $\mu\nu$, imply that we are dealing with the four dimensions of space-time. If the subscripts were Latin, such as ijk, then we are ignoring time and only dealing with the space dimensions. Often, GR is written in the Einstein Summation notation. This is a compact way to express high dimensional vectors in a compact single line notation. Also, as implied by the name, the summation Σ is implied but rarely written. Therefore, for Equation 1.5, this can be expressed using the Einstein summation notation as:

$$ds^2 = \eta_{\mu\nu}dx^\mu dx^\nu \tag{1.6}$$

The subscripts and superscripts on the Greek indices range from 0 to 3 to indicate t, x, y, z respectively. In this instance, we use the *Minkowski metric* $\eta_{\mu\nu}$ to define space-time as a Euclidean matrix:

$$\eta_{\mu\nu} = \begin{pmatrix} -1 & 0 & 0 & 0 \\ 0 & 1 & 0 & 0 \\ 0 & 0 & 1 & 0 \\ 0 & 0 & 0 & 1 \end{pmatrix} \tag{1.7}$$

The previous equations are true in the absence of gravity however space-time, in the presence of a weak gravitational field, the metric is almost flat. In this regime, we can express the field equations on orders of $h_{\mu\nu}$ (metric perturbations) and keep only the linear terms. These are known as nearly *Lorentz co-ordinates* since $h_{\mu\nu}$ represents a *metric perturbation* away from the Minkowski metric. This greatly simplifies the ability to solve Einsteins equations without the loss of accuracy. This approach is known as *the linearised theory of gravity.* We can express this as:

$$g_{\mu\nu} = \eta_{\mu\nu} + h_{\mu\nu} \tag{1.8}$$

1.2 Gravitational Waves

Laplace was close to obtaining the correct theory of gravity. Using the same approach, with the added intuition of special relativity and electromagnetic theory, we can make some initial assumptions. The faster the wavespeed though a material, the stiffer the material must be [15]. Therefore, since light travels at the fastest known velocity, space must be the stiffest "material". Moreover, the stiffer the material, the greater the force is required to perturb said material [15]. Ergo, if space is the stiffest material, then an incredibly large force (event) would be required to impart changes in space. We will discover in further sections that these events are no less spectacular than the cataclysmic death of a star when undergoing a supernova explosion or, the inspiraling and eventual merging of compact object such as neutron stars and black holes ejecting energy in the order of solar masses [15].

In the previous section, we have seen that Einstein field equations are comprised of 16 individual equations however, due to the symmetry imposed, many of these equations cancel out and we can immediately reduce the number of independent equations to ten. We can condense these further by restricting the gauge in which we observe the gravitational field. Here, we will use the *transverse-traceless* (TT) gauge to further simplify the Einstein Field Equations down to four unique equations. For an in-depth derivation of TT gauge, see Misner et al. [18], Daw [20] otherwise, only a summary on the impact to the Einstein Field Equations will be given here. With the Einstein Field Equations, we have gauge freedom, thus we can choose any place to observe, and still construct metrics to describe the physics.

1.2.0.1 The Transverse-Traceless (TT) Gauge

The *Traceless* gauge restricts our solution to be a null vector such that the sum of the diagonal components are zero. Conceptually, this means that if we were a point on a surface with a gravitational wave passing though, we would not experience a force that pushes us in the direction of propagation. Rather, we would be tidally accelerated, fixed in place like a ping pong ball on a pond, and would instead experience an acceleration proportional to the amplitude of the gravitational wave. This removes our need to worry about *parallel transport* on curved geodesics while in the weak field limit. Mathematically, we can represent the *traceless* gauge as:

$$h_{xx} + h_{yy} = 0 \tag{1.9}$$

Transverse means that the wave travels perpendicular to the direction of propagation in only the spatial degrees of freedom. Mathematically, we write this as:

$$h_{\alpha\beta}k^{\beta} = 0 \tag{1.10}$$

Where, k is the wave vector of a gravitational wave. One important feature of asserting the TT gauge is that only pure waves (plane waves) can be restricted to this gauge [18]. This greatly simplifies the solution we need to understand the propagation of gravitational waves. Therefore, we can now state the gravitational wave perturbation as:

$$h_{jk}^{TT} = \begin{pmatrix} 0 & 0 & 0 & 0 \\ 0 & h_{+} & h_{\times} & 0 \\ 0 & h_{\times} & -h_{+} & 0 \\ 0 & 0 & 0 & 0 \end{pmatrix} \tag{1.11}$$

This gauge has a physical meaning in terms of gravitational wave detection. The transverse-traceless observer is comoving with the test masses used in GW interferometery and will sway in the presence of a passing gravitational wave.

1.2.0.2 Propagation of Gravitational Waves

We are seeking wave solutions that propagate through empty space-time, hence $T_{\mu\nu} = 0$. Next note that the spatial extent of the waves is negligible on cosmological distance scales, hence the cosmological constant term can be neglected, so set $\Lambda = 0$. Finally, note that we seek waves that propagate on a flat spacetime background, so that locally the scalar curvature is zero, and hence $R = 0$. You only get $R \neq 0$ if you are sitting on top of matter and energy. Hence we get to:

$$R_{\mu\nu} = 0 \tag{1.12}$$

This equation is then written in terms of Christoffel symbols, and linearised in the sense that all terms that are higher than linear order in the coefficients of the h matrix and its derivatives are thrown out such that $\Box h_{\mu\nu} + f(h_{\mu\nu}) = 0$. Wave solutions of the Einstein equations corresponding to transverse waves propagating in the z-direction correspond to the subset of this equation given by $\Box h_{\mu\nu} = 0$, where $h_{\mu\nu} = 0$ for μ and ν not equal to x or y, and simultaneously $f(h_{\mu\nu}) = 0$, for the same subset of solutions. Because only the x and y directed components of $\mathbf{h}$ are non-zero, the waves are transverse to the z-direction, which is the direction of propagation. Furthermore, the condition $f(h_{\mu\nu}) = 0$ turns out to also require that $h_{xx} + h_{yy} = 0$. The two constraints on these wave solutions lead to the coordinate system where these conditions are satisfied being called the transverse traceless gauge. Note also that the symmetry of $g_{\mu\nu}$ with respect to the interchange $\mu \leftrightarrow \nu$ leads to the further condition that $h_{xy} = h_{yx}$.

As a result on the conditions we have imposed on the Einstein Field Equations, we can write the Einstein Field Equations as a wave equation. The propagation of gravitational waves in vacuum, in a flat background, far from the source field, is given by:

$$\mathcal{G}_{\mu\nu} = \mathcal{R}_{\mu\nu} - \frac{1}{2}g_{\mu\nu}R = 0 \tag{1.13}$$

Therefore, we can say that $\mathcal{G}_{\mu\nu} = 0$. These are known as the Biancci identities and the details of which are beyond the discussion of this thesis. Furthermore, by asserting that we are in the Lorentz gauge, we can express Equation 1.13 more simply as a wave equation:

$$\left(-\frac{\partial^2}{\partial t^2} + \nabla^2\right) \bar{h}_{\alpha\beta} = 0 \tag{1.14}$$

This can be written more compactly using the d'Albaterian wave operator $\Box$:

$$\Box \bar{h}_{\alpha\beta} = 0 \tag{1.15}$$

The solution to the wave equation is called a *plane wave* and takes the form $A^{\mu\nu} \exp(ik_\mu x^\mu)$. Thus, along with our gauge restrictions, we can write a solution to the Einstein Field Equation (using the formalism in [20]) to wave propagating in a weak field as:

$$g_{\mu\nu} = \begin{pmatrix} -1 & 0 & 0 & 0 \\ 0 & 1 & 0 & 0 \\ 0 & 0 & 1 & 0 \\ 0 & 0 & 0 & 1 \end{pmatrix} + \begin{pmatrix} 0 & 0 & 0 & 0 \\ 0 & h_+ & h_\times & 0 \\ 0 & h_\times & -h_+ & 0 \\ 0 & 0 & 0 & 0 \end{pmatrix} \cos(k_z z - \omega t + \phi_0). \tag{1.16}$$

where h_+ and $h_\times$ are two independent polarisations of the propagating wave and show the orthogonal polarisation of the gravitational wave. For a wave propagating along the z-axis, there will be a stretching along the x-axis simultaneously, there will be a squashing in the y-axis. We can better show this polarisation with a ring of test particles. It is interesting to note that between the + and $\times$ polarisation, there is a 45° rotation meaning that a GW radiation is invariant in 180°. This polarisation lends itself to a detection scheme whereby one can measure the differential length of two orthogonal directions. A Michaelson interferometer is an ideal choice for the task and has already produced scientific revolutionary results.

1.2.1 Sources of Gravitational Waves

All gravitational wave sources discovered thus far by LIGO are from compact binary coalescences, as they are the most efficient emitter of gravitational waves, hence our search volume for these classes of source is far larger than for the others [24, 25]. There are many sources that can produce gravitational waves and these sources span a large frequency range (1.1). We will briefly explore the generation and how their expected GW emission signature.

Band type	Corresponding Frequency	Source of Emission	Suitable Detector
Extremely low frequency	10^{-18}Hz $\sim 10^{-15}$Hz	Cosmic background	GW like signatures in the Cosmic Microwave Background Radiation.
Very low frequency	1 nHz $\sim$ 1 mHz	Supermassive Black Hole Binaries and Cosmic Strings (CW sources)	Pulsar Timing Arrays.
Low frequency	1 mHz $\sim$ 1 Hz	Supermassive black hole coalescence's, Extreme mass ratio coalescence	Space-based interferometers
High frequency	>1 Hz	Binary black holes, binary neutron stars, neutron star black hole binaries.	Terrestrial interferometers and Weber bars.

Table 1.1: Table of the typical frequency emission range of gravitational waves and the suitable detector to cover that range. There is not one detector that can cover the entire range, much like EM observatories, so a network of GW observatories would be required working in tandem to cover the broad spectrum. Credit: Creighton [12]

1.2.1.1 Compact Binary Coalescence's (CBCs)

Compact Binary Coalescence's (CBCs) are a class of gravitational wave sources that are the result of merging objects such as black holes and neutron stars. Systems can can consist of binary black holes (BBHs), binary neutron stars (BNSs) or black hole and neutron stars (NSBHs). Energy lost in the inspiral of the orbit is emitted as gravitational waves. The closer the object get to one another, the faster the angular velocity of the objects and the higher the frequency of the GWs up until the point where the objects merge. This signal is known as a chirp as the frequency whistles though the sensitivity band of GW detectors, Figure 1.1.

Pattern matching, using template banks, is used in the analysis of LIGO dimensionless strain. A template bank is a collection of realisations of general relativity numerically solved for various parameters of compact objects. Such parameters include sky location, spin, mass, precession, distance, interferometer (IFO) antennae pattern and IFO sensitivity. It is common to express the the gravitational wave amplitude, (h_0), of two orbiting compact objects in term of the *chirp mass* M:

$$\mathcal{M} = \eta^{3/5} m = \left(\frac{m_1^3 m_2^3}{m} \right)^{1/5} \tag{1.17}$$

As well as the orbital period P:

$$P = \left(\frac{4\pi^2 a^3}{Gm} \right)^{1/2} \tag{1.18}$$

where $a = \dfrac{p}{1-e^2}$ is the semi-major axis of the orbit. Thus, we have:

$$h_0 = \frac{2}{c^4 R} (G\mathcal{M})^{5/3} \left(\frac{2\pi}{P} \right)^{2/3} \left(\frac{1}{1-e^2} \right) \tag{1.19}$$

The first successful detection was achieved on September 14, 2015 at 09:51 UTC [26]. Figure 1.1 shows how the signal appeared in the detector using two different visual methods. This event has the name GW150914 and lead to the award of the Nobel Prize for Kip S. Thorne, Rainer Weiss and Barry C. Barish *"for decisive contributions to the LIGO detector and the observation of gravitational waves"*[27].

Furthermore, another landmark event was the detection of a pair of Neutron stars coalescing along with their electromagnetic kilonova counterpart [28]. This has become known as multi-messenger astronomy since the combination of gravitational waves and electromagnetic observations are used in tandem to analyse the event. The progenitor of the system was first identified in [29].

1.2.1.2 Continuous Waves

Continuous wave (CW) GW sources are mainly attributed to Pulsars, rapidly rotating neutron stars, that are not perfectly symmetric about their rotation axis [30]. Signals are very weak and can easily be masked by instrument noise. Furthermore, long, unbroken stretches of science data from the detectors is required in order to reduce the uncertainties in the search algorithms since many hours to days of integrated data is used to search for signals. These signals will appear as almost static frequencies (lines) in the long duration power spectra. We can estimate the signal using the spin axis formula:

$$h \sim \frac{2\epsilon\Omega^2 I_{NS}}{r} \tag{1.20}$$

where I_{NS} is the moment of inertia of the neutron star, ϵ is the fractional asymmetry of the neutron star, $\Omega = 2\pi f$ is the gravitational wave angular frequency and r is the distance to the neutron star. If we use typical values for the given parameters, see Schutz [16], we get $h \sim 10^{-25}$. The typical value used in this calculation are informed from electromagnetic observations of pulsars which were first discovered by Bell [31].

1.2.1.3 Burst

Short duration (< 10 seconds) transient signals that do not lend themselves to template bank style analysis are categorised as *Burst* sources. A large range of source can be responsible for a short duration burst event. One example is core-collapse supernovae [18]. In this scenario, the ejection of matter from the core of the supernova form the GW signal. It is difficult to model these signals since they can be dispersed over a large time-frequency bandwidth of the LIGO sensitivity range, even up to a few kHz .

Another class of burst sources are long duration ($10 - 1000$ seconds) transient signals that do not lend themselves to template bank style analysis. The progenitor of such a signal is thought to be from the death of massive stars. There are two classes of models that are thought to give rise to such signals. These are newly formed neutron stars that are rapidly spun up from an infall of matter from an accretion disk. The other model is clouds or clumps of material within an accretion disk, rapidly orbiting a large gravitational body, will emit long duration burst signals. In either case, the signals are expected to be narrowband and searches for these signals can be found in Thrane et al. [30], Klimenko et al. [32], Sowell et al. [33], Abbott et al. [34, 35].

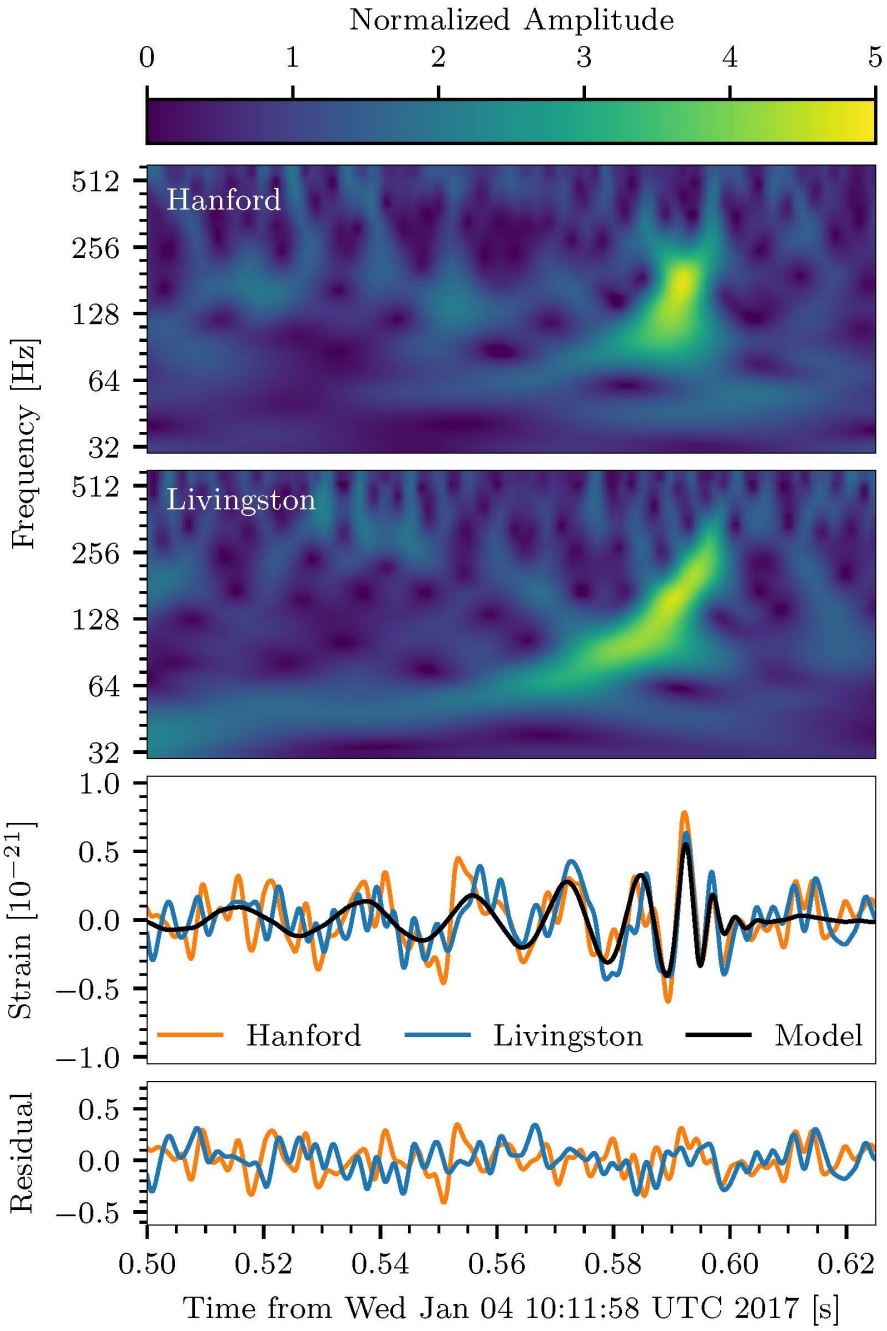

Figure 1.1: The top two traces show the power spectrogram of the Hanford (top) and Livingston (second) detectors at the time of the event. The third plot is an overlay of time series of the data from the two observatories with the model of the event overplotted. The final plot is the residual of the subtraction of the model from the data timeseries. Credit: Caltech/MIT/LIGO Lab

1.2.1.4 Stochastic

The stochastic background consists of a superposition of unresolved sources together comprising a detectable signal. Their signature in a detector network is correlated between the outputs of multiple detectors above expected backgrounds. The ultimate target of stochastic searches is the gravitational wave stochastic background from the big bang [36]. Detection of this background would be an historic discovery, providing initial-value data on the pre-inflationary Universe not available from other sources. Foregrounds from contemporary astrophysical sources of stochastic background may obscure any such signal over the whole LIGO detection band, though discovery of astrophysical stochastic background would itself be a significant achievement.

Chapter 2

A New Window into The Universe

That's one small step for a man,
one giant leap for mankind.

Neil Armstrong

Galileo Galilei (1564 - 1642) is considered the progenitor for modern observational astronomy. A natural philosopher who advocated for the scientific method, which we still adopt today, and his innovative experimental techniques revolutionised physics. The invention of the telescope, a literal window into the heavens above, is the ancestral beginning of the modern GW interferometery - not only in term of the scientific process but also changing the way we understand the universe.

In Chapter 1, we saw the theoretical description of gravitational waves. We argued for the stiffness of space-time and the amplitudes of GW events are very small therefore, measuring GWs would require extremely precise instruments. As a result, whilst the theoretical description was refined, many thought it would be impossible to construct a detector capable of measuring such subtle disturbances.

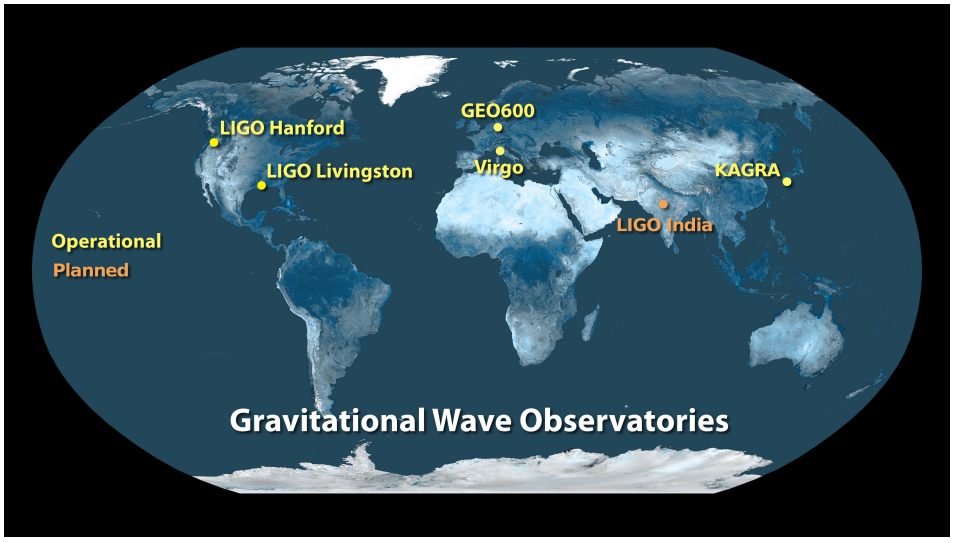

Figure 2.1: As of 2020, the current and in-construction, network of GW observatories. Credit: Caltech/MIT/LIGO Lab

Since the early 1960s, many experimental techniques have attempted the challenge of detecting gravitational waves [18, 37, 38]. The LIGO observatories, co-hosted by Caltech and MIT and funded though the National Science Foundation (NSF), located in the town of Livingston in the state of Louisiana and the town of Hanford in the state of Washington, have made breakthrough discoveries with the successful detection of gravitational waves from compact objects. Many advancements in technology have enabled the observatories to achieve the required sensitivity. The drive to improve the sensitivity and measure more exotic sources of gravitational waves has led to global network of observatories that include Advanvced LIGO (AdvLIGO) [5, 39], Advanced VIRGO (AdvVIRGO) [40, 41], GEO 600 [42, 43], TAMA [44–46], KARGA [47]. Planning is already underway for more advanced observatories such as AdvLIGO+ [48], LIGO India [49–51], bKARGA [52], LISA [53], Einstein Telescope [54], NEMO [55] and Voyager [56, 57].

In this section we will explore the history of gravitational wave detectors and measurement techniques from the resonant mass detectors, pulsar timing arrays, current and future interferometry. Furthermore, we will touch on the current challenges associated with LIGO and the sources of noise impacting the strain sensitivity.

2.0.1 Resonant Mass Detectors

Early efforts of GW detection began in the late 1960s with the use of resonant mass detectors, sometimes referred to as bar detectors. These were large cylindrical bars of high grade aluminium, 2 metres in length and 1 metre in diameter, suspended by wires in a vacuum chamber. Pioneered by Joseph Weber, they work on a simple principle of two masses connected by a spring. In the case of these detectors, a strain transducers in placed in the centre of the aluminium bar and the longitudinal mode of the bar behaves like two masses on a spring [38].

Resonant Mass detectors are still in operation such as ALLEGRO at Louisiana State University [58]. Modern resonant mass (bar detectors) are rare since interferometers have overtaken them as the more sensitive detector however, modern bar detectors are encroaching on the sensitivity of interferometers. This is because, bars have around ten levels of isolation as well as being cryogenically cooled with liquid helium to ~ 4 K. Future developments of bar detects are looking to use dilution refrigerators to cool down to ~ 50 mK [38].

2.0.2 Pulsar Timing Arrays

Pulsar Timing Arrays is an astronomical detection technique that measures the radio pulses emitted by rapidly rotating neutron stars [59]. Highly localised jets of radiation are emitted at the poles of these stars that arrive at Earth as radio pulses. The timing of arrival of these pulses are extremely consistent and make very good clock for the universe and can even be tests for the Shapiro delay [60]. Therefore, slight irregularities in the timing of these radio pulses can be a good measure of General Relativity and by extension, gravitational waves. Infrastructures such as Jodrell Bank [61], the Square Kilometer Array (SKA) [62] and the Parkes Pulsar Timing Array [63] are attempting to measure gravitational waves using pulsars.

2.1 Laser Interferometry

2.1.1 A Brief History

Proposals for an interferomter style GW detector arose as early as the 1960s by [64] however, because the technology and funds to build very long baseline interferometers with acceptable beam divergence and light stability was not available, Weber

Bars remained as the more sensitive detector [65]. It wasn't until the 1980s, where improvements in lasers and optics, began to supersede the sensitivity of resonant mass detectors. This was demonstrated by three interferometers in Glasgow [66], Garching [67] and MIT [68]. Weiss's outline for a interferometer detector lead to the construction of the 10m prototype at MIT [69] and a 40m prototype at Caltech soon after [37].

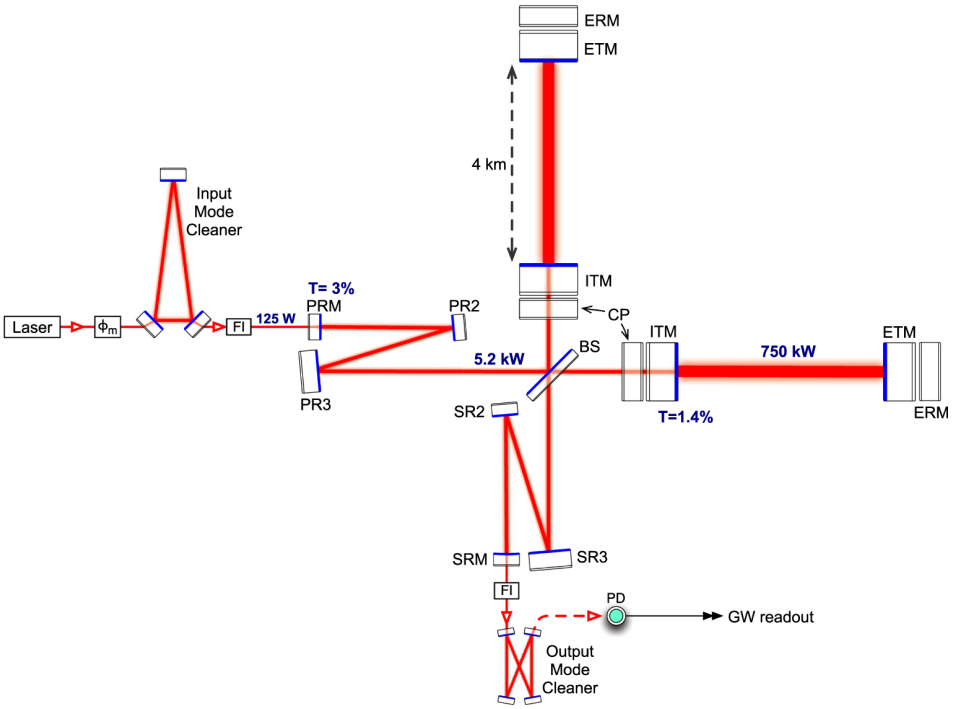

Figure 2.2: Schematic of the Advanced LIGO optical layout. Image repordiced from [5].

The modern Advanced Laser Interferometer Gravitational-Wave Observatory (aLIGO) achieved sufficient sensitivity in order to detect gravitational wave emissions from compact objects. It operates as Michelson interferometer with 4 km Fabry-Pérot arm recycling cavities, Figure 2.2. Each arm traps light within a Fabry-Pérot cavity, amplifying the sensitivity in the phase of the reflected beam to changes in the light travel time between the mirrors. The majority of the carrier light returns towards the laser, so a recycling mirror (RM) in the beam path there makes the entire interferometer resonant at the carrier frequency, increasing the light intensity at the beam splitter by a factor of about 100, and reducing the uncertainty in the phase shift between the returning beams from the two arms by about the same factor. A further signal recycling mirror (SRM) in the output path is used to modify the sensitivity as a function of frequency across the LIGO sensitive band, which is nominally between 20 and 8192 Hz - known as the sensitivity bucket. Mode cleaning cavities at both the input and output of LIGO suppress optical spatial modes above the ground, TEM_{00} mode, for improved sensitivity. The alignment of the suspended mirrors forming the arm cavities and the mean length of the arms are servo controlled to maintain resonance with the laser carrier light. The difference between the arm lengths, the so-called gravitational wave channel (also often abbreviated to DARM), is left free to fluctuate across most of the sensitive band, with some control at lower frequencies to ensure linearity in the presence of background ambient noise bleed-through into the interferometers. The peak sensitivity, the lowest point in the sensitivity bucket, is determined by

the storage time of the light within the cavity arms. This results in LIGO having the most sensitive regions at around 90 Hz (known as the cavity pole) however, the LIGO arms are slightly de-tuned to have a peak sensitivity at around 100 Hz. This has the effect of a small reduction the peak sensitivity however, opens up more of the larger bandwidth for gravitational wave detection. The light storage time (or the cavity pole) is chosen to be comparable with the gravitational wave period. A multi-stage active and passive vibration isolation system is used to insulate the interferometers from ground noise, and the entire interferometer is under vacuum to reduce noise due to scattered light. Standard advanced LIGO is quantum limited above about 100 Hz, with squeezing of light reducing the noise floor further by a few dB. The noise floor at the sweet spot frequency, commonly referred to as the bucket, is around 150 Hz at $h \simeq 10^{-23}$ in strain.

2.1.2 Key Hardware

2.1.2.1 Vacuum System

The LIGO interferometers boast the largest vacuum facility in northern America and is the one of the most critical systems in LIGO. Each IFO is evacuated to $< 10^{-8}$ Torr [70] including eleven vacuum tanks - five BSC chambers holding the core optics and six Horizontal Access Modules (HAM) chambers containing auxiliary components [71] - throughout the instruments that delivers the main and auxiliary LIGO systems. At the ends of the 4 km arms, 1 m gate valves can isolate the arms such that the Basic Symmetric Chambers (BSCs) holding the core and auxiliary components can be brought up to Standard Room Temperature and Pressure (SRTP) during maintenance and upgrade procedures. Isolating the arms is important since, during initial construction, it took approximately six months to bake and pump the arms in order to reduce the outgassing of hydrogen and water vapour within the arms to the required levels [70] and reach the required vacuum level. Since initial construction, the arms have never been vented due to the high time and cost associated with the procedure. Pumps located at the corner, mid and end buildings ensure the vacuum level is maintained. The doors have begun to reach the end of the predicted service life and have already begun to show signs of wear. A recent malfunction at LLO site as a result of the door not sealing correctly during the mid-O3 commissioning break has raised concerns over the integrity of the vacuum system and currently the vacuum system is being assessed for larger scale maintenance or potential overhaul.

2.1.2.2 LIGO Quadruple Suspension

In order to detect gravitational waves, the test masses require isolation from all terrestrial noise sources, Figure 2.3. The quadruple suspension achieves this using a 4 stage pendulum and 3 stages of cantilevered blade springs. The LIGO suspension follow the design used at the GEO600 observatory. Aston et al. [6], Matichard et al. [71] provides detailed explanations of the systems employed by Advanced LIGO. The key features of the design are summarised as:

- The Hydraulic External Pre-Isolator (HEPI) suspension provide the first, main seismic isolation and, it bolted to the concrete slab of the building. This provided the first level of isolation however is susceptible to the tilt of the building and the slab.
- The Internal Seismic Isolation (ISI) platforms within the Horizontal Access Modules (HAM) chambers provide the second stage of isolation, mainly for the auxiliary systems.

- Four stage pendulum provides, with two chains of suspended optics hang from the upper stages. Each level of pendulum suppresses frequencies by a factor of f^2.
- 40 kg test masses at the final stage are suspended by fused silica fibres, to create a monolithic final stage, to reduce thermal noise and friction loss.
- The penultimate mass and the test mass will have *ears* that will provide locations for the fused silica fibres to be bonded and welded to. This method has been shown to yield the optimal thermal noise isolation [6].
- Cantilever blade springs, made of maraging steel, will be used to assist the vertical degree of freedom.
- Components must be able to operate at high vacuum $\sim 10^{-8}$ Torr. The high vacuum reduces gas noise and prevents contamination of the highly reflective optical surfaces.
- Optical Sensor and Electro-Magnetic (OSEM) [72] actuator provide control over the upper-intermediate level masses and Advanced LIGO Optical Sensor and Electro-magnetic (AOSEM) actuators provide control over the penultimate masses. Passive damping, through the use of eddy current dampers, was found to not meet the thermal noise requirements for the level of damping achieved [73].
- Global control uses the front end CDS system to control the overall alignment of the arm cavities using the measurements from the full IFO and acting on the ETMs and ITMs [6, 74, 75].

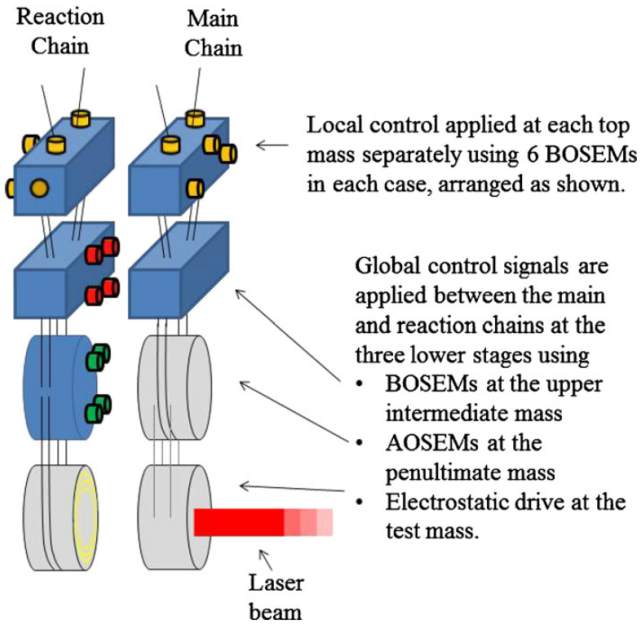

Figure 2.3: Cartoon of the LIGO quadruple suspension pendulum with both the main and reaction chain. As shown, there are two chains of suspended optics. The *main chain* is the main suspended optics that interacts with the main laser. The *reaction chain* holds equivalent components the main chain however, the reaction chain is used as the mounting points for the passive and active actuators. Image credit: Aston et al. [6].

2.1.2.2.1 The Blade Springs The blade springs are made of maraging steel due to the high tensile strength and low dislocation noise under load. Fabrication of each spring is made by grinding stock material to the desired thickness before rolling to the required curvature then hardening though martensitic ageing [76]. The springs demand tight tolerances since the deflection of the spring under load is expected to up to 300 mm and, small errors in the final stiffness can result in large deviations in the deflection morphology thereby, reducing stability and increasing the locking difficulty. The load applied to the springs, hung by steel wires, is attached with clamps at the end of the springs to maintain uniform bending across the spring.

It is also pertinent to address the thermal response of the blade springs. There will be a slight deflection of the spring as they warm and cool with the surrounding environment [77]. There is not active control over the blade springs therefore, the building temperatures are highly regulated in an attempt to keep a constant temperature to ensure that the blade springs are relatively unaffected by the outside weather conditions.

2.1.2.2.2 Beam Rotation Sensors The Beam Rotation Sensors (BRS) are precise environmental tilt sensors mounted adjacent to the interferomter suspensions on the same concrete slab with the most modern instrument featuring precision machined balances using thin flexures [78]. This is to measure the tilt of the ground motion local to the test mass. These measurements are fed back into the suspension control loops further increasing the robustness of the suspensions to local ground motion. Such motion can arise from seismic waves propagating though the earth from earthquakes, daily activity of human traffic and building tilt due to high winds [79, 80]. The latter is mainly a problem for the Hanford observatory due to the observatory being located in an exposed flat landscape however, Livingston suffers from additional ground motion from trains from a nearby rail line. A detailed description of the BRS system can be found in Ross [81].

2.1.2.3 Monolithic Fibres

In initial LIGO (iLIGO) and during the first observing run (O1) of AdvLIGO the final stage test mass was suspended with steel piano wire. Since O2, the AdvLIGO and AdvVirgo test masses are suspended by fused silica fibres drawn from rods using a precise CO_2 laser drawing robot [82]. This upgrade has two main advantages over the piano wire (steel) suspension. This first is reduced friction from the silica fibres which reduces the pendulum suspension noise and opening up more of the lower frequency band for GW detection [83]. The seconds effect is pushing the violin modes to higher frequency [82]. The result of this upgrade also reduced the thermal noise in the LIGO sensitivity sweet spot (150 Hz) by an order of magnitude. The fibres are attached via bonded standoffs, known as *ears* (Figure 2.4), that are welded using room temperature silicate bonding onto the flats of the test mass and the penultimate mass of the main chain since both the penultimate and test masses are fused silica and, alternative attachment methods (adhesive and rubbing friction joint) would be too noisy. The glass fibres also allow for suspending heavier test masses. The initial glass fibres were quasi-cylindrical. The newer fibres used in O3 were more elliptical in morphology. This change increases the lateral stiffness whilst sacrificing horizontal stiffness.

There are three main loss mechanisms in the silica fibres [84]: surfaces losses from imperfections and contaminants on the fibre surface [83]; bulk losses from internal stresses within the silica fibre [85] and, thermoelastic loss from thermal expansion of the fibre caused by heat transfer [86]. In order to mitigate thermal noise contributions of the silica fibres, they are dumbbell shaped which almost nullifies most thermoelastic effects to 10^{-19} Hz at 10 Hz [6, 82, 83]. Polishing the

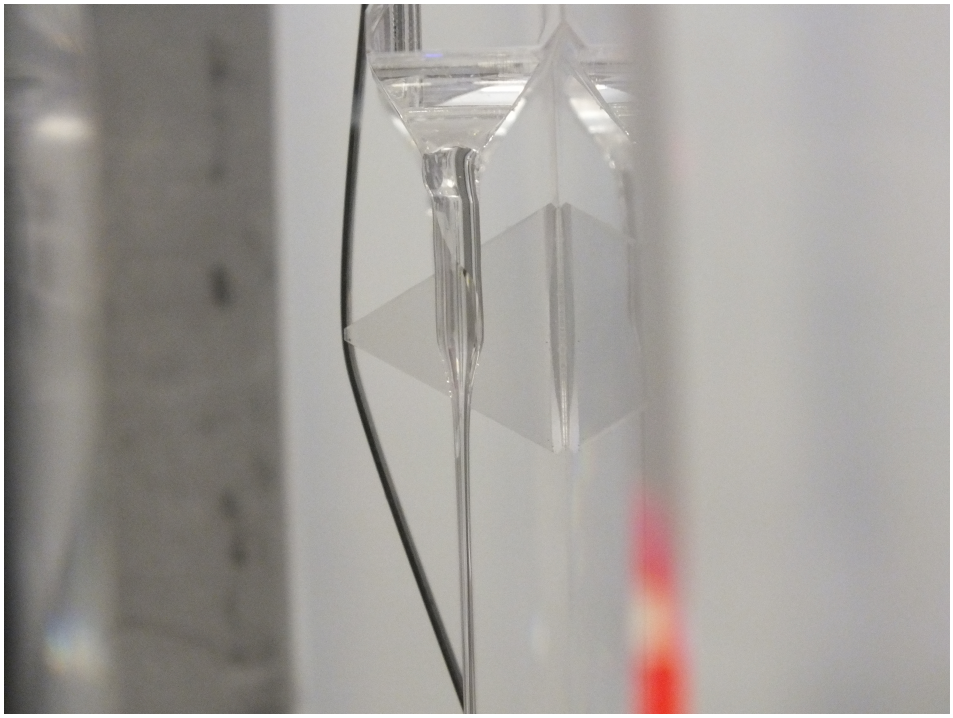

Figure 2.4: Side view of the bonded ears and the glass fibre at the LIGO Livingston Penultimate Mass (PUM) during the O3 upgrade. The triangular block is bonded to the test mass which allows the steel suspension wire from the upper stages to be looped around the PUM. In-front of this is the *ear* from which the glass fibre is suspended that connects the main test mass. Image credit: LIGO Livingston.

stock material before pulling the fibre has been shown to increase the strength of the fibre. This techniques anneals the surface material using a gas torch to melt the surface material. Since the fibres are pulled to a such a thin diameter, 400 μm, polishing after pulling the fibres would reduce their strength [83]. Bulk loss is mitigated by pre-tensioning the fibres before final installation which prevents creaking, a term used to describe the slight extension of the fibre when under load.

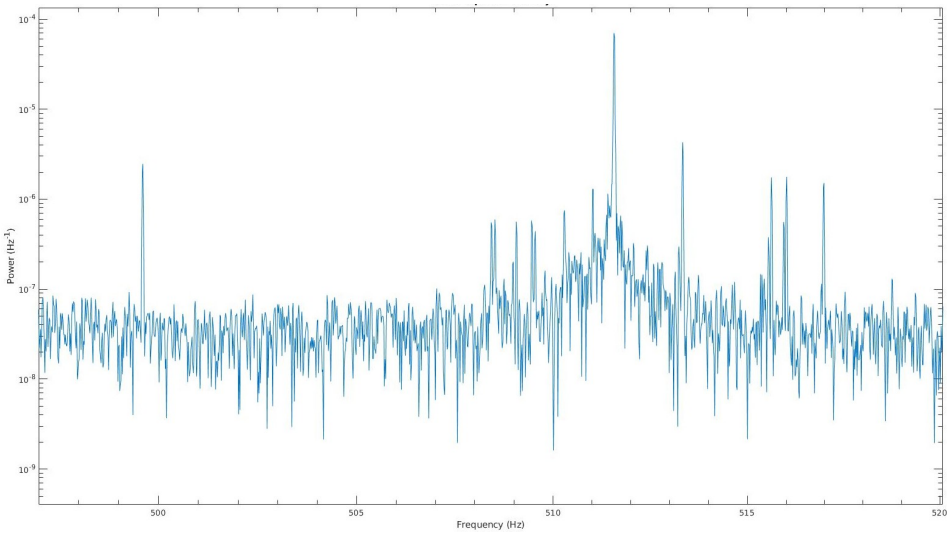

Figure 2.5: First order violin modes of the at LHO. There will be a doublet peak for each suspension silica fibre and the amplitude of these peaks will vary as energy is shared between the two lateral degrees of freedom. There will be 8 peaks per optic therefore across all the optics there will 32 fundamental violin modes and are concentrated in a 10 Hz range. Damping of the violin modes is a tricky task since extremely narrow filters are required to isolate the target peak in such a crowded region frequency space.

The violin modes are the resulting mechanical excitation seen in the LIGO spectrum from the monolithic fibres. They have extremely high Q-factors, with a separate resonance for each fibre, spaced $\sim$ 2 Hz apart. Harmonics of the violin modes have been characterised to the 8^{th} order however, measuring higher harmonics becomes more complex [6, 87]. Each resonance contains two peaks, often referred to as a doublet, as a result of the asymmetrical morphology of the glass fibres which arise from the orthogonal degrees of freedom. The spacing of the doublet peak is typically around 0.1 Hz therefore, mHz resolution of the LIGO spectrum is required to identify the modes. Feedback control systems, using narrow passband digital filters, are used to actively damp the fundamental, first second and third overtones (harmonics) of the test mass suspensions. Left un-damped, these resonances can be excited during noisy periods and inhibit operation of the interferomter.

2.1.2.4 Optics

The LIGO suspensions contain two chains of fused silica glass masses with each chain totalling $\sim$ 120 kg. Each interferometer has four test masses suspended in a quadruple isolation chain. The main test masses weigh 40 kg, are 34 cm in diameter and 20 cm thick. They are highly polished ($\leq$ 0.3 nm rms surface figure and $\leq$ 0.16 nm rms microroughness [88]) with a 2 km radius of curvature. This level of precision allows for the required optical loss is required to be $\leq$ 80 ppm. In addition, the back side of each optic is wedged to suppress parametric instability.

2.1.2.5 Main Laser

The Pre-Stabilised Laser (PSL) is the subsystem responsible for delivering the main laser, a 1064 nm Nd:YAG pumped diode laser. Here, stabilisation means the beam profile is optimised, using a series of two mode cleaners, a monolithic silicon pre mode cleaner (PMC) and a suspended triangular mode cleaner (MC) in

series to suppress all high order modes above TEM_{00}. Multi-stage Pound Driver Hall (PDH) technology maintains resonance between the laser wavelength and the interferometer cavities with different servo topologies dominating in different frequency bands. Kwee et al. [89] explains the various subsystems incorporated into the PSL system.

The main laser itself is a multi-stage process, amplifying the laser power to the required level before being injected into the arms of the main interferometer, known as the seed beam. In the first stage, a 4 W 808 nm beam is injected into into a Non-Planar Ring Oscillator (NPRO) [89–92]. The second stage consists of four ND:YVO4 crystals arranged in series that further amplifies the 1064 beam to 35 W. The third stage, which was part of the O3 upgrade, amplifies the seed beam further by a High Powered Oscillator (HPO), capable of achieving an output Gaussian beam of 220 W [89].

Squeezed Light [93] is a quantum optics technique that can overcome the standard quantum limit thereby improving the sensitivity of Advanced LIGO above 150 Hz. It is based on the Heisenberg uncertainty principle which relates measurement of the intensity (amplitude) and the phase of the laser such that it is not possible to precisely measure both states of the laser simultaneously. The process of squeezing allows for more precise measurement of the laser intensity measurement with trade off of more noise in the phase measurement. This is because gravitational waves are encoded in the intensity of the interferometer laser therefore, it is desirable to target this parameter.

2.1.3 Front End

It is useful, at this time, to briefly outline the digital interfaces used to interact with the interferometer. As noted in the previous sections, interferometry relies heavily on feedback and control. Therefore, the aLIGO front end is a multi-layered network of computers and electronics that monitor and control the interferometer and associated subsystems. In order for rapid detection and EM follow up of GW candidates, data must be piped out of the detector quasi real-time with high accuracy and easy usability. Encompassed in the front end is GPS timing computers. The AdvLIGO data acquisition and controls system [94, 95] is the main system that handles the real time opto-mechanical devices, feedback control and digital signal processing as well as responsible for FRAME writing.

The software of the front end is comprised of three main libraries which fall under the LIGO *advligorts* software library [94]. These are the Real-Time Code Generator (RTG), EPICS and Guardian. Each subsystem of LIGO is subdivided into models and these are executed on a dedicated machines. The front end machines are configured for low-latency signal processing and data transfer therefore, models must not exceed a given number of compute cycles else they will cause delays in the interferometer signal chain. Furthermore, to further reduce the latency of the signal chain, data is piped through in single precision. In the next few paragraphs, we will briefly outline the front end architecture used in aLIGO. Detailed information on the LIGO software and hardware used can be found in Bork et al. [94, 96], Bork and Thorne [97], Bork [98], Rollins [99].

2.1.3.1 Hardware

Hardware implementation of real time digital servomechanisms is achieved by dedicating one or multiple cores on Intel clone CPUs to bare metal implementation of code compiled from C and MATLAB/SIMULINK source. A single core on the CPU is dedicated to UNIX kernel operations, and communication between this controlling core and the cores carrying out the digital filter calculations is via shared memory. A parser written to translate SIMULINK models into C source

code for subsequent compilation with a bare-metal cross compiler was developed in house. Users can also write their own C source code. The main complication in writing this code is the lack of the usual math libraries, and there are many special-purpose algorithms written in-house for the LIGO controls. The resulting system is an effective compromise between a back end that instrument scientists can contribute to and a front end that is real-time capable at the 64 kHz sampling rate of the DAQ system.

2.1.3.2 RTG

The Real Time Code Generator (RTG), is responsible for compiling models into C code that can be deployed onto the LIGO front end computers. Models are formed using MATLAB Simulink [100] blocks that are converted into real time C code that can be deployed into the front-end computers. The Simulink blocks are used as a *drawing tool* thereby allowing users to simply chain blocks together to create a model. The blocks range from standard maths function through to more complex functions such as VCOs, digital signal processing tools, signal injections and data output (saving to frames).

2.1.3.3 EPICS

The Experimental Physics and Industrial Control System (EPICS) [101] is a free, open source, digital monitoring system employed by LIGO to control the operating parameters of the IFO. Parameters can be altered through the MEDM GUI interface or directly though a terminal command line interface. EPICS contains interfaces to the test points, but the actual test point software is a custom implementation of EPICS developed by Sigg and Bork and, is part of the real time front end system. EPICS implementation internally is the slow controls and monitoring of all the channels not clocked by GPS like gains, offsets, pressure, temperature, intensity on some slow photodiodes, the 16 Hz versions of all the fast channels (here fast means any channel sampled > 16 Hz) [94]. Injections can either be a pre-determined waveform or a set of instructions for modifying EPICS parameters for a subsystem model.

2.1.3.4 Guardian

The GUARDIAN is a Python interface that allows automation of the Advanced LIGO interferometer though EPICs. The primary role automate the *lock-acquisition*. Sequences of control operations that would previously have been carried out by-hand through operator control has now been automated for ease-of-operations and repeatability of the locking process however, the user can still intervene to pause, cancel or request alternative states if required. The GUARDIAN has been incorporated into multiple automation processes [94, 102]. Guardian is a system of state machines that is formed of hierarchical nodes, where each node is an individual process being controlled [102]. The nodes form a graph of states and transitions between states are governed by user defined conditions. The guardian runs alongside the IFO, on dedicated machines, and can control both the low-level front end digital controls as well as undertaking the role as a higher level manager with sub-nodes executed beneath it [102].

2.1.3.5 LIGO/VIRGO FRAME Format

Finding a flexible data storage solution is a challenge that many scientific laboratories face. Big data is a growing concern for many sectors such as finance, marketing, healthcare, research and many more. For example, the CERN Data Centre is crunching over 10^6 GB data per day, equating to over 25 PB of data in

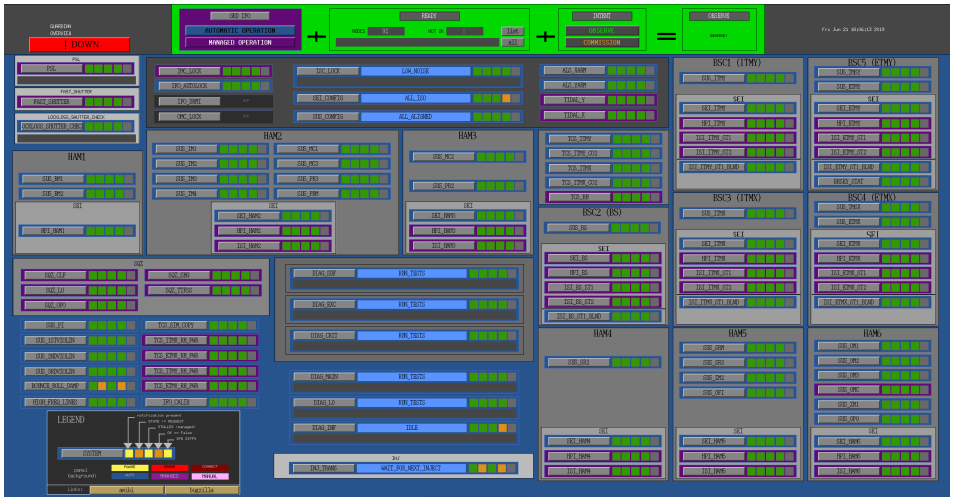

Figure 2.6: LLO GUARDIAN overview screen produced during my fellows placement. This is the main screen that commissioners and operator can monitor the interferometer automation. Each block corresponds to a separate GUARDIAN automation monitor. During the science observing state, the IFO parameters are locked in and continually monitored across the entire site and, all the block should be green to indicate the IFO is up to date with all configurations and changes. Should there be a change in a given parameter, such as drives exceeding predetermined limits or a user change, the GUARDIAN screen will highlight the offending GUARDIAN monitor and the subsystem that tripped.

1 year [103]. Whilst LIGO is not producing as much data as CERN, the character of the data is different because LIGO produces continuous time series of output from photodetectors, whereas CERN produces discreet output for each one of a set of events corresponding to collisions in the detectors. This 'always on' aspect of LIGO places special requirements on the data format chosen to store the raw data. An inter-laboratory committee decided on the gravitational wave frame (GWF or gwf) format in the 1980s [104], and GWF files are currently the format of choice for all the major experiments. These are a custom format of the HDFS [105] compression algorithm however discussion to move to a more conventional HDF5 file format is ongoing. Added complications arise when data drop-outs, mis-calibration and glitches require amendments to be made to the data requiring a new copy of the data files with the corrected data, essentially doubling the storage cost (see Table 2.1). Furthermore, whilst there is a brief embargo on GW data such that collaboration members are allowed priority over the data, eventual public release of the data dictates that the data format must be easily readable, fast to transfer and contain minimal errors. Historical data is stored on magnetic tapes that are held in secure environmentally controlled rooms at each observatory as well as at Caltech. Due to storage costs increasing, only observing runs and engineering runs are kept thereby reducing the overall amount of stored data.

Data is exported from the interferometers in two types of frames. These are science frames and raw frames. The science frame only contain data such as the the calibrated strain, glitch flags, GPS time and other parameters useful for GW detection and EM follow-up. The raw frames contain data from all the channels of data from the front end. These are mainly for detector characterisation, glitch (noise) hunting, simulations and modelling of the observatories.

There are many software packages that can read the data frames. C libraries are the preferred way to interact with the frame files such as *Libframe* and LalSuite [106]. Due to the abundance of search pipeline written in Python, PyCBC [107]

Data Set	Frame Type	Min. GPS	Max. GPS	File count	Total Size
H1 O2 h(t) C01	H1_HOFT_C01	1164554240	1188057088	5506	2.41 TB
H1 O2 h(t)	H1_HOFT_C00	1164554240	1188081664	5795	2.38 TB
H1 O2 raw	H1_R	1164554240	1188081664	367547	600.11 TB
L1 O2 h(t) C01	L1_HOFT_C01	1164554240	1188057088	5496	2.52 TB
L1 O2 h(t)	L1_HOFT_C00	1164554240	1188081664	5774	2.55 TB
L1 O2 raw	L1_R	1164554240	1188081664	367386	518.84 TB
V1 O2 h(t)	V1Online	1178200244	1235750000	28418	1.10 TB
H1 O1 h(t) C02	H1_HOFT_C02	1126621184	1137258496	2705	784.26 GB
L1 O1 h(t) C02	L1_HOFT_C02	1126621184	1137258496	3113	638.55 GB
H1 O1 h(t) C01	H1_HOFT_C01	1126621184	1137258496	2684	1.17 TB
L1 O1 h(t) C01	L1_HOFT_C01	1126621184	1137258496	3178	1.14 TB
H1 O1 h(t)	H1_HOFT_C00	1126621184	1137258496	2746	1.16 TB
L1 O1 h(t)	L1_HOFT_C00	1126621184	1137254400	2611	1.18 TB
H1 O1 rds	H1_RDS	1126621184	1137258496	41547	25.85 TB
L1 O1 rds	L1_RDS	1126621184	1137258496	41554	24.53 TB
H1 O1 raw	H1_R	1126621184	1137258496	166160	126.09 TB
L1 O1 raw	L1_R	1126621184	1137258496	166188	116.12 TB

Table 2.1: The different data sets (frames) across the LIGO observations runs. The raw frames clearly show a much larger storage size than the main science frames as a result of the raw frames storing data from all the data channels. Furthermore, as the length of the observation runs increase, the file sizes are increasing therefore, when planning future observation runs, data storage and capacity is a non-trival challenge to consider. Table reproduced from https://monitor.ligo.org/data .

and GWpy [108] are the more commonly utilised frame reading tools.

2.1.4 Noise Sources

A dedicated team of commissioners continually monitor the IFO. Through hardware injections and software, each subsystem of the IFO is modelled and forms part of the total noise budget. Features within the LIGO sensitivity band, that are not sufficiently accounted for by these models, are examined and traced in order to identify and mitigate noise couplings. Figure 2.7 shows each subsystem of noise that contributes to the total noise budget - black curve. At frequencies > 100 Hz the noise contributions are well understood however, below this threshold, the

real detector signal deviates from the model. Resolving features at low frequencies (< 100 Hz) requires long integration times which are not always feasible to conduct.

2.1.4.1 Quantum Noise

The quantum noise is the result of two main statistical fluctuations associated with the main laser beam. These are the counting statistics in the photodetectors (shot noise) and the radiation pressure of the photons on the optics [109]. This is measured as the Standard Quantum Limit (SQL) and is the maximum obtainable sensitivity permitted by Heisenberg Uncertainty Principle. For LIGO, this is designed to be at angular frequencies $\Omega > 100$Hz. The standard quantum limit, for a conventional interferometer that is utilised by LIGO, follows the formalisation given in Kimble et al. [110] and Buonanno and Chen [111]:

$$S_h = h^2_{SQL} = \frac{8\hbar}{M\Omega^2 L^2} \tag{2.1}$$

Where $\hbar$ is the plank constant, M is the optic mass, L is the arm length (cavity length) and Ω is the angular (gravitational) frequency. The LIGO interferometers design sensitivity is to meet the SQL. Therefore, high laser power is required to approach this. This can be expressed as:

$$I_{SQL} = \frac{ML^2\gamma^4}{4\omega_0} \tag{2.2}$$

Where γ is the arm cavity 1/2 bandwidth and ω_0 is the laser light frequency. Since the test masses are not fixed, the high intensity beam exerts a force on the optics via radiation pressure. As a result of the high intensity laser within the arm cavity, the coupling function $\mathcal{K}$ as a result of the radiation pressure, is expressed as:

$$\mathcal{K} = \frac{(\frac{I_0}{I_{SQL}})2\gamma^4}{\Omega^2(\gamma^2 + \Omega^2)} \tag{2.3}$$

There is a trade-off between these two noise sources. One the one hand, tuning the stored power in resonant cavities could reduce shot noise however, photon radiation pressure will increase. Heavier optics would allow increased laser power whilst minimising the increased radiation pressure noise although this bring additional challenges such as suspending heavier optics.

2.1.4.2 Seismic Noise

The LIGO suspension provide many levels of seismic isolation however, some residual motion couples into the IFO. Whilst most of the noise is within the $0.1m$ Hz $< f <$ 1 Hz region, out of the LIGO sensitivity bandwidth, if left undamped can accumulate such that locking stability (the ability to hold the arm cavities on resonance with the main IFO beam) is not possible. Furthermore, some modes of vibrations can up-convert through various mechanical and digital paths that can confuse control loops and artificially drive undesirable resonances and increase instabilities.

2.1.4.3 Thermal Noise

Like any classical oscillator, the pendulum suspensions from which he LIGO optics hang, are subject to fundamental limitation when trying to remain at rest. Unfortunately baryonic matter, of which the test masses are constituents, are subject to the laws of thermodynamics. Generally referred to in LIGO as *thermal noise*,

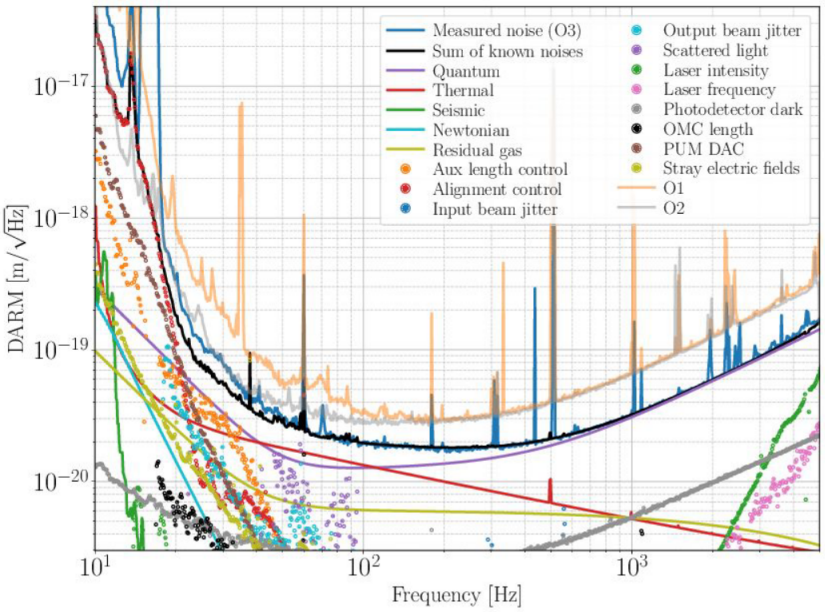

(a) LLO noise budget.

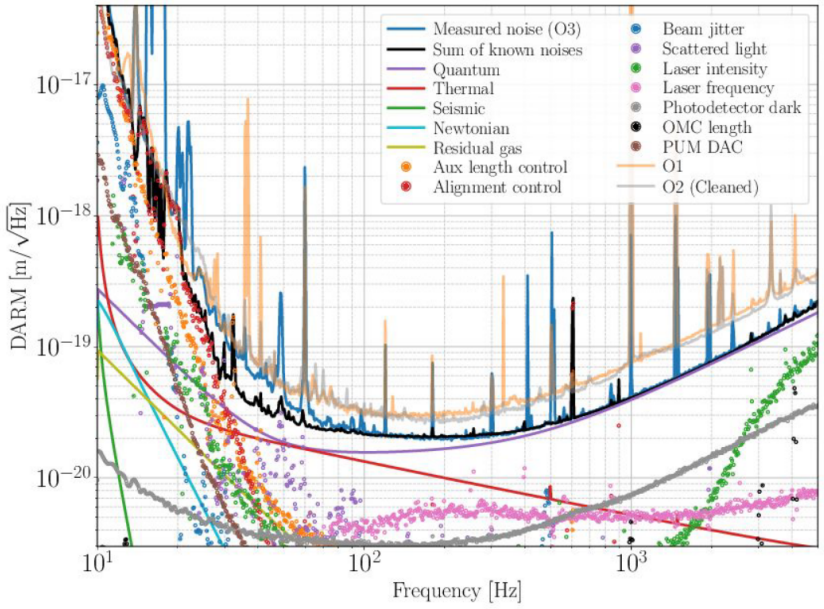

(b) LHO noise budget.

Figure 2.7: The individual contributions of each source of noise across the LIGO sensitive bandwidth. The black line shows the sum of all known noise contributions for AdvLIGO. The blue line is the real AdvLIGO spectrum with the orange and grey curves showing the best O1 and O2 sensitivity curves. There is a clear disparity in the $10-100$Hz range, more so for Hanford, and these are under investigation. Furthermore, at frequencies < 20Hz, suspension controls are the main noise barrier. At High frequencies > 100Hz, quantum noise is dominant. Moreover, thermal noise is the next limiting noise source for further LIGO sensitivity gains. Overall, the poorly understood noise is at a manageable level and known noise sources are well characterised. Images reproduced from Fig 2 from Buikema et al. [3].

the random motion of particles forming the substrate and bulk material lead to random forces on the optics, whose magnitude depends on the Boltzmann constant k_B and the temperature T. This is a simplification of *Brownian motion* in which Einstein had a hand in helping discover the true nature of phenomena [38]. In an ideal world, the displacement from thermal noise would be concentrated to an infinitely narrow frequency of the pendulum mode however, in reality pendulums are lossy. Whilst the superior optical properties of fused silica exhibit loss angles of $\phi = 10^{-9}$ at room temperature, which results in thermal noise concentrated around the pendulum natural frequency in the $\sim$ Hz region, the tails of the resonances can bleed out into the sensitive regions of the LIGO spectrum $\sim 10^2$ Hz (see Figure 2.7). As a result, thermal noise is a slow effect, taking many hours to resolve the response of the interferometer to thermal transients. Hence, mitigation of thermal noise is a key priority in the ongoing work of enhancing LIGO sensitivity, particularly important for high mass, long duration GW sources. Cooling the mirrors to cryogenic temperatures is a solution that can mitigate thermal noise, as currently being attempted by KAGRA. However this brings significant engineering and logistic challenges such as: facilities to house the cryogenic equipment; changing test mass bulk and substrate material to silicon or sapphire; increased operational costs and possible change of laser wavelength. Despite these concerns, AdvLIGO+ and Voyager are investigating proposals for using cooled optics.

In the near future, thermal effects are soon to become the limiting factor in the LIGO sensitivity region. This is because one of the easiest ways to increase sensitivity in the interferomter is to increase the laser power within the arms thereby exacerbating thermal noise. There are many mechanisms that feed into the thermal noise and these are: Brownian coating noise from mechanical losses in the highly reflective coatings; suspension thermal noise from the thin glass suspension fibres; thermal modes from the internal mechanical heating of the quadruple suspension and thermo-optic lens from radius of curvature changes of the optical surface by absorbing laser power. The large optics allows for a large spot sizes, $\sim$ 6.2 cm on the ETMs and $\sim$ 5.3 cm on the ITMs [88], on the optics, thereby reducing the coating and substrate thermal noise

Above the suspension pendulum resonance, Callen and Greene [112], Callen and Welton [113] calculated the displacement of the test mass ($x(f)$) resulting from thermal noise, known as the fluctuation-dissipation theorem, can be expressed as [6]:

$$x^2(f) = \frac{k_B T}{2\pi^3 m f} \left(\frac{f_o^2(f)}{f_o^4 \phi^2(f) + (f_o^2 - f^2)^2} \right) \tag{2.4}$$

Where T is the temperature, m is the pendulum mass, $\phi(f)$ is the mechanical loss angle of the pendulum, f_o is the resonant frequency, k_B is Boltzmann's constant and f is the frequency. A detailed explanation of individual contribution to the thermal noise contributions can be found in Franc et al. [114] and references therein.

2.1.4.4 Gravity Gradient (Newtonian) Noise

As a result of the scale of LIGO, density perturbations in Earth surface local to the test masses, induce Newtonian gravitational forces on the test masses [109, 115]. First identified in Muehlner and Weiss [69], [116] and [117] are the latest efforts to quantify the effects. The gravitational forces are produced by ambient seismic waves, which are constantly present, that will induce *seismic gravity-gradient noise* within the LIGO sensitivity band $f < 20$ Hz. Atmospheric gravity-gradient noise was also calculated in Saulson [116] however, it was much weaker than the Earth's seismic motion.

2.1.5 Observational Range

The metric of IFO observational distance is a frequently debated measurement since it can be defined with a multitude of scales. The LIGO observatories are often quoted to have an astrophysical range, measure in mega-parsecs (MPc). This metric is calculated from the luminosity distance by which a binary neutron star system, whose constituents have equal mass at $1.4M_{\odot}$, will result in a measurable signal in the sensitive band of the detector at an SNR of 8. The detector sensitivity to such a signal is averaged over the detector antenna pattern to yield the average astrophysical range. Therefore, this range metric is not strictly the maximum viewable range of the observatory but, a reasonable estimate of the sensitivity of the interferometer. For heavier mass systems, such as black holes, the observational range is much greater.

2.2 Future GW Detection

Spurred on by the success of LIGO, many more interferometer style detectors are being proposed internationally. These will form the third generation (3G) network of gravitational wave detectors. Increasing the number of observatories will allow for greater accuracy for the sky location of a GW candidate. Not only is this useful for rates and population statistics, it will greatly assist rapid follow up EM observations of the GW event. Currently, all the GW observatories are based on the northern hemisphere therefore a southern hemisphere observatory is of particular priority for the GW community since this will cover the blind regions of the northern hemisphere.

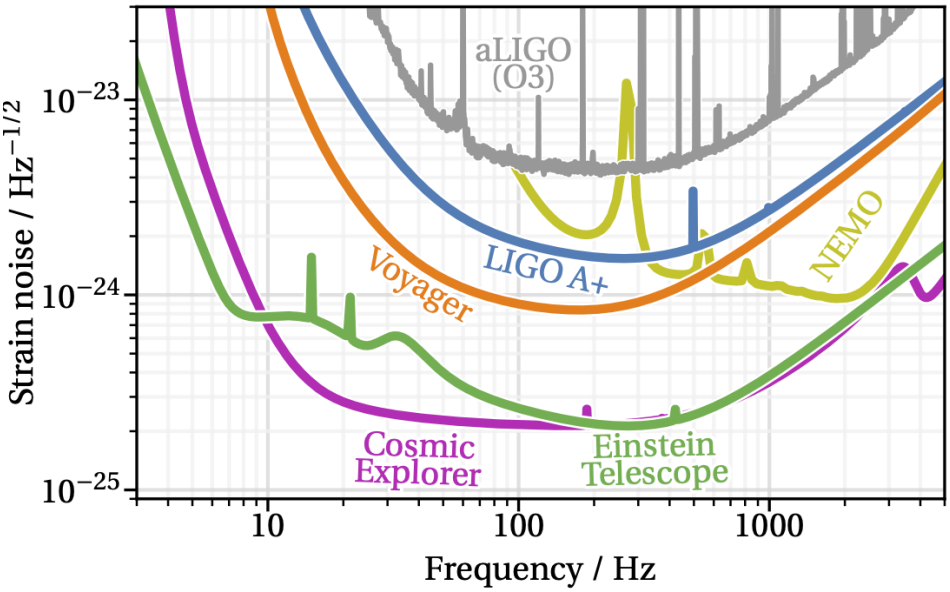

Figure 2.8: Sensitivity of future GW observatories with the current LIGO O3 sensitivity cirve as a reference. Credit: Cosmic Explorer Project.

2.2.1 Advanced LIGO A+

Advanced LIGO A^{+} will be the next phase of the current advanced LIGO observatories. There are many developing technologies that will enhance the current LIGO facilities. This includes frequency dependent squeezed light, improved mirror coatings, better manufacturing of the glass fibres, larger beam splitters, new

IFO Cases	aLIGO	A+	Voyager	CE (pess)	CE	ET LF	ET HF
Arm Length [km]	4	4	4	40	40	10	10
Mirror Mass [kg]	40	40	200	320	320	211	200
Mirror Material	Silica	Silica	Silicon	Silica	Silicon	Silicon	Silica
Mirror Temp [K]	295	295	123	295	123	10	290
Sus Fiber	0.6m SiO2	0.6m SiO2	0.6m Si	1.2m SiO2	1.2m Si	2m Si	0.6m SiO2
Fiber Type	Fiber	Fiber	Ribbon	Fiber	Ribbon	Fiber	Fiber
Input Power [W]	125	125	140	150	220	3	500
Arm Power [kW]	710	750	3000	1400	2000	18	3000
Wavelength [nm]	1064	1064	2000	1064	1550	1550	1064
NN Suppression	1	1	10	10	10	1	1
SQZ Factor [dB]	3	6	8	10	10	10	10
F. C. Length [m]	none	300	300	4000	4000	1000	500

Table 2.2: An overview of the main differences between the current AdvLIGO interferomter and the interferomters that are bring proposed. Here NN suppression refers to Newtonian Noise as discussed in Section 2.1.3.4. The F.C. Length is the Filter Cavity length and is a separate, small beam tube that runs alongside one of the IFO arms to provide a reference cavity for conditioning the main beam. Reproduced from Table 2 in Fritschel et al. [13].

test masses and upgrades to the auxiliary internal mirrors and optical components. The upgrades will span over the next two major observing runs, O4 and O5, and attempt to reach a design sensitivity of 325 MPc BNS range. This is expected to span four to five years.

High frequency and low frequency gains are hotly debated for upgrades beyond O5. Both would require significant engineering changes to the facilities, optics and software. For low frequency gain, cryogenic optics would need to be developed to achieve sufficient sensitivity < 20 Hz whereas the high frequency gain, much higher

laser power would be required.

2.2.2 KAGRA

KAGRA [118–121]is a Japanese interferomter located in the Kamioka mine in Gifu prefecture. Formerly know as the Large-scale Cryogenic Gravitational-wave Telescope (LCGT), it departs from current GW observatories as it is the first to be built underground, utilising 3-stage cryogenic suspension and optics cooled to 20 K and 3 km Fabry-Pérot arm cavities. The length of arms is limited to the size of the area in the mountain that could be excavated to accommodate the arms. Underground construction of the facility will reduce the seismic and Newtonian noise impacts on the overall strain sensitivity. The main laser will be a 400 mW Nd:YAG NPRO laser with test masses made of pure sapphire. The cryogenic operating conditions minimise thermal noise from the main laser. However, the laser power must be limited with the main constraint being the suspension fibre ability to absorb the heat from the test mass [120].

2.2.3 LIGO India

The LIGO India project [122, 123] is the latest effort to construct a new facility for the detection of Gravitational Waves with an interferometer style detector. The initiative is being lead by the Indian Initiative in Gravitational-Wave Observations (IndIGO) [124], and a site has been established in Aundha within the Hingoli District of which 99% of the land has being acquired [122, 123]. Currently geological investigations are ongoing in preparation for construction of the site [122, 123]. The detector is expected to be online in $\sim$ 2026 and will be a copy of the aLIGO+ detector configuration. Most of the construction will be shared by RRCAT and IPR however, some redundant parts will be recycled from the existing LIGO sites in LHO and LLO in order to facilitate the construction of LIGO India. IUCAA will be main institution responsible for the DAQ, CDS and data storage systems.

2.2.4 LISA and Spaced Based Observatories

The Laser Interferometer Space Antenna (LISA) [53, 125–127] an ambitious project that aims to deploy a space based GW observatory. This is a joint collaboration between the National American Space Agency (NASA) and the European Space Agency (ESA). The LISA project has been in development as early as the 1970s [126] whereby three triangular space craft 1 Mkm apart (akin to terrestrial arm length) will orbit the Sun lagging behind the Earth by 20°. Multiple factors must be taken into consideration when choosing the orbital location such as communication, cost of travel, thermal and gravitational stability.

LISA is designed to measure low frequency (0.1 mHz to 0.1 Hz) GW candidates indicative of IMBH coalescence's, supermassive BH inspirals from galaxy mergers and inspirals of lighter compact objects such as stellar mass black holes, white dwarfs and neutron stars [128]. An advantage of the space interferometers is that it is sensitive to GW in all directions however the trade off is that the spacecraft cannot be "aimed" at a particular direction. GW source direction can be obtained by accounting for the Doppler shifted signal - resulting from the spacecrafts orbit - and the measured amplitude [53]. Moreover, the chosen orbital point of the spacecrafts are required to satisfy the strict thermal and gravitational stability such that large bodies do not exert gravitational tidal forces [129].

The LISA Pathfinder project successfully demonstrated the ability to hold two gold platinum quasi-cubic test masses in drag free freefall [130]. The ESA mission was launched on December 03 2015 and collected science data from 01 March 2016 until 30 June 2017 [8]. The main constraints found during the mission

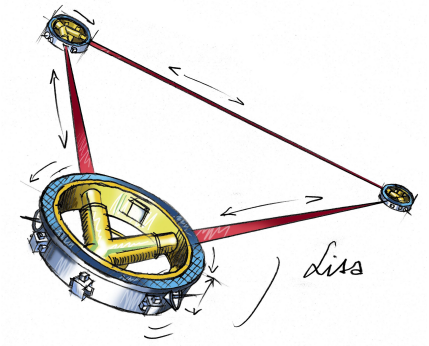

(a) A cartoon of the three satellites of LISA arranged in their orbital configuration.

(b) The launch of the LISA Pathfinder mission.

Figure 2.9: Credit: The successful launch of LISA pathfinder and the full scale LISA project is paving the way for space-based GW detectors. Data from these missions will help to cover a wider range of GW frequencies, particularity in the low frequency region. Image sourced from ESA/LISA mission [7].

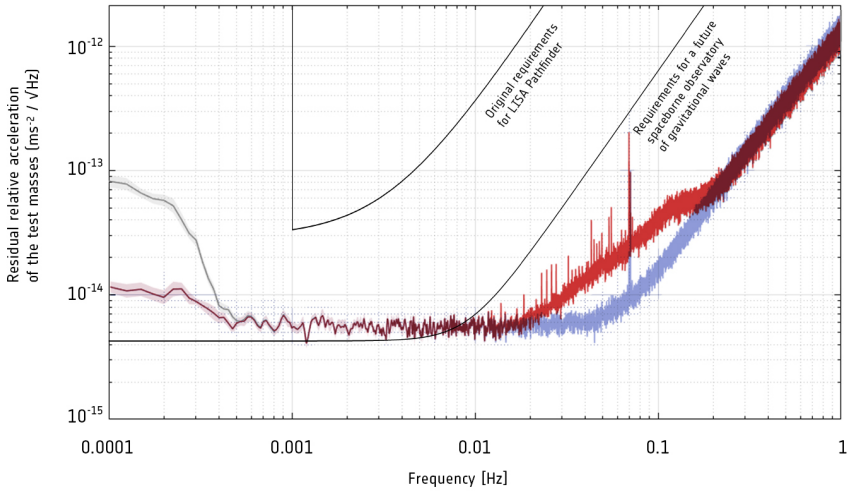

Figure 2.10: Results of the LISA Pathfinder experiment showing the acceleration noise of the spacecraft. The top black curve is the expected performance, the lower black curve is the expected LISA mission performance and the red and blue curves show the actual LISA pathfinder results. The difference between the red and blue curve is the results of further data processing of the tilt to length noise to suppress this noise noise, further improving the overall acceleration noise. Credit: Armano et al. [8].

was Brownian noise from residual gas around the test masses, calibration of the electrostatic force actuation and correcting for non-inertial effects [8]. Additional instrumentation challenges arise such as the satellite alignment introducing cross coupling noise via the control systems within the 18 Degrees of freedom in the controls system.

Other space based detectors, such as TianQin [131], Taiji [132] and DECIGO [133], are being explored by space agencies in other countries.

2.2.5 Neutron Star Extreme Matter Observatory

The Neutron Star Extreme Matter Observatory (NEMO) is a proposal for building an interferometer, technologically similar to AdvLIGO and AdvLIGO+ however, to focus on high frequency sensitivity (500 Hz − 4 kHz) [55]. The project is still very early in development and a site has not yet been chosen. The OzGrav group are keen in pushing for NEMO to be a southern hemisphere observatory and are currently conducting surveys into possible suitable locations for the observatory in Australia and Asia [134].

The astrophysical motivation is to target the core of a Neutron Star and probe the equation of state of Neutron Stars and the extreme matter that evolves around the dense objects. The evolution of neutron stars are excellent universal engines for particle physics and little is known about the core of a neutron star since is hidden from typical EM observations. GWs provide can unbiased view into the evolution and dynamics of a neutron stars core from: evolution into a neutron star at the end of the stellar life cycle; merging of smaller neutron stars and remnants from core collapses into black holes or larger binary mergers that leave neutron star remnants [55].

2.2.6 Voyager

The LIGO Voyager [57] is a proposal for another terrestrial based GW interferomter however, will feature cryogenically cooled ($\sim$ 123 K) optics constructed of silicon. The main goals of Voyager is to overcome the main limitations of the current LIGO interferometers, namely quantum noise, thermal noise and Newtonian Gravity noise [13, 57]. A detailed study of the Voyager technologies can be found in [57] however, the main points will be given below:

- Large test masses, approximately 200 kg, with improved mirror coatings and larger beam size to mitigate thermal noise.
- Cryogenic optics and suspension with silicon blade springs holding the penultimate and test masses with longer suspension chains for lower suspension resonance modes.
- Main beam wavelength changed to 1.4 μm to 2 μm operating at 150 to 200W as resulting from the change of test mass material because of the desire to cool to cryogenic temperatures.
- High power optical mirror coatings to reduce optical absorption to less than 1 ppm at 2μm at 123 K.
- Frequency dependent squeezed light, $\sim$ 10 dB, in order to lower the quantum limit.

Voyager's sensitivity will be 4-5 times greater than what is currently achievable with LIGO thereby increasing the event rate by $\sim$ 100 which equates to approximately 10 BNS daily events and around 30 BBH merger events daily [57].

2.2.7 Cosmic Explorer

The Cosmic Explorer will be a North American facility that will span $\sim$ 40 km. Using the same Febry-Pérot interferomter optical layout as LIGO. Extending the baseline of the interferometer will increase the sensitivity of the detector to $\sim 10^{-25}$ Hz$^{-1/2}$ across a larger bandwidth ($\sim$ 5 Hz to 5 kHz). The lifespan of the facility is planned for about 50 years. The three main science goals for the Cosmic Explorer project that demand such extreme detector engineering and, is similar for most long baseline GW observatories, are:

- Black Holes and Neutron Stars in the Early Universe.
- Extreme Gravity and Fundamental Physics.
- Dynamics of Dense Matter.

In conjunction with next generation telescopes, such as James Webb, Cosmic Explorer measurements of Binary Neutron Star coalescence's will attempt to probe the internal structure of compact objects. Further exploring the dynamics of matter and nucleosynthesis in extreme environments such as kilonovae high relativistic jets.

2.2.8 Einstein Telescope

The Einstein Telescope (ET) [54, 135] is a European effort for a third generation observatory. Instead of the usual *L-shaped* arms of a Fabry-Pérot interferometer, ET will operate three 10 km arms in an equilateral triangular formation and use VIRGO style suspensions. The motivation for the triangular arms is to overcome the *blind spots* in the sky position that a traditional L-shaped Michaelson interferometer suffers from. Building underground will reduce the gravity gradient noise that is expected to be a significant factor resulting from the longer baseline detector however, the facilties will need to located over 100 m underground [136]. Moreover, there will be two beams in each beam tube such that there are two interferomters in each arm. These will be a high-frequency interferometer and and low frequency interferometer such that a wider bandwidth of sensitivity can be covered. The low frequency detector will use cryogenic suspended optics $(10-20$ K) whereas the high frequency arrangement will be at room temperature. The scientific goals are detailed in [36, 137].

2.3 Conclusion

With the development of laser systems, optics, material science and engineering, it has been possible to build facilities that can isolate suspended masses in order to achieve sufficient sensitivity to measure gravitational waves. Moreover, with the success of LIGO and VIRGO, greater international funding has allowed for more ambitious facilities to begin construction and are being proposed.

Recently, there has been a great deal of friction between scientific facilities and sacred grounds upon which they are constructed. Recent examples include construction the Thirty Meter Telescope at Mauna Kea and Square Kilometer Array in South Africa. It is important to respect the social and cultural implications of building such facilities in these locations and understand the impact research has on the environment and local heritage. Failing to do so can not only greatly impact the cost of building scientific facilities but also damage the reputation, integrity and relationship science has with the general public. The construction of the next generation of gravitational wave observatories will need to factor this additional challenge into site locations. This also is the case for space based observatories admits the recent crisis of *space junk* orbiting the Earth.

Chapter 3

Needles in Digital Haystacks

> When people say 'it's always the last place you look'. Of course it is. Why would you keep looking after you've found it?
>
> Billy Connolly

It goes without saying that electronics has greatly advanced scientific discoveries however, their introduction it not without their own challenges. In Chapter 2, we have seen how LIGO digital and physical systems integrate and communicate with one another. However, the raw time series data is very messy because instrumental noise sources leak into neighbouring systems - mixing into auxiliary data channels overall, making it difficult to track down the origin of the noise. Therefore the signals are processed digitally, using a combination of time and frequency domain techniques, in order to identify characteristic resonances (lines) within the LIGO spectrum and trace their origin.

Our task here is to find an effective way of characterising waves in a data set. The standard physicist's approach is to use Fourier analysis. Therefore we begin this chapter with a summary of the practical technology and techniques of Fourier analysis. This is there to ground the reader in something with which they should be familiar, but also to permit us to expose some shortcomings of this approach, particularly if it is applied to dynamic characterisation of oscillations with time-varying frequency and amplitude. These shortcomings will be pointed out as they manifest themselves in the discussion. Following this brief introduction, the alternative technology for wave characterisation, lock-in and phase locked loop techniques, will be discussed. These too are familiar to physicists, but they too have shortcomings, which will also be discussed as they arise. Finally we will describe a novel approach to phase locked, IWAVE, invented by Edward J. Daw and developed by the Sheffield group (and partly by the author), which addresses these shortcomings and shows potential for many applications both in gravitational waves and in wider science and engineering applications.

3.1 Digital Signal Processing

3.1.1 The Fourier Transform

A simple classic oscillator can be expressed as a linear function of sines and cosines in time $f(t)$. We can analyse this system by rearranging the information in $f(t)$ thereby transforming it into a distribution function $F(\nu)$ whose coefficients resemble that of the original function. This process is known as the Fourier Transform

[138–140] and, is powerful tool for analysing periodic data. Other then the development of the Digital Fourier Transform (FT) and the Fast Fourier Transform (FFT) for practical, fast implementation on computers the technique has changed very little from its' initial derivation by Jean Baptiste Joseph Fourier (1768–1830) in 1807 [141], and is now an integral part of modern physics and digital signal processing.

The transform is a lossless rearrangement of the information carried by the original function and plotting the resulting distribution function reveals of spectrum of frequencies [142]. The DFT can be mistaken for a compression algorithm since the magnitude of the peaks are of most importance for most users and the information between the peaks are often disregarded as uninspired noise. However, the DFT is not a compression algorithm since the inverse of the transform will yield a perfect copy of the original continuous function.

Different groups of users of the Fourier Transform often have their own definition of the algorithm depending on the application and the heritage of their field of research. The Fourier Transform $F(\nu)$ and its inverse $f(t)$, are defined by the following pair of integrals:

$$F(\nu) = A \int_{-\infty}^{\infty} f(t) e^{-2\pi i \nu t} \, dt \tag{3.1}$$

$$f(t) = B \int_{-\infty}^{\infty} F(\nu) e^{2\pi i \nu t} \, d\nu \tag{3.2}$$

Where A and B are constants such that $A * B = 1/(2\pi)$, t is the sample time and ν is the frequency of the signal. The Fourier Transform is used to represent a continuous data set in terms of complex-functions of sine and cosine functions.

3.1.1.1 Discrete Fourier Transform

The Discrete Fourier Transform (DFT) is a computational method to estimate the Fourier transform of a function from a finite set of samples of that function. It is used because you can never take more than a finite set of measurements of data from any channel. Two important assumptions are that the function is bandwidth limited, so the value of the underlying function between the samples is reasonably represented by interpolating between the measured samples, and that the finite range of times over which you took your data are typical of the behaviour of the function outside that time interval. We can express the DFT as:

$$X(k) = \sum_{n=0}^{N-1} x(n) e^{\frac{-i2\pi kn}{N}} \tag{3.3}$$

Where N is the total number of samples, n is the sample number and $2\pi k$ relates to frequency f where $f = k/(n * t_s)$ and t_s is the period between successive samples. Taking Equation 3.3 at face value, the time superficially required to compute all N independent Fourier coefficients is order N^2:

$$\text{ExecutionTime} = \text{k}_{\text{DFT}}\text{N}^2 \tag{3.4}$$

3.1.1.2 Fast Fourier Transform

The Fast Fourier Transform (FFT), is an computationally superior algorithm for calculating DFTs that takes advantage of the symmetry of Fourier Transform Pairs. Cooley and Tukey [143] first demonstrated the usage of FFTs however, Gauss had already described the FFT as early as 1805 [144–146]. The time to calculate the FFT can be calculates as:

$$\text{ExecutionTime} = \text{k}_{\text{FFT}}\text{N}\log_2\text{N} \tag{3.5}$$

This faster method of calculating DFTs has made the FFT a staple in data processing as it lends itself to very large data sets. Applications span audio engineering, signal processing, image processing and much more.

3.1.2 Power Spectral Density

The Fourier transform is useful for deterministic function however, in the case where the input function is a unknown random time series ($s(t)$), the *power spectrum* or Power Spectral Density (PSD) is more advantageous. The PSD is an advancement on the Fourier Analysis whereby data is divided into segments consisting of equal number of samples. Data is windowed (see Section 3.1.3) and a DFT is calculated of each segment. The windowed DFTs are then averaged together to yield the final spectrum. This is known as the Welch estimate of the Power Spectral Density. Experimentalists of LIGO will often take the square root of the Welch PSD to obtain the Amplitude Spectral Density (ASD) which has units of $\sqrt{\text{Hz}}$. There are other methods to compute the PSD however, this is beyond the scope of this thesis. Discussion of PSDs can be found in Prabhu [147], Moses and Stoica [148], Kay [149], Marple [150].

$$S_{\text{ASD}}(f) = \sqrt{S^2_{\text{PSD}}(f)} = \frac{1}{\sqrt{2\pi}} \int_{-\infty}^{\infty} s_{\text{window}} * s(t) e^{-i2\pi f t} dt \tag{3.6}$$

3.1.3 Windowing

Windowing is a signal processing technique used when segmenting data used for DFTs. When using the DFT, one assumes that the input data is periodic about the segment length the user has selected. In reality, this is not the case and digital artifacts arise from the hard boundaries of the discrete segments of data. A windowing function is used to smooth the artificial features across all segments and suppress the contributions of the boundary glitches. There are many algorithms for calculating the segment with the most popular being the Welch method. The choice of window has a profound affect on the transform of the data. We demonstrate such affect in Figure 3.1 using the most common windowing methods to transform a slice of LIGO data. Here we have chosen to focus on the static 60Hz mains resonance line and it can be seen that the different choose of windowing affects the morphology of the signal peak. This becomes more problematic when one wants to extract information about the peak as one must not only assume the peak shape (i.e. Gaussian) but also include the windowing transform contributions. This problem becomes further exacerbated for non-stationary peaks. It is often best just to pick a single windowing function and stick with it throughout ones analysis as there is no best function, and the more common ones like Hanning are adequate for most purposes.

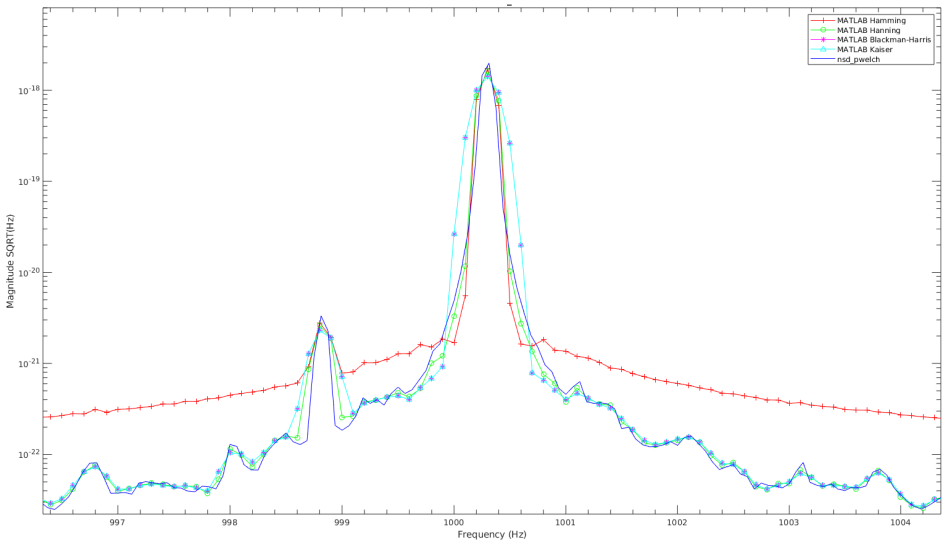

Figure 3.1: Using different windowing calculations for the same stretch of LIGO data in MATLAB along with a Welch method.

3.1.4 Frequency tracking and Phaselocked Loops

Phase lock Loops (PLLs) can take both analogue and digital form however all share the same basic principles - a Voltage Controlled Oscillator (VCO), Phase Detector (PD) and a Loop Filter (LF). The phase detector will compare the input signal to that of the VCO. An error signal generated by this is processed by the loop filter to adjust the VCO in order to minimise the error signal. A PLL is considered to be *locked* when the average input signal exactly matches the average VCO signal [151]. The error signal is driven to zero by the feedback control on the VCO however will never reach zero since each cycle of the loop will introduce phase noise into the system and the loop gain in the feedback path is not infinite. The PLL will be unlocked when the loop filter can no longer hold the PLL in a steady state.

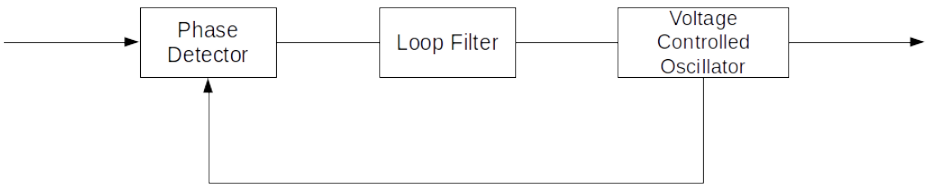

Figure 3.2: Basic diagram of a PLL.

PLLs are, by design, non-linear devices therefore, predicting their behaviour is a non-trivial process. The response of a PLL can be analytically expressed using a transfer function (TF), a ratio of polynomial expressions of coefficients. This effective method of signal processing notation allows system engineers to design and model as well as evaluate the various circuit configurations with ease.

3.2 IWAVE

3.2.1 Motivation

IWAVE [1] is a digital signal processing tool that can track resonant features even in noisy data streams. The core operation stems from phase lock loops however, in place of the counter or reference oscillator, an IIR filter is used to construct the reference signal. IWAVE produces simple outputs such as the demodulated phases of the tracked signal, a reconstructed amplitude estimate and error signal.

The core algorithm is written in C [152] and wrappers can build libraries for MATLAB, Python and LIGO CDS compatible C code. The C libraries used are the *libc* libraries that is compatible with most operating systems therefore, IWAVE has great flexibility across a wide array of machines and operating systems. The portability of IWAVE using this development approach takes advantage of the rapid processing speed of C whilst, for users that prefer the wrapped libraries, maintain the convenience of other programming syntax. This approach can be seen in libraries such as Python's *numpy* [153] libraries and MATLAB's *fft* libraries.

(a) IWAVE Filter

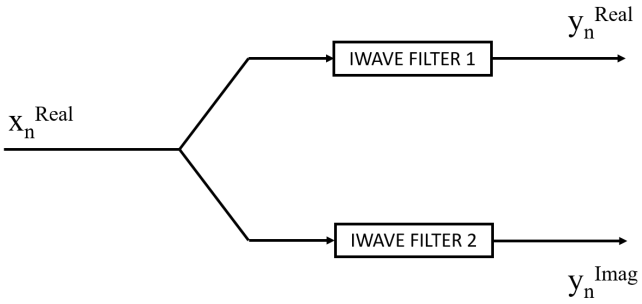

(b) Computer friendly

Figure 3.3: A basic block diagram of the IWAVE PLL algorithm. a) The IWAVE filter as viewed from an analytical viewpoint that takes a real input oscillation and yields a imaginary output informed by the input oscillation. b) The IWAVE algorithm configured in a more computationally friendly configuration. The two filters demonstrate how IWAVE produces real and imaginary outputs informed by the input oscillation.

There are many advantages of using IWAVE for tracking resonant features. One of the benefits of IWAVE is that it is relatively easy to use. There are only three inputs to the algorithm which are: (a) $x(t)$ input signal time series; (b) τ [seconds] the response time and, f_{guess} [Hz] the guess frequency. Another advantage is the algorithm operates within the time domain therefore, it is possible to obtain the real-time frequency and amplitude estimates of the tracked resonant feature. However, unlike traditional PLLs, the absence of a VCO within IWAVE means that whilst the algorithm is acquiring lock, no additional noise is being injected into the data stream.

In the next section, we will review the maths of the core algorithm before exploring the how IWAVE can be used in various applications. This will not be an extensive derivation of the maths as this is covered in Daw et al. [1]. Furthermore, whilst the core algorithm has changed slightly, the detailed description of IWAVE

performance in Kennedy [154] remains relevant.

3.2.2 Theory of the IWAVE Algorithm

We start by choosing the $\mathcal{Z}$-transform as a method for transforming our real input data into real and imaginary parts. This is advantageous, over Fourier analysis like the DFT, since the $\mathcal{Z}$-transform has a unique property that it weights previous samples exponentially, alleviating the need for a windowing function. Therefore, we can express the $\mathcal{Z}$-transform, for a regularly sampled, τ_s, time series data series, x_t, as:

$$\mathcal{Z}_n(\xi) = \sum_{v=-\infty}^{n} x_t \exp([v-n]\xi) \tag{3.7}$$

Where v is the sample number and increases with time and $\xi = \omega - i\Delta$ is a complex number attributed to weighting the previous samples. Here ω weights the previous sample according to the sampling time (τ_s) and the user defined IWAVE response time τ. The relationship then follows $\omega = \tau_s/\tau$. The exponential taper in weighting of samples in the past has an e-folding time of 1/w samples. This formula allows you to calculate ω, and $1/\omega$ is how many samples back into the past you have to go before you encounter a sample that has been divided by 1/e. Moreover, the imaginary part, $\Delta = 2\pi f \tau_s$, is the resonant frequency of IWAVE in units of radians per sample.

An alternative way to represent the $\mathcal{Z}$-transform is by showing it as an IIR single input single output (SISO) first order IIR filter with imaginary terms in a recursion relationship:

$$y_n = e^{\xi} y_{n-1} + x_n \tag{3.8}$$

Here we show that the current input, x_n and the current output, y_n, are related by the previous output y_{n-1}. To prevent the recursion relation from diverging for very large n, we scale the input by $(1 - e^{-\omega})$ such that:

$$y_n = e^{-\omega} e^{i\Delta} y_{n-1} + (1 - e^{-\omega}) x_n \tag{3.9}$$

Equation 3.9 is the pure definition of the IWAVE filter and is a compact way to easily analytically find solutions to input since the response to an arbitrary waveform $x_n = e^{in\phi}$ will have eigenfunction solutions of the form $y_n = Ae^{i(n\phi+\theta)}$. However it is difficult to implement this in practice. Alternatively, we can express the filter a multi input multi output (MIMO) IIR filter with real terms. Recall the notation for expressing real and imaginary numbers:

$$y_n = y_n^R + i y_n^I \tag{3.10}$$

$$x_n = x_n^R + i x_n^I \tag{3.11}$$

Furthermore, recall the Euler formula:

$$e^{i\Delta} = \cos\Delta + i \sin\Delta \tag{3.12}$$

By substituting 3.10 and 3.12 into 3.9 we obtain:

$$\begin{pmatrix} y_n^R \\ y_n^I \end{pmatrix} = e^{-\omega} \begin{pmatrix} \cos(\Delta) & -\sin(\Delta) \\ \sin(\Delta) & \cos(\Delta) \end{pmatrix} \begin{pmatrix} y_{n-1}^R \\ y_{n-1}^I \end{pmatrix} + (1 - e^{-\omega}) \begin{pmatrix} x_n^R \\ x_n^I \end{pmatrix} \tag{3.13}$$

We introduce the sample delay operator z to show the relationship between previous samples more elegantly such that $y_{n-1} = z^{-1} y_n$. Orders of z result in

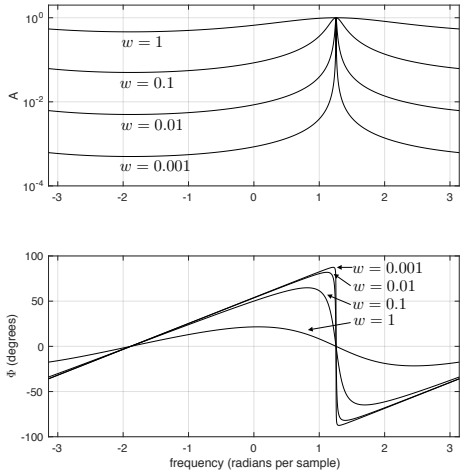

Figure 3.4: Response of IWAVE filter in open loop to a static input data. The ω parameter shows the different bandwidth of IWAVE, equivalent to changing τ. The larger the value of ω, the greater amount of broadband noise is pulled into the IWAVE. Reproduced from Daw et al. [1].

previous samples indicated by the power indices i.e. $y_{n-p} = z^{-p}y_n$. Multiplying out the brackets and collecting real and imaginary terms we arrive at:

$$\begin{pmatrix} y_n^R \\ y_n^I \end{pmatrix} = \Lambda \begin{bmatrix} \mathcal{H}_{11}(z^{-1}) & \mathcal{H}_{12}(z^{-1}) \\ \mathcal{H}_{21}(z^{-1}) & \mathcal{H}_{22}(z^{-1}) \end{bmatrix} \begin{pmatrix} x_n^R \\ x_n^I \end{pmatrix} \tag{3.14}$$

Where:

$$\Lambda = \left(\frac{1 - e^{-\omega}}{1 - 2e^{-\omega}z^{-1}\cos\Delta + e^{-2\omega}z^{-2}} \right) \tag{3.15}$$

and the components of $\mathcal{H}$ are:

$$\mathcal{H}(z^{-1}) = \begin{bmatrix} 1 - e^{-\omega}z^{-1}\cos\Delta & -e^{-\omega}z^{-1}\sin\Delta \\ +e^{-\omega}z^{-1}\sin\Delta & 1 - e^{-\omega}z^{-1}\cos\Delta \end{bmatrix} \tag{3.16}$$

From Equation 3.14, we see that the transfer function of IWAVE contains a z^{-2} component thus, the IWAVE algorithm is sensitive not only to the previous sample but the samples before that too. Furthermore, the output is decomposed into a real and imaginary parts. We can analytically solve for the magnitude $\mathcal{A}(\theta)$ and the phase $\phi(\theta)$ response to an arbitrary input static frequency, represented in radians θ as:

$$\mathcal{A}(\theta) = \frac{1-e^{-\omega}}{\sqrt{1-2e^{-\omega}\cos(\Delta-\theta)+e^{-2\omega}}} \tag{3.17}$$

$$\phi(\theta) = \arctan\left(\frac{e^{-\omega}\sin(\Delta-\theta)}{1-e^{-\omega}\cos(\Delta-\theta)}\right) \tag{3.18}$$

In a real case scenario, an input data stream will contain the real part of the oscillation. We represent this by saying $x_n^I = 0$ and $x_n^R = \cos(n\Delta)$. If we plot the real and imaginary parts of the IWAVE outputs, we obtain Figure 3.5. By substituting this into Equations 3.17, it can be shown that (see the mathematical addendum by Hollows et al. for full derivation in Daw et al. [1].) the response of IWAVE is:

$$y_n = e^{\frac{i\phi}{2}}\left(\frac{(1+\mathcal{A})}{2}\cos\left(n\Delta - \frac{\phi}{2}\right) + \frac{i(1+\mathcal{A})}{2}\sin\left(n\Delta - \frac{\phi}{2}\right)\right) \tag{3.19}$$

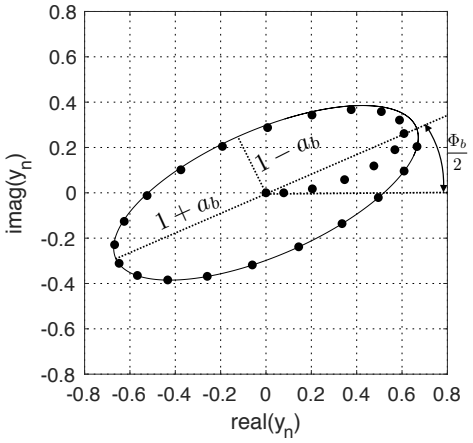

Figure 3.5: Output of IWAVE with a real input data series. Each solid dot is the outputs of y_n and the solid line is traced over to show the ellipse. Reproduced from Daw et al. [1].

As time elapses, the real and imaginary outputs of IWAVE will trace an ellipse with an inclination angle $\frac{\phi}{2}$, semi-major axis $(1+\mathcal{A})$ and semi-minor axis $(1-\mathcal{A})$. An ellipse is indicative of an imbalance of the between the real and imaginary parts of the IWAVE outputs from the recursion relationship from Equation 3.9. Balancing the real and imaginary parts requires transforming the output such that the components of the output trace out a circle. The real and imaginary outputs, now called the D and Q phase respectively, are the in-phase and 90° out of phase to the input oscillation with equal amplitude. The transform is a three step process:

- Rotation of the ellipse to such that the semi-major axis is parallel to the x-axis.
- A shear matrix that transforms the rotated ellipse to a circle
- A rotation of the sheared ellipse to correct for the phase rotation in the first step.

Mathematically, we can write this as :

$$\begin{pmatrix} D_n \\ Q_n \end{pmatrix} = \begin{pmatrix} \cos(\alpha) & \sin(\alpha) \\ -\sin(\alpha) & \cos(\alpha) \end{pmatrix} \begin{pmatrix} \frac{2}{(\mathcal{A}_f+\mathcal{A}_b)} & 0 \\ 0 & \frac{2}{(\mathcal{A}_f-\mathcal{A}_b)} \end{pmatrix} \begin{pmatrix} \cos(\beta) & \sin(\beta) \\ -\sin(\beta) & \cos(\beta) \end{pmatrix} \begin{pmatrix} y_n^{\Re} \\ y_n^{\Im} \end{pmatrix} \tag{3.20}$$

We then have it that we can express the amplitude estimate as the least square sum of the D_n and Q_n phases, $A = \sqrt{D_n^2 + Q_n^2}$. The frequency estimate is given by the complex number of the D_n and Q_n phases, $f_n = D_n + iQ_n$. The phase output of IWAVE is the Pythagorean angle of the D_n and Q_n phases, $\phi_n = \arctan(Q_n/D_n)$. This concludes the main part of IWAVE algorithm. In the following sections, we will see how IWAVE implements a feedback loop in order to phase lock to characteristic resonances and thereby behave like a Phase Locked Loop frequency tracker.

3.2.3 Configurations of IWAVE

IWAVE has three main configurations: open loop; closed loop (Single IWAVE) and, parallel closed loop (Multi-IWAVE). The merit of each configuration will depend on the task one employs IWAVE for. In general, if the input data stream is very

noisy and/or the target feature is closely spaced to other resonances, the Multi-IWAVE is the recommended configuration. Conversely, if the target resonance has a sufficiently large SNR such that it is the most prominent feature within the broadband signal then the single IWAVE is more suitable.

Computationally, one would prefer to use the single IWAVE filter over the Multi-IWAVE to reduce the computation time. This is particularly important for real-time data processing such as the front end of LIGO, ADMX or FPGA deployment. Should a user want to use only the single IWAVE tracker with noisy data streams and large broadband noise, data reduction techniques can be implemented. Using one of or a combination of pre-filtering, mixing and subtraction can clean the up the input data sufficiently for a single IWAVE filter.

3.2.3.1 Open Loop

In open loop, it is possible to evaluate the characteristics of the IWAVE filter resulting from the input parameters. Specifically, the response time τ, has the greatest impact on IWAVEs behaviour. In open loop, the feedback part of the algorithm is bypassed therefore, the description of the filter in Section 3.3.2 is appropriate.

3.2.3.2 Single IWAVE

In the closed loops state, shown in Figure 3.6, we require a metric to determine the divergence of frequency from the input harmonic. In other words, we are seeking a suitable error signal we can exploit in order to modulate the IWAVE resonator to converge onto a input oscillation. We use the response time (τ) of the IWAVE filter as our metric since this is the main parameter that shapes the response of the filter.

We compare the accumulation of the departure in phase ($\delta\phi$) is summed with the homodyne IWAVE phase with the imaginary estimate of the input data to obtain the modulated error signal. This can be as the trigonometric relationship as:

$$\mathcal{A}\cos(n\Delta)\sin(n\Delta) = \frac{\mathcal{A}}{2}\sin(2n\Delta) \tag{3.21}$$

We see with this relationship that there is a pure harmonics at twice the input input harmonic ($2n\Delta$). This harmonic is not present in the amplitude and phase outputs This can be removed by using a second IWAVE filter but only implementing the imaginary part of the IWAVE filter. In the second IWAVE filter, the ($2n\Delta$) harmonic appears as a DC offset to the input signal therefore a simple subsitution removed the harmonics from the final output. This output is now a complete measure of the departure of phase between the IWAVE resonator and the input data thus yields a usable error signal ($\delta\phi_n$).

Whilst we now have a suitable error signal, we must tell the IWAVE filter how to handle the modulation in order converge to a central value. This is controlled with our choice of the closed loop feedback Gain ($\mathcal{G}$) without which the algorithm cannot lock. This calculated as:

$$f_{out} = (f_{in} - f_{out})\left(\frac{2\pi}{s}\frac{s\tau}{1+s\tau}\mathcal{G}\frac{1}{s\tau}\frac{1}{2\pi\tau}\right) \tag{3.22}$$

Where f is the frequency, $\frac{2\pi}{s}$ is the accumulation of phase with $s = 2\pi i f$. Evaluating the closed loop transfer function $H(s)$ we arrive at:

$$H(s) = \frac{f_{out}}{f_{in}} = \frac{\mathcal{G}\tau^{-2}}{s^2 + s\tau^{-1} + \mathcal{G}\tau^{-2}} \tag{3.23}$$

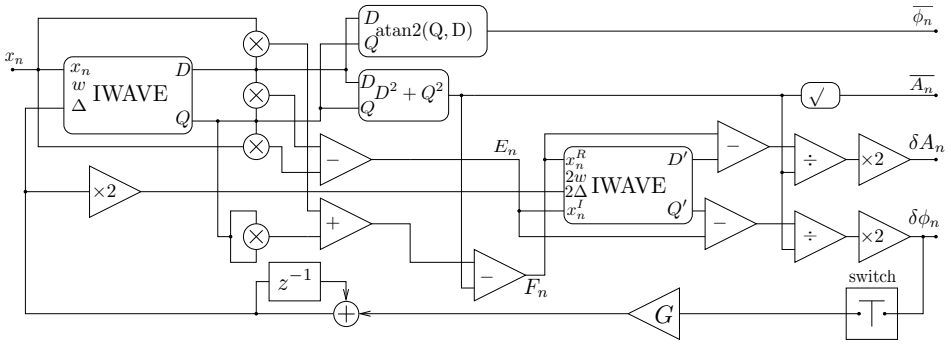

Figure 3.6: Schematic of the IWAVE PLL

The resulting quadratic transfer function is indicative of a driven damped oscillator. We can solve to underdamp, overdamp or critically damp the system. Overdamping would result in the IWAVE filter converging faster but may overshoot and introduce more noise in the final frequency output. Underdamping will result in slower convergence with little to no overshoot at the expense of increase time to converge. Finally, critical damping is a middle ground between the previous two regimes that balances speed with noise contribution. We choose to critically damp the system therefore, we set $\mathcal{G} = \tau_s^2/4\tau^2$. Substituting this into 3.23 we obtain the critically damped closed loop transfer function as:

$$H(s) = \left(\frac{\frac{1}{2\tau}}{s + \frac{1}{2\tau}} \right)^2 \tag{3.24}$$

Since we have established that τ is mainly responsible for IWAVE response, we must consider the best way to set the parameter. Firstly, one must have an estimate of the rate of change of the target frequency δf. Whist this is not critical, it will help with optimising IWAVE performance. If one chooses a $\tau < \delta f$, IWAVE will have a large bandwidth thereby ingesting more broadband noise however, IWAVE will have the flexibility to maintain lock on rapidly moving δfs. For $\tau > \delta f$, IWAVE will have a narrow bandwidth therefore less susceptible to broadband noise however IWAVE will struggle to catch rapid δfs thus, more suited to slow or static resonances. For the most part, evaluating τ is an empirical exercise of minimising the error signal. More recently, a method has been devised to find the optimum τ by large number of simulations of IWAVE performance to different δf using swept sinusoidal injections and various τ values. Using χ^2 statistics, as the metric of performance that assumes $2\pi^2\tau^2(df/dt)^2 > 1$, minimising yields the optimal τ as:

$$\tau_{opt} = \frac{1}{6\sqrt{288\pi^4 f^2 (\frac{df}{dt})^2}} \tag{3.25}$$

For a more in-depth study into τ optimisation, see Daw et al. [1].

3.2.3.3 Parallel (Multi) IWAVE

For scenarios where the input signal contains multiple harmonics, and in some cases the harmonics are closely spaced in frequency, it may be more suitable to use the multi-IWAVE filter. Here, IWAVE is configured such that multiple single IWAVE filters are connected in parallel. Cross subtraction between the IWAVE filters removes tracked harmonics from the data stream within the feedback loop,

alleviating cross talk between the filters. Demonstrated in Figure 3.7, a multi-IWAVE filter containing two filters will be able to isolate two characteristic frequencies for and input data stream. It is also possible, though not show in 3.7, to extract a *cleaned* data stream as one of the outputs of the multi-IWAVE outputs. Here, cleaned means a channel where all IWAVE cross subtraction has been implemented therefore, any residual harmonics within the output data is a feature not tracked by IWAVE.

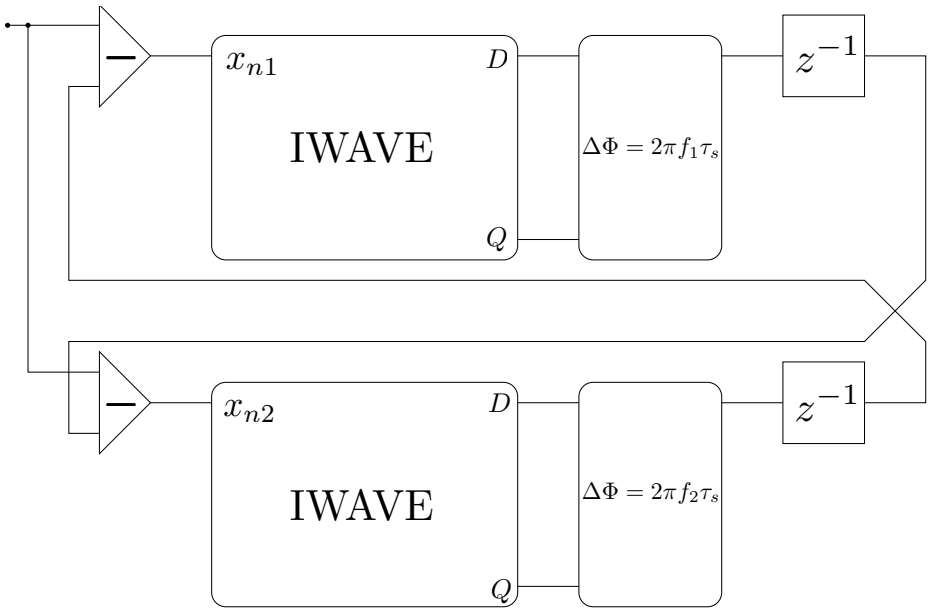

Figure 3.7: Schematic of the IWAVE filters used in parallel.

Construction of the multi-IWAVE filter is done using the constructor command such that the usual IWAVE arguments are required (time series data and τ) as well as a vector of frequency guesses. Moreover, there is an added feature such that the user can turn on and off the outputs. This is useful for when combating large number of IWAVE filters and large amounts of input data.

The advantages of using the multi-IWAVE filter can be summarised as follows:

- Reduces the need for complicated pre-filtering of the data.
- The cross subtraction can be used as a cleaning algorithm for input data streams.
- It is possible to store all the individual parameters of all the IWAVE filters for batch or parallel computing.
- Frequency limits can be imposed such that if one of the line trackers wanders outside of the limits then that line tracker is reset.

However, there are limitations to the mulit-IWAVE tracking. These are:

- Only one response time, τ, can be used for all IWAVE filters. The implications of this is that if there are harmonics that are non-stationary and have different time constants, it will be difficult for IWAVE to reliably lock onto all the harmonics.
- For every IWAVE filter in the parallel circuit, a copy of the input data is made. Therefore, for offline analysis of large data sets, the memory requirements can rapidly grow. This can slow down computation time and

techniques such as batch processing, GPU processing or parallel computing may be required.

3.2.4 Examples of IWAVE

3.2.4.1 Use on parallel computing

It is possible to use IWAVE on parallel (grid) computers. However, one limitation of IWAVE is that it is designed to be used on live data and and run in series with the data stream. However, when processing large amounts of data offline (not live), we can take advantage of (grid) computer clusters to parallelise our analysis to rapidly analyse the data. This involves splitting up large stretches of data into smaller, more manageable, pieces and analysing the data simultaneously across many computing cores. After the analysis, one can stitch the data and analysis segments back together, as if the analysis had been executed uninterrupted on the original stretch of data. However, since IWAVE requires the history of its previous states in order to calculate the next state, we must adapt the way we use IWAVE for grid computing. Here the user must store the previous IWAVE output and pass this filter state into the next IWAVE analysis segment. If we do not do this, IWAVE will initialise using the user input guess parameters. Figure 3.8 demonstrates the effect of the IWAVE filter continually re-initialising at each new analysis segment without passing the previous segment into the new analysis segment. Therefore, one must pass the last filter state into the next analysis segment, this is akin to running the IWAVE filter over an unbroken stretch of the segmented data. As a result, this behaviour complicates how IWAVE can be used on grid computers and techniques such as overlapping analysis segments in order to suppress re-initialisation features. The overlap time can be evaluated by monitoring the error signal until it reaches a magnitude that shows IWAVE is locked. This can also depend on the value of τ that is used therefore, this applications will vary depending on the data that is being analysed.

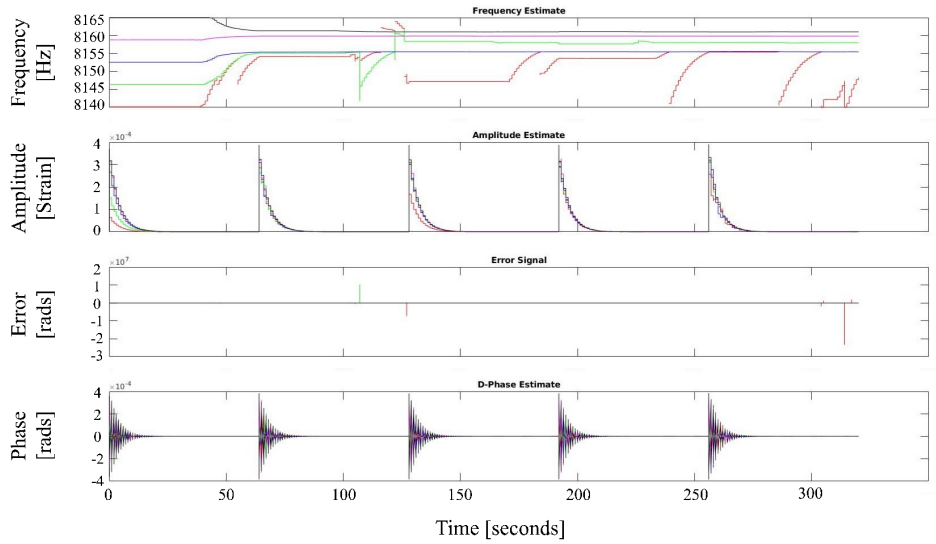

Figure 3.8: Example of using IWAVE multi-line tracking but not passing the last IWAVE filter state into the next chunk of analysis.

3.2.4.2 Multi-Line Tracking of Violin Modes

We can show how the multi-line tracker is effective by tracking the second order violin modes at LIGO Livingston (LLO). The violin modes are a good example since they are a group of tightly spaced harmonics that contain doublet peaks. We take a small stretch of data, shown in Figure 3.9 and plot the power spectra to show the forest of peaks we are dealing with. There is a lot of instrument noise in the LIGO bandwidth including the 60Hz mains line and its harmonics that could interfere with IWAVE tracking therefore, we can filter the data before passing this into IWAVE.

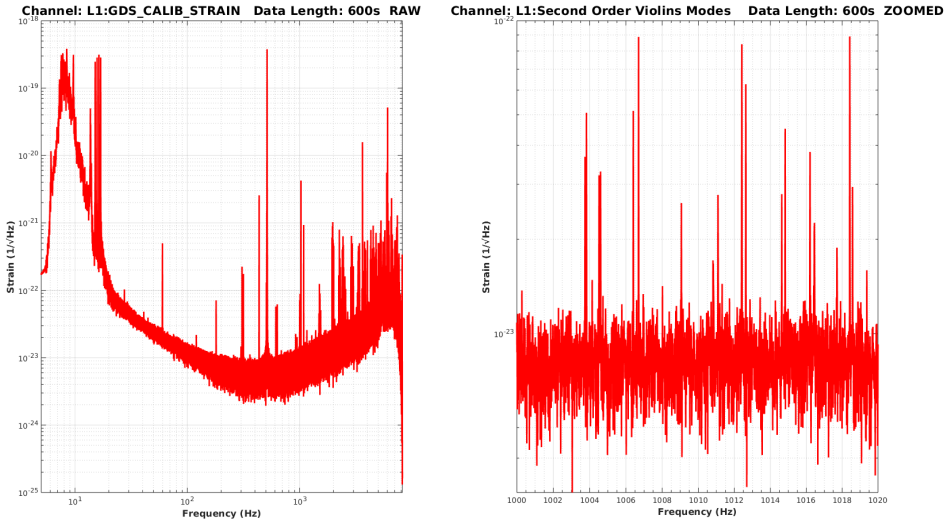

Figure 3.9: Raw data from LLO. On the left we have a power spectra of the science channel from LIGO called L1:GDS_CALIB_STRAIN plotted for 600 seconds of data. Here, the term raw means we have not processed the data in any way. On the right we have zoomed into the Second Order Violin Modes. We can see there are is a forest of peaks from the violin mode harmonics.

Since the data is very crowded, we can pre-filter the data to remove all but the desired features from the LIGO strain. In this example, a narrow bandpass filter, shown in Figure 3.10, to isolate the second order violin modes. The smooth phase response of the filter shown in the bode plot keeps the passband more or less unaffected in phase therefore, we can treat the phase delay as negligible from the filter. To further demonstrate how the filter affects the input data, Figure 3.11 compares the filtered data along with the original input data

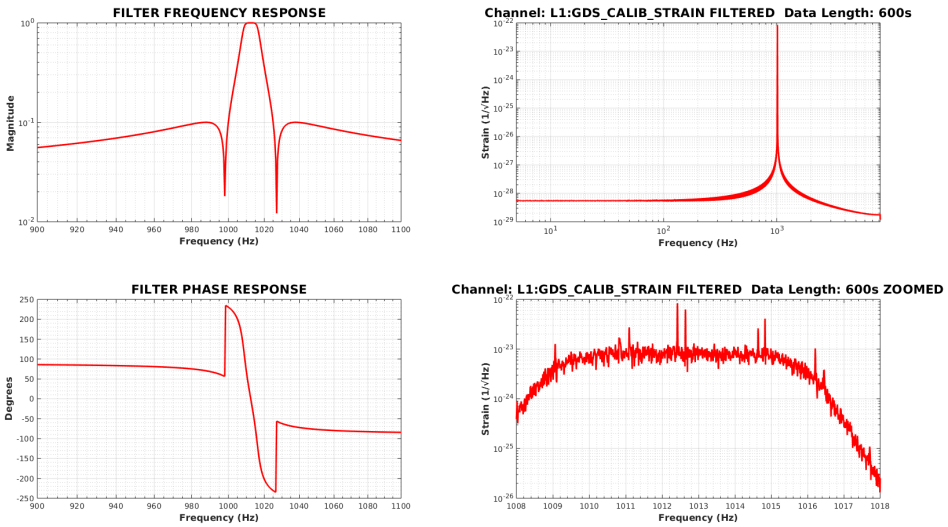

Figure 3.10: Filtering the data. The left two panels are Bode Plots of the filter we use to apply to the data. The result of applying the filter is given in the top right panel. The lower right panel is a zoomed in look at the passband to show the narrow bandwidth we retain after filtering.

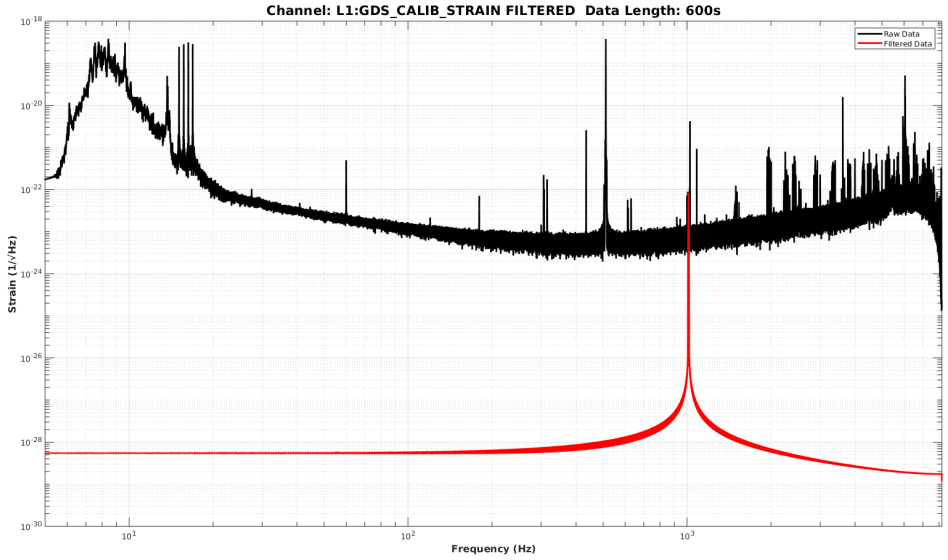

Figure 3.11: Compare the input data with the filter. The top black trace shows the raw data from Figure 3.9 and the lower red trace shows the filtered data and the narrow bandwidth we have retained.

Finally, we can pass the filtered data into IWAVE. Here we use four line trackers to look for the violin doublet at $\sim$ 1012 Hz. With the multi-line tracker, we can restrict IWAVE to look within frequency limits. If a line tracker goes beyond the user limits, it is reset. In Figure 3.12, two line tracker have locked onto the violin doublet whilst the remain two have found other resonances in this passband. The other two line trackers act as cleaning filters ergo making the trackers that have locked into the violin modes more stable.

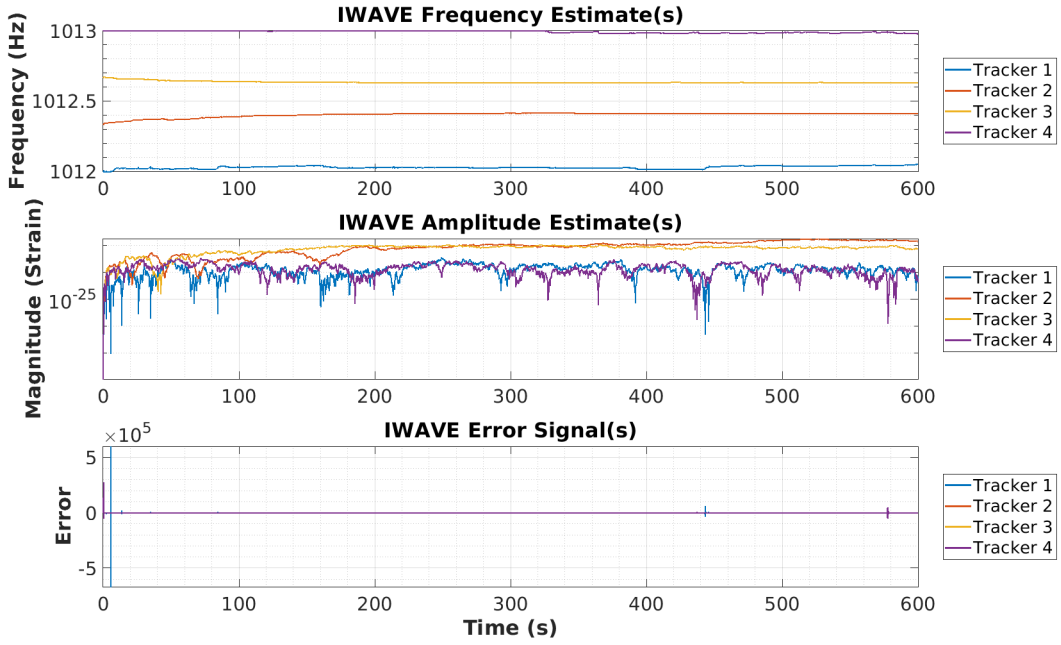

Figure 3.12: Final output after evoking IWAVE tracking. The top panel is the frequency output of IWAVE, the middle panel is the amplitude estimate of the frequencies and the lower panel is the error signal from IWAVE.

3.2.4.3 Upgraded Line Trackers on the LIGO Front End

The LIGO front end has a version of IWAVE installed from Kennedy [154]. Here, we implement the improvements outlined in 3.2.2, which include an improved feedback gain. One restriction of building software models for the LIGO front end is that the IWAVE filters need to be pre-built before deployment. In other words, you are unable to dynamically change the number of line trackers. Therefore we chose to build IWAVE with four line trackers (Figure 3.13). This is achieved by modifying the underlying C code of IWAVE and building a custom SIMULINK block for the LIGO RTG. We chose four line tracker because most signals appear in groups of four. Moreover, as discussed in Section 2.1.2, there is a computational limit to the number of cycles that a model can use therefore four line tracker is a good balance between computational cost and performance.

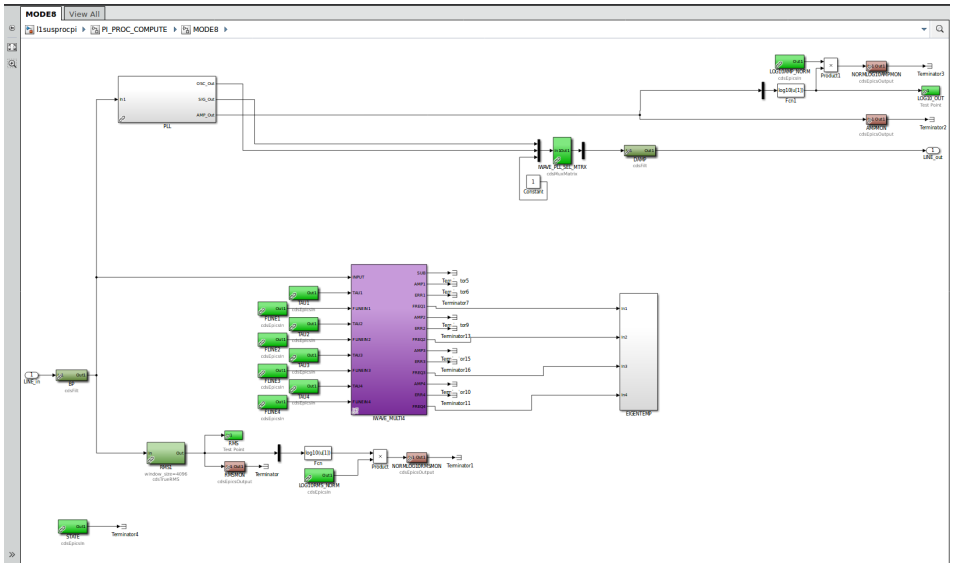

Figure 3.13: The IWAVE front end model viewed in LIGO RTG SIMULINK model viewer. The top blocks are a traditional PLL implemented by LIGO and the lower block is the upgraded four line tracker.

3.3 Conclusion

IWAVE has been exercised in a number of LIGO projects. Applications include: Characterisation of the violin modes of the glass fibres [155]; Real-time tracking of parametric instabilities [156] and, cleaning strain data for GW search analysis [156].

IWAVE has seen successful deployment in industry in a variety of situations. A medical implementation of IWAVE has seen the algorithm being used to track the magnetic field lines generated by the human heart in Magnetocardiography (MCG) data. There are many different electrocardiogram (ECG) signals measured by the MCG machine in addition to large amount of noise due to the hospital environment. IWAVE is employed to track electrocardiogram (ECG) signals and is assisted with a reference signal therefore IWAVE is capable of tracking signals with a SNR < 1.

IWAVE is a useful alternative for traditional PLLs since the absence of a VCO in the IWAVE algorithm means that, whilst IWAVE is idle, no extra noise is injected into the system. Without the reliance of a VCO, IWAVE is unaffected by VCO slips - a glitch resulting from a mis-count in the VCO timing circuit. Additionally, the simplistic design of the IWAVE algorithm can be analytically expressed and easily modelled. This means that the user only has one tunable parameter available to them (the response time τ), thereby simplifying usage an reliability of the algorithm. Furthermore, the core library of IWAVE, written in C, is easily portable to almost any computer system and is lightweight enough such that it can be built on wide variety of operating systems and computer architectures with minimal to no alteration in performance. The additional benefit of being written in C, it is fast and can be implemented multiple times for real-time computation.

Chapter 4

Thermal Transients of the LIGO Test Masses

Sections 1 and 2 introduced the requirement for precise control over the main laser in addition to the large amounts of laser power in the arms in order to achieve the sensitivity for GW detection. The LIGO recycling cavities build up sufficient laser power that enables GW detection. As a result of these cavities, the LIGO test masses are engineered to withstand such laser power. Mechanically, this is achieved by the high purity of the bulk material of the test masses, surface curvature and utilising specialised mirror coatings. Moreover, the Thermal Compensation System (TCS) [157], is a set of peripheral systems, that attempt to further mitigate heating effects. These systems are the ring heaters, electrostatic drive (ESD), CO_2 laser, the Harmann Wave front sensor and Acoustic Mode Dampers (AMDs). Inherently, laser power is absorbed by the test masses leading to thermo-elastic expansion of the test mass. This can change the radius of curvature of the test mass promoting higher order modes to build up within the cavity as well as increasing the scatter light losses. Moreover, defects in the mirror coating, known as point absorbers, will absorb large amounts of laser power in a highly localised area.

Understanding the thermal performance of the LIGO interferometers is increasing in importance as the instrument approaches its theorised sensitivity. The thermal noise is soon to become a limiting factor in the sensitive region of the LIGO spectrum, with quantum noise being the other main limitation. Whilst squeezing has proved to overcome the quantum limit, a robust method for mitigating the thermal noise has yet to be implemented. This is mainly due to the many complications in achieving such a goal since it takes a long time to verify the effectiveness of the solutions. Such solutions are improved mirror coating, improved test mass thermal modelling, non-invasive and low noise thermal monitoring system. Furthermore, as we gain more experience operating $\sim$ km scale interferometers, the length of unbroken lock stretches increases. Here, an lock stretch means a period of time whereby the interferometer is stable (known as low noise) and collecting science data. Stability is achieved by holding (controlling) the long arm cavities on resonance with the main interferometer beam. As such, new transients become apparent in the main strain data such as day-night cycles. Monitoring these transients has been crudely attempted, such as the calibration lines and the time-dependent correction factors. However, over long lock stretches, the accuracy of the corrections diverge ultimately leading to a mis-calibration. This was see in LIGO Hanford which resulted in a new calibration model being made and a crude correction factor to be applied to the affected data to fix the transient. Therefore, a more robust thermal monitoring system is required that could feed into the calibration pipeline to prevent future errors.

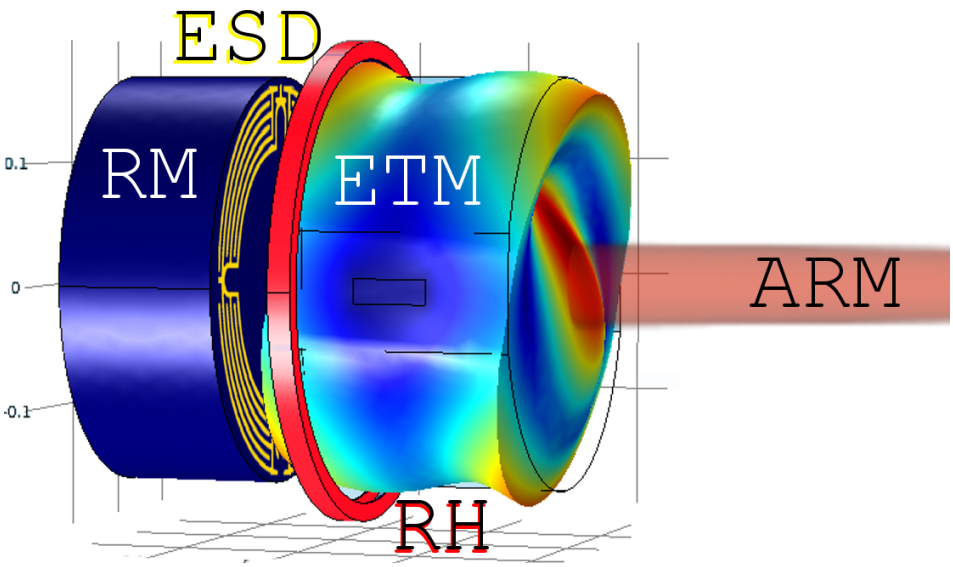

Figure 4.1: The COMSOL model of the TCS system. The Reaction Mass (RM) is modelled to hold the electrostatic drive (ESD) actuator. The ring heater (RH) surrounds the back end of the End Test Mass (ETM) and the main interferomter beam is modelled from the resonant arm cavity. The shape on the ETM is an exaggeration of one of the body modes that can be excited from coupling to the TEM mode of the main laser. Credit: Blair [9].

In this section, we shall explore the main sources of heating in the LIGO interferometers and how, though the use of IWAVE, we could provide useful metrics for improving the LIGO TCS.

4.1 Heating of the LIGO Suspended Optics

Whilst a brief introduction was given for thermal noise in Section 2, we will examine the effects of thermal heating of the LIGO optics leading to the development of a preliminary thermal monitoring system. Test mass heating is mainly attributed to losses in the FP cavity due to absorption of laser power by the main optics (ETMX, ETMY, ITMX, ITMY). Uniform and differential mechanisms contribute to the losses. Uniform losses are spatially invariant (equal to or greater than the main Gaussian beam) and despite the highly reflective (HR) surface mirror coatings, some absorption still occurs. Differential are spatially dependent (smaller than the main Gaussian beam) and is greatest a the centre of the Gaussian beam spot where laser intensity is greatest.

4.1.1 Thermal Control System

Given the high amounts of stored laser power in the IFO arms, it is natural that the optical surfaces will absorb some of this power. The ETMs are coated in a bilayer of amorphous SiO_2 and Ta_2O_5 to a thickness $\leq 6\mu$m [158]. It is expected that a 0.5ppm of laser power is absorbed in a Gaussian spatially distributed profile by the HR surface which equated to ~ 375mW. A thermal gradient across the optics creates a thermorefractive substrate lens resulting in thermoelastic deformation of the HR surface [159]. This reduces the stability of the FP cavity as a result of the main beam wave front being distorted by the thermally lensed optic. These effects introduce the following challenges for robust and stable IFO operation that arise

from the thermal effects:

- Parametric instabilities. This will be further discussed in Section 4.1.2
- Radiation pressure induced angular control noise.
- Reduced GW signal amplification.
- Increased photo-diode readout noise resulting from:
  - Reduced power at the beam splitter because of poor mode-mismatching from each arm.
  - Scattered (stray) light reflected into the anti-symmetric port causing elevated shot noise.
  - Local control loops such as local damping servos on the optics perform sub optimally in the presence of scattered light due to thermal lens effect.
- Increased alignment control noise from radiation pressure induced torques on the optics.
- Increased intensity (amplitude) and frequency (phase) noise coupling at DC readout.

The thermal control system (TCS) [157] is an assembly of control systems, sensors and actuators that aim to mitigate the thermal effects without additional strain noise. The system includes a CO_2 laser, a ring heater, Hartmann Wave front Sensor and the electrostatic drive (ESD). The ring heaters heat the edges of the optics to reduce the temperature gradients the lead to the thermo-optic lenses. During O3, the ring heater were set to a constant value in order to maintain a constant thermal profile for the test mass, minimising the thermal lens caused by thermal heating of the main laser [3]. The CO_2 laser provides additional localised heating to target regions on the optic to mitigate differential heating. The set point of the ring heater was characterised during the engineering runs and updated during the science run of O3. Characterising the thermal response of the test masses required a thermal injection, usually delivered by the ring heater, and the shift in the eigen-body mode frequencies were tracked over the course of several hours - typically 12-24 hours. Cooling the optics is an area of active research that is proposed for AdvLIGO+ and Voyager so it will be important to have accurate temperature measurements and models of the suspended optics.

4.1.2 Parametric Instability

The LIGO test masses have mechanical resonances that couple with the main laser. TEM modes of the main laser can excite the mechanical resonances of the test mass that beats with the main laser and enters a growing feedback loop - in the same way an one gets undesirable feedback from an electric guitar and amplifier. Such as the analogy described, in LIGO the higher order TEM modes and mechanical modes feedback to one another causing growing instability in the interferometer - though the controls systems and actuation actively trying to resist the induced motion and mode mis-matching. Ultimately, the instabilities can grow large enough to overcome the controls and the interferometer looses lock. This was formerly known as parametric instability and Evans et al. [160] showed it can be expressed as:

$$R_m = \frac{8\pi Q_m P}{M\omega_m^2 c\lambda_0} \sum_{n=1}^{\infty} Re[G_n] B_{m,n}^2 \tag{4.1}$$

Where, R_m is the parametric gain, Q_m is the quality factor of the test mass body mode m. P is the power in the fundamental optical mode, M is the optic mass, c is the velocity of light, λ_0 is the wavelength of light, ω_m is the body mode angular frequency, G_n is the transfer function for the recombination of light scattered that originated from the optic surface and $B_{m,n}$ is the overlap parameter with the n^{th} optical mode. With most of the parameters in Equation 4.1 being fixed, one can see that the parametric gain increases proportionally to laser power. Blair [9] is a detailed investigation into the theory, measurement and modelling of parametric instabilities. The test mass form factor, modelled in COMSOL, helps to identify the characteristic frequencies and the shape of the test mass that couples with the resonance [161, 162]. LIGO Livingston is currently better characterised, with 34 modes identified and confirmed, whereas LIGO Hanford only has around 20. Experimental verification of the modes is difficult. Currently, the best method of mode identification involves measuring a long period ($\sim$30 hours) of kHz broadband data and matching frequencies whose δf are similar. This is challenging because at these high frequencies, the data is contaminated with forests of overlapping instrumental overtones, some of which mask the desired test mass modes. Furthermore, the fastest data channels, sampled at 65535 Hz, means only modes up to 32 kHz can be identified before hitting the Nyquist frequency. Higher modes are aliased down, sometimes multiple times, and are lost in the anti-aliasing filters. Overall this technique is a manual effort since and automation requires a reliable method to identify (track) frequencies. IWAVE lends itself perfectly as it can be used for subtraction of unwanted frequencies, tracking of desired resonances that can be implemented autonomously.

Acoustic modes are tightly packed across the LIGO bandwidth with many of the higher order modes overlapping. In some cases, exciting one mode can drive the resonance of another mode. In addition, damping certain modes can lead to other modes becoming excited therefore, a large array of filters and damping must be employed in order to fully suppress the body modes [9, 163]. With the addition of the resonant mode dampers (Parametric Instability dampers) [163, 164] affixed to the test masses, these instabilities are largely suppressed. Before the dampers were installed, the ESD was used to drive the test mass in order to counter the instabilities. The MEDM control screen, Figure 4.3, contains the front end models that could track and damp up to 24 modes.

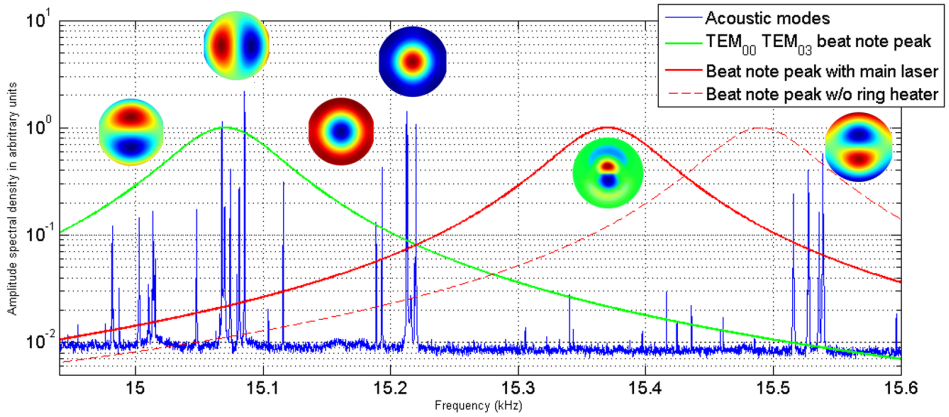

Figure 4.2: During LIGO first observing run, parametric instabilities were observed. Five test mass body modes shown here with their form factor. Image credit: Blair [9].

Whilst the most problematic PI modes have been addressed with the PI dampers, other modes may still pose a threat. Therefore, it is still useful to keep the front

end infrastructure in place, especially as LIGO increased its laser power, to damp new modes that will be rung up. Moreover, the software architecture developed to damp modes, Figure 4.3, can serve as a useful platform for more sophisticated real-time thermal monitoring and we put this to good use in Section 4.2.

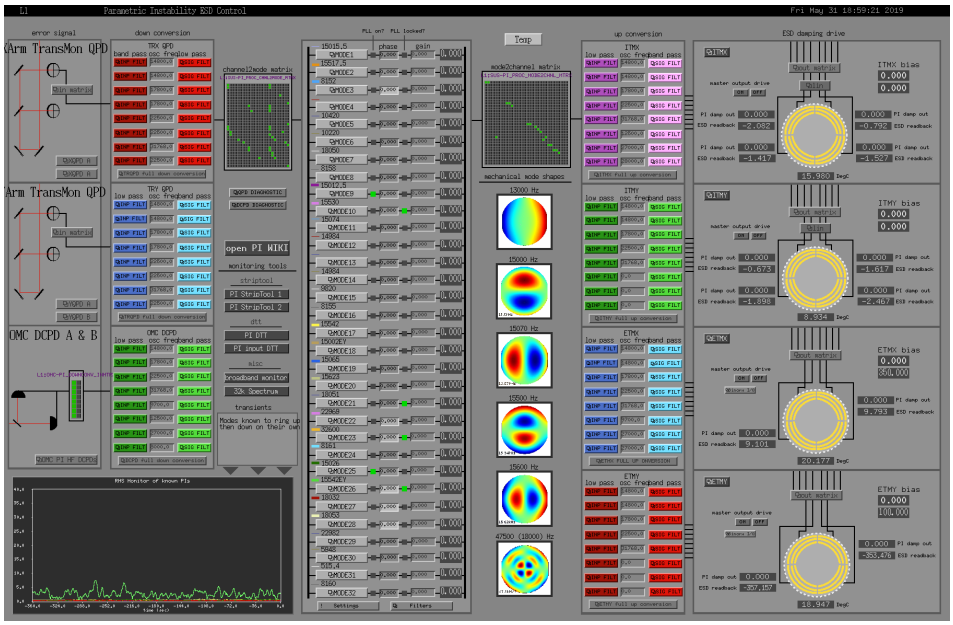

Figure 4.3: LLO parametric instability MEDM control screen that interfaces with the LISUSPROCPI LIGO RTG model. The left hand side is where data is piped in form the QPDs which then can be fed into a bank of local oscillators. These mix the signal down making it easier to isolate particular frequency bands without using high latency filters. The middle contains 24 modes that each hold a IWAVE line tracker. The right side has another bank of local oscillators to mix the signal back up to the original frequency which can then be send to the ESD drive.

4.1.3 Point Absorbers

Point absorbers are the mainly attributed to imperfections in the mirror coatings. The main source of contamination has been found to be microparticles of aluminium however, other sources of contamination on the mirrors arise such as dust, skin and fibres. These are believed to be deposited during the inspection process [165] and in-situ cleaning of the mirror surface prior to final closure of the HAM module largely removes most of the surface contaminants. The most troublesome point absorbers are found to be deeply ingrained into the optic surface, most likely during the HR coating process [165]. Point absorbers absorb large amounts of the main laser power into a localised area of the test mass. These non-linear absorption of laser power cause thermal lenses. In extreme cases, the glass can fracture and shards of molten glass shower the local area. Moreover, point absorbers can scatter light out of the fundamental mode into higher order modes further reducing the cavity power and increasing stray light noise and parametric instabilities.

The Hartmann Wave front sensor is the main, *in-situ*, tool used to measure the wave front distortions [157, 159, 165]. The sensor has proved useful many times in the successful detection of point absorbers on an optic despite the low resolution of the measurements. The resolution is limited by the transverse spatial sampling interval ($\sim$ 7.5mm), therefore, features smaller than this are unresolvable [165]. Uncertainty in the position of the point absorber increases the uncertainty of the noise coupling models for ITM thermal lensing. Whilst current O3 noise budgets

show that laser intensity noise is not a limiting factor of the IFO sensitivity, with increasing laser power as part of planned upgrades, thermal effects will become more prevalent [165].

Currently, the only way to compensate for point absorbers, during an observing run, is to slew the main laser to a location on the test mass devoid of such imperfections. This has a detrimental effect on the the amount of recycling power stored in the FP cavities. Methods are being investigated to remove defects in the HR surface during the coating procedure or removal after coating through a combination of annealing and polishing as well as high frequency spatially dependent actuators are being investigated in order to tackle the non-linear surface deformations [165].

4.1.4 Stray Light

Stray light arises from light scattering out from the main beam, interacting with the surrounding subsystems and returning the encoded noise into the LIGO strain. Stray light produces combs of lines in the LIGO spectrum called scattering arches. The main mechanism of scattering arises from imperfections on the surface of the test masses that reflect power out of the main beam. The resulting light bounces around the chamber, encoding phase noise from the surfaces it reflects from. Some of the scattered light recombines with the main beam thereby encoding the noise into the main gravitational wave strain data stream.

4.2 Test Mass Thermometers

One of the biggest challenges facing the thermal controls systems is being able to precisely measure the in-situ test mass temperature. Many commercial and bespoke sensors are too noisy for operation in or around the LIGO test masses - as discovered by the temperature sensors located on the upper stages of the LIGO quadruple suspension. Ergo, a proxy measurement of the test mass temperature, using the resonant coupling characteristics of the test mass to the main laser, is possible. Here, we will demonstrate how IWAVE can accurately measure the body mode resonances to provide such a metric.

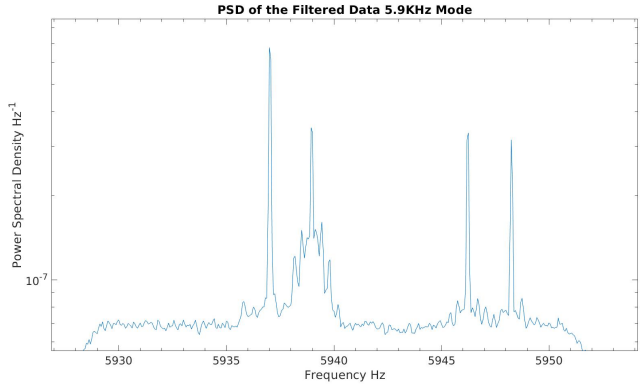

(a) 5 kHz Mode.

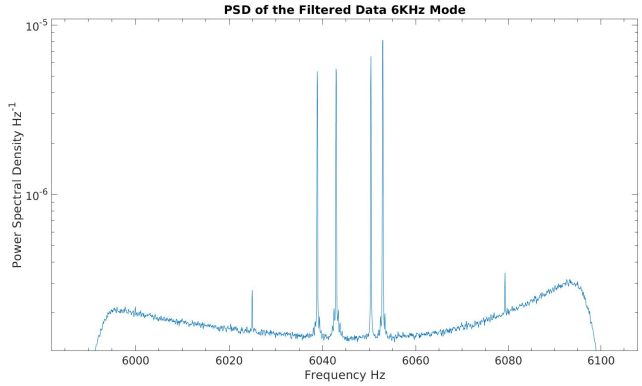

(b) 6 kHz Mode.

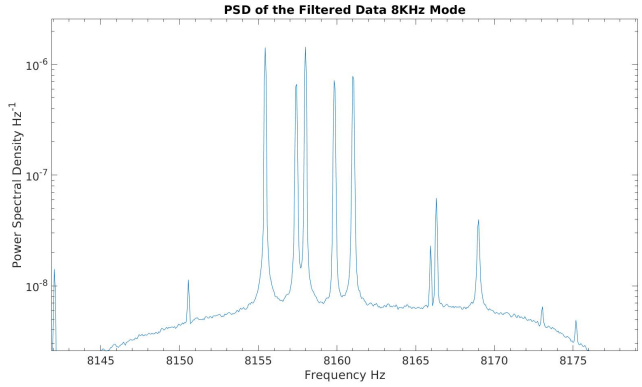

(c) 8 kHz Mode

Figure 4.4: Parametric Instabilities as seen in the LIGO strain spectrum for the Livingston observatory. Each peak is one of the main optics (EMTX, ETMY, IMTX, IMTY) and the frequency of the mode corresponds to a different body mode shape. An narrow bandpass elliptical filter is used to isolate the features.

Measuring thermal transients requires many hours of continuous data. This is because the thermal time constants of fused silica is very small. It takes around 30 hours for the LIGO test masses to reach thermal equilibrium from a cold state. In this context, **cold** means a time when the IFO has been unlocked for longer than 2 hours. Therefore, in order to quantify the response of the LIGO test masses to heating transients, we must search for data with the following criteria:

- The IFO must have been unlocked for at least 2 hours prior to lock acquisition.
- The IFO must be in the *low noise* state. This ensures that the IFO is fully powered and aligned.
- The length of data must be an unbroken stretch longer than 35 hours.

The data used to produce the calibration is taken from LLO's $\sim$ 105hr lock, during the third observation run of Advanced LIGO (O3). This lock stretch is impressive in multiple ways. One of which is that there is uninterrupted stretch of data during 3 day/night cycles. We extend the analysis time to 140 hours to see the effects of unlocking and re-locking of the LIGO Livingston interferometer. This is important because previous investigations on thermal heating show that for the first $\sim$ 30 hours of a lock stretch, self heating effects are the dominant thermal contribution [166]. Self heating sources are known to be the main laser beam incident onto the test mass and scattered light from the ring heater. After $\sim$ 30 hours, environmental heating is the dominant thermal source to temperature flux. The two mechanisms of radiative heating are: the walls of the chamber tank to the quad suspension and test mass and conductive heating though via the top stage though the cantilever springs, the cage/chassis to the ring heater.

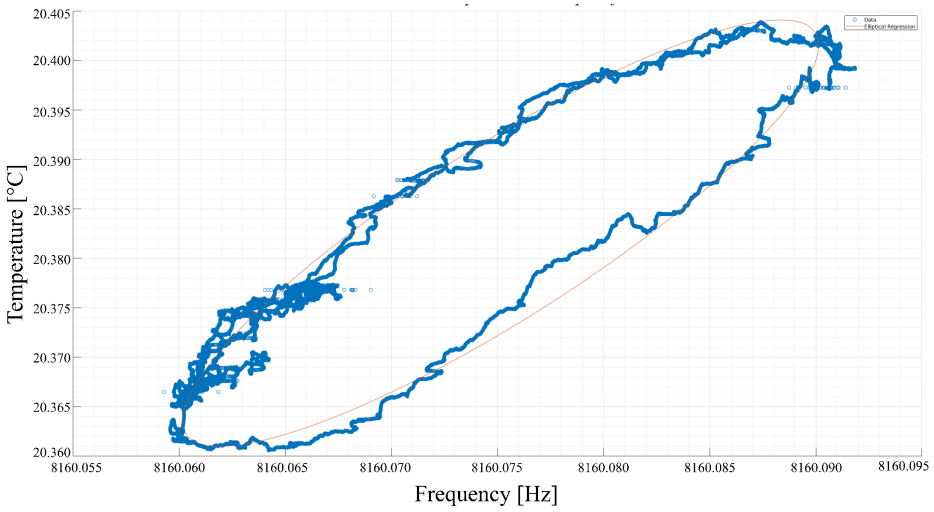

Figure 4.5: Hysteresis observed from the 8 kHz drum-head test mass body mode for LLO EMTY. This is measured using the IWAVE line tracker tool over the 110 hours of continuous lock stretch from the LLO. The red line is an elliptical regression that is applied to the IWAVE data such that the semi-major axis forms the calibration for the test mass thermometers.

For the purposes of calibration, the data after the self heating effects subside is used. We can use the ring heater thermistor as a calibration source to the eigen-mode frequency because, it is the closest calibrated sensor to the test mass. In this case, the calibration is performed for LLO ETMY. When plotting the thermistor temperature to the eigen-mode frequency, Figure 4.5 one can see an ellipse. This is a hysteresis effect induced by the weak thermal link between the ring heater thermometer and the optic. We can ignore the ring heater contribution since the ring heaters are set to a constant value throughout the observing run. In order to get a basic calibration, an elliptical regression is used to capture the phase lag. The calibration is then formed by obtaining the semi-major axis and creating a linear model.

Variable	Description	Value	Units
r_1	Radius of the X axis of the non-tilted ellipse	0.0060	Arb
r_2	Radius of the Y axis of the non-tilted ellipse	0.0256	Arb
Phi	Orientation (angle) of the ellipse (tilt)	0.5864	Radians
x_0	Centre of the X axis of the non-tilted ellipse	6.7858e3	Arb
y_0	Centre of the Y axis of the non-tilted ellipse	4.5322e3	Arb
X_0	Centre of the X axis of the tilted ellipse	8.1601e3	Hz
Y_0	Centre of the Y axis of the tilted ellipse	20.3825	DegC
SMa	Length of the Semi Major axis	0.0119	Arb
SMi	Length of the Semi Minor axis	0.0511	Arb

Table 4.1: Parameters of the elliptical fitting for ETMY. This will form the calibration parameters for the test mass thermometers.

The coefficients of the calibration have been integrated into the l1susprocpi model 4.6. Currently this takes the tracked frequencies from the IWAVE multi-line tracking and converts them into temperature in degrees centigrade (°C). The same coefficients are used across all test mass eigen-modes. Strictly, there should be a separate model for each eigen-frequency. In reality, the gradient across all optics is expected to have low variance because physically, the optics are the same (vary less than 0.1% in thickness; calculated from Evans et al. [167]) however, the offset for each model will vary more significantly across the optics. Currently, only the ETMY calibration of eigen-frequency to temperature is reliable. The uncertainty in this has yet to be calculated however it most likely to be dominated by the uncertainty of the thermistor on the ETMY ring heater. The test mass thermometers are displayed on the L1SUSPROCPI MEDM screen, underneath the optic cartoon on the far right hand side 4.6.

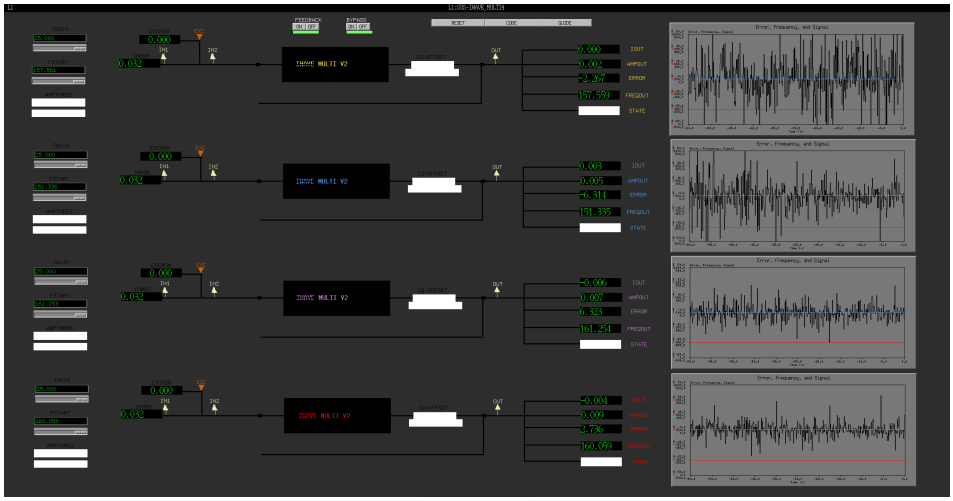

Figure 4.6: LIGO Livingston front end control screen for the four line IWAVE tacker. The upgrades to IWAVE on the LIGO front end allow for four simultaneous IWAVE line trackers to operate on a single core. Since most resonances come in packets of four (one for each optics), this upgrade can be a powerful tool for site wide simultaneous monitoring.

The pythonic front end state machine, known as guardian [99], was used to control IWAVEs' behaviour. This automation allowed robust tracking of the test mass body modes without user interference. Built into the automation were routines to handle reacquiring tracking if the IFO lost lock and resetting the line tracker

should they loose lock themselves or track the wrong frequencies. Monitoring of IWAVE error signal provides most of the information on the stability of the line trackers and the frequencies to track are known in advance therefore limits can be set to ensure IWAVE tracks correctly.

4.3 Modelling the Thermal Profile

4.3.1 Test Mass Response Model

Since we have converted the test mass body mode into units of temperature, it is possible to try and evaluate the response of test mass to an external thermal transient. This is mainly radiative heating from the vacuum chamber tank to the test mass. Another source of heat transfer could be conductive though the suspension chain and through the monolithic fibres. As discussed in Section 2.3.2, this is highly unlikely and is confirmed since we do not see the violin modes shift in frequency relative the change in ambient temperature.

Using the test mass thermometers, we evaluate the response of the LIGO test masses model. Therefore, it is possible to measure the transfer function of the test mass to a thermal injection. However thermal injection require a long time to conduct, since it involved both in terms of driving the CO_2 laser to heat the optic and allow the optic to cool sufficiently for stable lock acquisition, the multiple day-night cycle would be the closest injection feasible. Therefore, in Figure 4.7, we test the calibration of the test mass thermometers and find there is good agreement after the first 30 hours of a lock stretch. The first 30 hours shows the actual temperature rise a lot faster then the predicted model and this is the result of the test mass thermalising from lock acquisition. It is expected that the model will not fit this early region since the model was calculated during the steady state period after the thermalisation period.

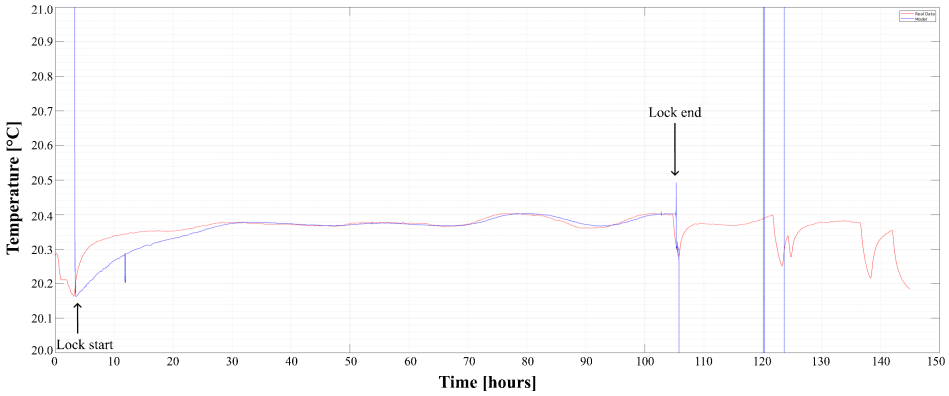

Figure 4.7: Testing the elliptical model on the ETMY optic. The red line is the real data from the temperature sensor on the ring heater. The blue line is the predicted temperature using the calibration in Figure 4.5. In the first 30 hours, we have poor agreement with the temperature sensor data however, after this time, the model agrees well with the measured temperature. The vertical blue lines are regions where IWAVE was not able to acquire (track) the eigen mode. In this case, this IWAVE line tracker has locked onto another mode. This is because the line trackers will lock onto the loudest features and it's a stochastic process which tracker locks onto a given mode.

Using the thermal model, we convert the thermal response of the test mass into a state space model. Shown in Figures **??**, we attempt to model the chamber tank contribution using poles and zeros and in doing so, we have a poor fit with the data.

Firstly, we can see that we have poor coherence between the optics and the chamber tank at frequencies above 10^{-5} Hz thus there is some suppression of thermal perturbations $> 10^{-5}$ Hz. Furthermore, whilst we can find good agreement with the magnitude of the transfer function, we have poor agreement with the phase. This is a result of poor understanding of the mechanisms that transfer the outer environmental temperature onto the test mass. Whilst radiative heating from inner wall of the vacuum tank to the test mass is the most likely path for thermal noise injection, it is difficult to construct a state space model to describe this effect.

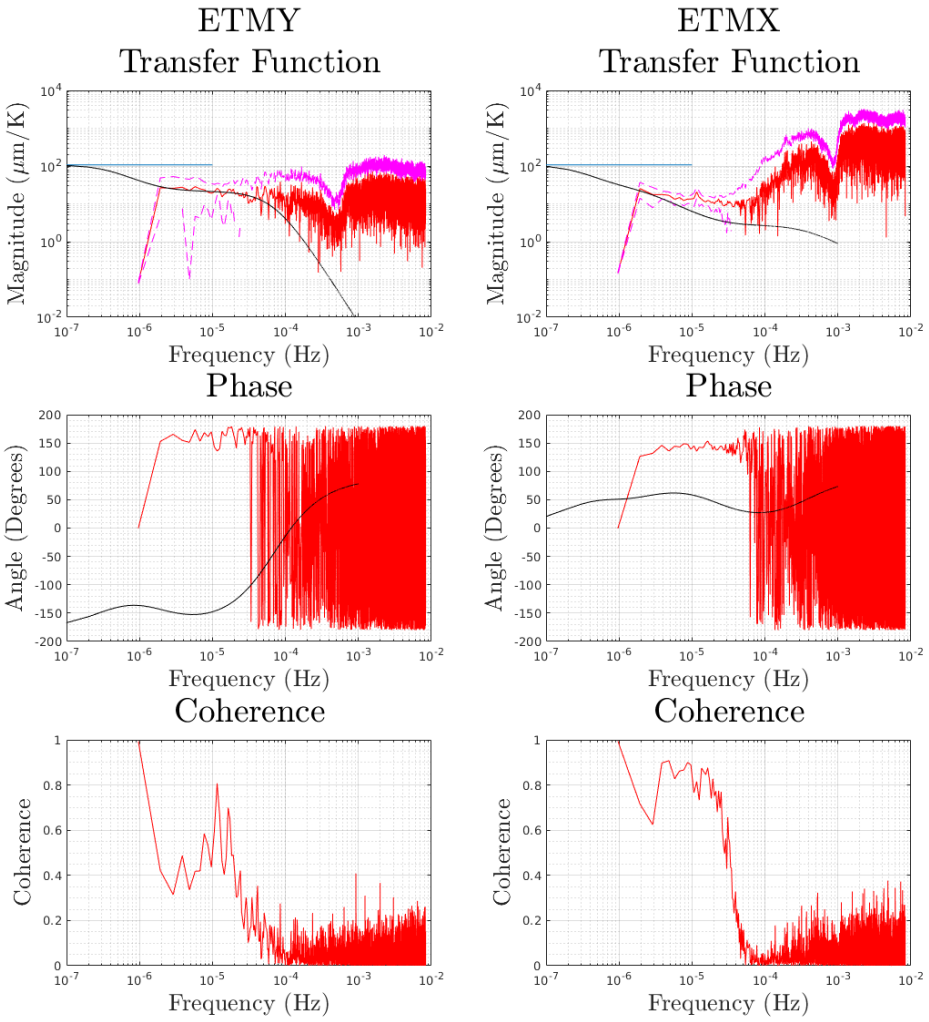

Figure 4.8: Thermal response of the LIGO end test masses (ETM) from external thermal transient. The black line is the best attempt to model the state space model using poles and zeros. The red line is the transfer function of the optic (as measured by the eigen-frequencies) to the vacuum tank temperature. The purple lines are the upper and lower bounds confidence intervals calculated by projecting the coherence onto the main transfer function.

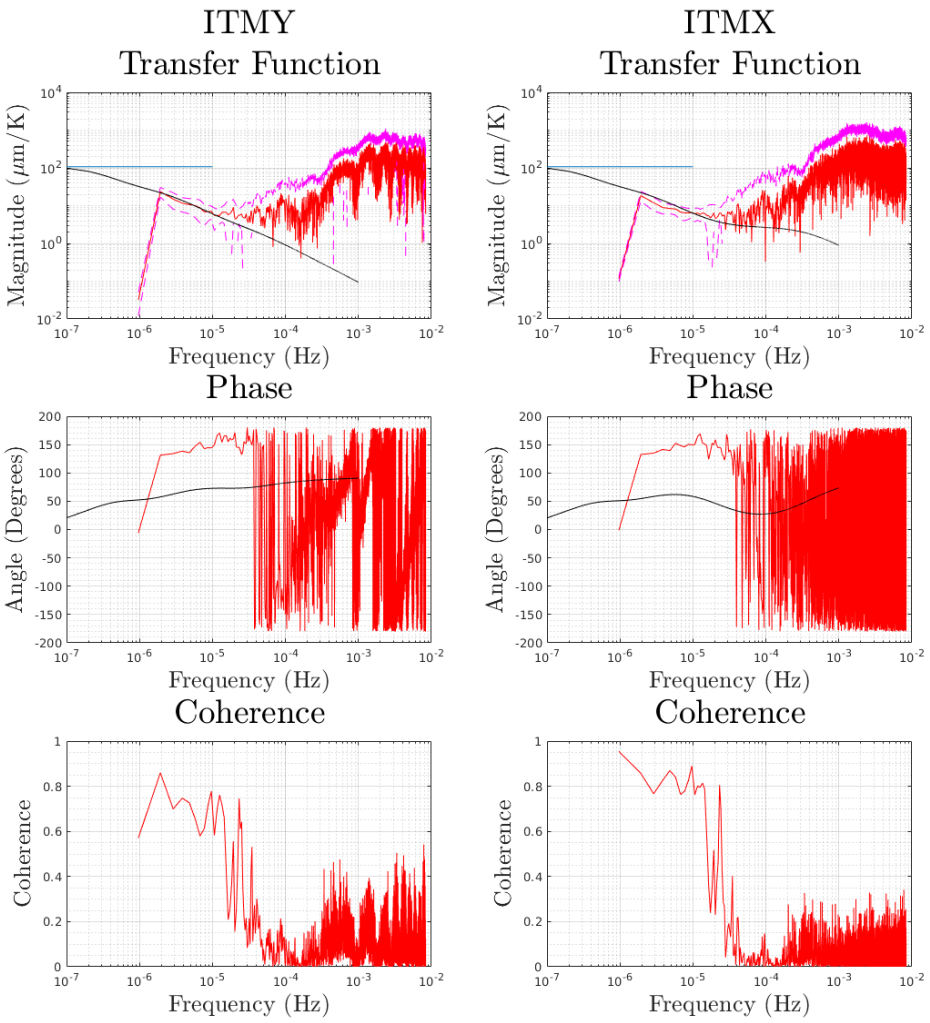

Figure 4.9: Thermal response of the LIGO inner test masses (ITM) from external thermal transient. The black line is the best attempt to model the state space model using poles and zeros. The red line is the transfer function of the optic (as measured by the eigen-frequencies) to the vacuum tank temperature. The purple lines are the upper and lower bounds confidence intervals calculated by projecting the coherence onto the main transfer function.

4.3.2 Heat Transfer Model

The test mass thermometers lay the foundation for modelling the test mass thermal profile. Extending this method to include as many of the body-mode frequencies that can be identified and tracked in the raw frame data would allow a temperature distribution over the test mass to be estimated. Not only would this be useful for understanding the real-time thermal response of the test masses, it would also allow for estimating the thermal performance of the test masses in greater accuracy. Moreover, this model will be useful for optimising the thermal performance of the IFO during the observations runs, it would allow for accurate thermal modelling for new IFO configurations - such as larger test masses, improved coatings and cryogenic IFO. The key parameters that can be extracted are the absorption of laser power, thermal lensing and temperature.

Both the LIGO and VIRGO observatories have made efforts to characterise the thermal response of the IFOs using the body mode shifts. Finite element models of the test masses are used to predict the frequencies of the body modes. The LIGO effort, outlined in Wang et al. [166], used a symmetric model of the test mass with COMSOL simulations for the predictions. Whilst the models were able to accurately predict the thermal heating and the levels of absorption, a lack of long lock stretches in LIGO second observing run limited the investigation. Furthermore, the uncertainties in the model are large since only one test mass body mode was used to derive the full optic thermal profile. In order to reduce the uncertainty, more body modes would need to be fed into the model thereby increasing the spatial resolution across the optic. This is where IWAVE will prove most useful as it can accurately measure many modes, either on the LIGO front end or offline in FRAME data. The LIGO Livingston data used in the calibration presented this section was the best unbroken lock stretch across both observatories. In order to reduce the uncertainties in the calibration, lock stretches will need to be stitched together however this will increase the systematic error in the calibration. It is hoped that in the fourth observing run and beyond, there will be significantly more unbroken long lock stretches to improve the calibration and verify the model.

4.4 Improved Tracking

Due to the finite resources of the front end, tracking of the LIGO test mass body modes was moved over to the LIGO computing grid. We discussed in the previous section that we would need to stitch together lock stretches. We can do this using the saved channel data in the LIGO FRAMES and the LIGO computing grid. Parallel jobs would be able to track multiple modes simultaneously. Moreover, with better understanding of the τ parameter of IWAVE, it is possible to automate the IWAVE parameters. The new tracking pipeline follows the following steps:

- The `gw_data_find` tool is used to create text (cache) files that contain the locations to the GWF frame files within a GPS time for a lock stretch of a 30+ hours.
- A custom C script, that is a wrapper of the *libframe* frame reader, opens the the GWF files sequentially and extracts the required channel data and stores this in binary (.bin) file.
- A MATLAB script opens the binary file and converts it into a MATLAB readable compressed (.mat) file.
- A spreadsheet containing the latest estimates of the optics body mode resonances are used to provide initial guesses for the frequency estimates. These are loaded for IWAVE to use later.

- The MATLAB IIR filters are used to pre-condition the data.
- The filtered data is passed thought the MATLAB build of IWAVE where the results are decimated then saved.

The raw date is stored at the maximum (full) LIGO sampling rate of 65536Hz. This sampling rate is necessary since the body modes are present at many orders of kHz. This large amount of data poses a computation challenge since 1 hour of 65536Hz stored in double data precision yields $\sim$ 15 GB of data. Recall that IWAVE makes internal copies of the input data therefore, four line tracker would take over 60 GB or memory to process a 1 hour segment of data. Therefore, small segments of data on the order of a few minutes are analysed and stitched back together in order to reduce memory costs. This high sampling rate is necessary since it allows higher spatial frequency resolution. There was not enough time to fully evaluate this improved tracking using the offline data FRAMEs due to time limitations however, the code pipeline has been tested in small batches and has proved to be capable of the task. Only minor improvement are required, such as handling parallel job crashes and performance optimisation, however these take a long time to rectify since the job themselves take several days to run.

4.5 Limitations

One of the key limitations is the identification of the test mas body modes. The greater the number of modes reduce the uncertainty in the parameter estimation as well as increasing the spacial resolution for the optic. Currently, COMSOL simulations predict the locations of the body modes and careful study of the LIGO ASD corroborates the prediction. In the kHz region of the IFO, forests of peaks from other resonant sources overlap with the test mass body mode making it difficult to distinguish each mode. One potential solution would be to automate a IWAVE to track the predicted modes over a long lock stretch and observe if the frequency shift co-insides with the thermal model frequency shift. This would requires a large computational resource allocation since many hours of data, sampled at a very high rate, would need to be processed parallel to all other concurrent frequency predictions.

Once test mass body modes are identified, it would be much easier to deploy IWAVE on the LIGO front end. This way, offline processing requirements can be better allocated for training and improving thermal models. However, the limitation here would be the number of IWAVE modules that can fit onto the front end DACs such that the latency of the front end is minimally affected. Tracking the modes on the front end not only takes advantage of IWAVE time-series based analysis but one can levy the front end tools such as filtering, decimation and frame writing. IWAVE has been measured to be relatively low impact to signal delay on the front end machines at LIGO thus lends itself for rapid, real-time characterisation of the test mass body mode resonances.

Another challenging tasks will be verification of the model. Since the time scale to measure thermal transients is on the order of hours, with a stable IFO, it will be difficult to obtain the commissioning time in order to perform the required injections as well as, recovery time for the IFO back to nominal conditions. With the improvements of the seismic isolation, PI dampers, violin dampers and length control, the number of long continuous lock stretches is expected to increase therefore, more data sets will be available to refine the models.

4.6 Extensions and Alternative Applications

4.6.1 Ptychography

We have seen in the previous sections that the quality of the optical surface greatly affects the ability to lock the interferometer as well as stability of the lock. Measuring the optical surface is a non-trivial pursuit since the size of the optic makes it unsuitable for most surface characterisation techniques as well as, in-situ techniques would need to meet the strict vacuum requirement of LIGO. Therefore, a surface characterisation technique that can rapidly scan the surface of the test mass and provide precise information on the surface quality either in-situ or close to final installation would be very useful.

Ptychography [168] is an optical technique coupled with an image processing technique that can characterise the surface if a target, to high precision, with imperfect lenses. The techniques uses overlapping Fresnel diffraction patterns from light reflected from a target using a monochromatic source. The laser is scanned over the target and, at each position, a image is captured with a CCD camera. Knowing the laser wavelength, distance from the target, angle of reflection and CCD properties, the image can be reconstructed of the target.

Typically, Pytchography has been demonstrated on a small scale using targets of the order of 10^{-3} m however, recent tests using large mirrors ($\sim 10^{-2}$ m) have proved fruitful. The limitations currently lies with the time to scan across large optics and optimising the analysis algorithm to handle the large amounts of data from scanning larger optics. If the speed of the technique can be improved then one immediate application in LIGO is rapid characterisation of the optical HR surfaces. This would particularly useful during installation and maintenance process of LIGO optics because the commissioners could obtain a snapshot to the condition of the optic surface, useful for avoiding potential problematic areas during beam alignment.

4.6.2 Application for Current and Future Observatories

The analysis for the O3 run has establish the foundations for a real-time estimate of the LIGO test mass thermal properties. The overall goal of thermal modelling and parameter estimation is to establish a robust method of characterising the thermal response of a GW interferometer. The implications of this new analytical pipeline could be expanded to model the thermal response of future GW observatories. This is because of the increasingly higher input and stored laser power. The consequence of increasing laser power, will result in more power being absorbed by the optics. Thus, having a robust method for monitoring and modelling will be vital in playing a part in long lock stability of current and future GW detectors. By extension, it is extremely expensive and time consuming to produce new optics for GW observatories for either room temperature or cryogenic operational temperatures. Whist mirror coating technology has improved immensely, the long term thermal performance of an optic will only be revealed under operation. Therefore, the methods presented in this chapter can provide early estimates for the expected thermal performance over an observing run - useful for thermal tuning, improving mirror coatings and commissioning.

Chapter 5

Calibration

> Glory lies in the attempt to reach one's goal and not in reaching it.
>
> Mahatma Gandhi

Chapter 4 has shown us one of the time dependent mechanisms perturbing the interferometers that affect the final output strain. Understanding such effects are important for calibrating the LIGO strain data. The calibration pipeline aims to characterise the response of the interferometer and uncertainty, thereby creating an explicit relationship between the amplitude and phase of incoming gravitational waves, by using a combination of hardware injections, systems modelling and absolute references. In this chapter, we will see how a mechanical device, called the Newtonian Calibrator (NCal), will add another source of absolute reference. In particular, we will focus on the hardware used, the installation and commissioning of such a device and the resulting, first ever, injection of the NCal signal into the LIGO Hanford detector.

5.1 Introduction to Calibration and Absolute References

Before delving into the NCal impact on calibration, first we must understand how the calibration pipeline converts the raw counts of LIGO into a calibrated dimensionless strain, $h(t)$ through the use of absolute length references. For the following sections, we will be summarising the calibration processes used during LIGO third observation run (O3).

5.1.1 Calibration Scheme in O3

The calibration pipeline aims to characterise the differential arm (DARM) displacement of the 4km LIGO arms. External stimuli, such as GWs, cause apparent length changes ΔL_{free} which is expressed are DARM as:

$$\Delta L_{\text{free}} = \Delta L_x - \Delta L_y \equiv hL \tag{5.1}$$

Where ΔL_x and ΔL_y are changes in the lengths of the X and Y arms and, h is the dimensionless strain recovered from the detector. The quadrupole suspension and the mirror actuators, housed on the reaction chain, work in tandem to suppress the free motion ΔL_{free} of the test masses. This global length control, with open loop gain G, hold the arm cavities in resonance. Residual motion outside of this control loop is known as the residual differential arm length ΔL_{res}. The

digital error signal $d_{\rm err}$ is formed by converting $\Delta L_{\rm res}$ using the sensing function $C(f)$. Additional digital filters, D, convert d_{err} into the digital control signal $d_{\rm ctrl}$. The actuation function, A, further converts $d_{\rm ctrl}$ into the control displacement, $\Delta L_{\rm ctrl}$, that suppresses the motion of $\Delta L_{\rm free}$. From this, it is possible to deduce a conceptual calibration model (Figure 5.1):

$$\Delta L_{\rm free} \equiv \Delta L_{\rm res} + \Delta L_{\rm ctrl} = \frac{1}{C^{\rm model}} d_{\rm err} + A^{\rm model} d_{\rm ctrl} \tag{5.2}$$

thereby the response function, $R^{\rm model}$, can be defined as:

$$R^{model} = \frac{1 + A^{\rm model} D C^{\rm model}}{C^{\rm model}} = \frac{1 + G^{\rm model}}{C^{\rm model}} \tag{5.3}$$

where $G^{\rm model} \equiv A^{\rm model} D C^{\rm model}$ is the DARM open loop gain therefore, the dimensionless strain, h, is given by:

$$h = \frac{R^{\rm model} d_{\rm err}}{L} \tag{5.4}$$

Characterising the IFO for calibration involves two main functions. These are the sensing function $C(f)$ and the actuation function $A(f)$:

$$C^{(\rm model)}(f) = \left(\frac{H_C}{1 + i f f_{cc}^{-1}} \right) \left(\frac{f^2}{f^2 + f_s^2 - i f f_s Q^{-1}} \right) C_R(f) \exp(-2\pi i f \tau_C) \tag{5.5}$$

$$\begin{aligned} A^{(\rm model)}(f) = {} & F_U(f) H_U A_U(f) exp(2\pi i f \tau U) \\ & + F_P(f) H_P A_P(f) exp(2\pi i f \tau P) \\ & + F_T(f) H_T A_T(f) exp(2\pi i f \tau T) \end{aligned} \tag{5.6}$$

There are three distinct calibration data products: a real-time (online) calibration; a low-latency ($\sim$ 10 seconds) and a high latency ($\sim$ 6 months) calibration. The online calibration uses the raw real-time interferometer output in addition to infinite impulse response (IIR) models of the interferometer actuation (A) and sensing (C) response to form a crude estimate of h. Whilst not useful for GW source searches - due to the IIR filters having appreciably high systematic error and uncertainty unsuitable for search analysis - this calibration reliably informs commissioners and operators the condition of the interferometer. The low-latency calibration uses the same raw real-time interferometer response however, moderate fidelity finite impulse response filters (FIR) of A and C are used. This calibration pipeline delivers the C00 calibrated science frames used for initial event detection and subsequent follow-up investigation.

$$\eta_R = \frac{R_{\rm ref}}{R_{\rm model}}. \tag{5.7}$$

The high latency pipeline delivers the C0N calibrated science frames, where N is the release number. This version of the calibration recovers the raw detector output, stored in frames, and uses the highest fidelity models of the actuation and sensing functions calculated from first principles. Furthermore, systematic uncertainties, omitted during the low-latency calibration, are included in the high-latency calibration. The omission of certain features are the result of later improvements in the understanding of the interferometer, changes in the actuation strength within the pendulum chain and correcting for mistakes in the low-latency calibration. This usually takes some number of months to produce. Therefore, the high latency is useful for better constraining the Parameter Estimation (PE)

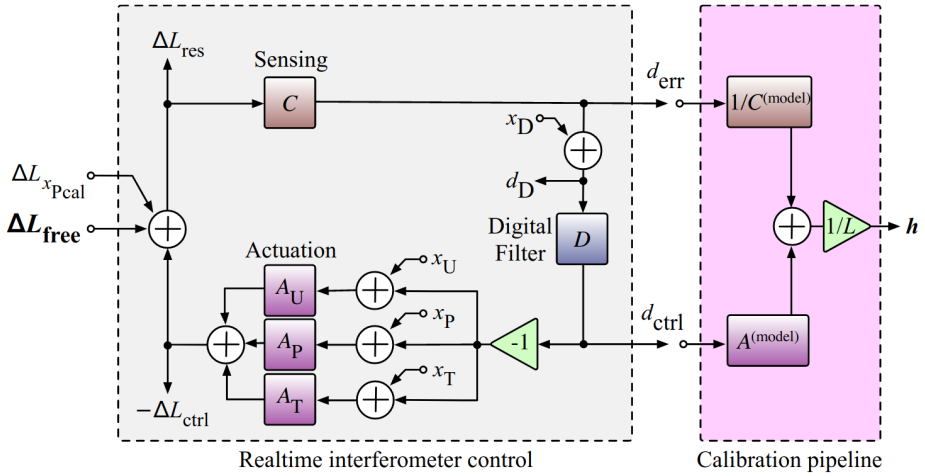

Figure 5.1: A basic schematic of the basic interaction of the length control for the DARM feedback loop for AdvLIGO (left) and the calibration pipeline (right). The length control is a sum of the Upper Intermediate mass (U), Penultimate mass (P) and Test mass (T) stages of the LIGO suspension which informs the actuation function ($A_{\mathrm{model(f)}}$) (Equation 5.6). Through the loop, the PCal can inject waveforms to induce length changes via radiation pressure, represented here by $\Delta L_{x_{Pcal}}$. The sensing function converts the residual DARM motion (ΔL_{res}) into a digital control error signal (err). The pink box produces the calibrated strain and this process can be interpreted as either unmodelled noise or the graviational wave signal after all known contributions have been removed from the data. The DARM loop suppression can be obtained by measuring $d_D = d_{err} + x_D$. Reproduced from [2].

of successful GW events. Moreover, high computation search pipelines that require long stretches of data - such as those looking for CWs, long duration bursts, stochastic events IMBHs and extreme BBH or NSBH candidates - prefer using the cleanest data before executing search analysis since these pipelines have a high computational cost.

In O1 and O2 versions of calibration pipeline, the upper-intermediate and penultimate stages of the main quadruple suspension chain were combined. In addition to the characteristic response (delay) time of the last three stages were combined into a single time parameter. O3 saw the introduction of each stage of the quadruple pendulum having their own eigenvalue. Furthermore, O3 saw the rigorous improvement and implementation of ***pyDARM***, the dedicated calibration pipeline used for calibration modelling, analysis and parameter estimation. It is important to note, pyDARM is not part of the LIGO front-end but is used separately on local machines for interrogating data to better understand the systematic uncertainty in the calibration.

The uncertainty in the calibration of LIGO is reported as the upper and lower 68% confidence interval on the systematic uncertainty in the most sensitive frequency band 20-2000 Hz.

Obs Run	Magnitude	Phase
O1 & O2	$\lesssim 5\%$	$\lesssim 7$ degrees
O3a	$\lesssim 2\%$	$\lesssim 2$ degrees
O3b	$\lesssim 2\%$	$\lesssim 4$ degrees

Table 5.1: The uncertainty of the calibration since the first observation run over the most sensitive region 20-2000 Hz.

5.1.2 The Photon Calibrators

5.1.3 PCal Overview

The Photon Calibrator (PCal) is the main source of absolute length reference used in the calibration pipeline. The PCal uses sinusoidal modulated laser power that displaces the LIGO optic by a fiducial amount through photon pressure. An integrating sphere, based on a power sensor that is surrounded by a spherical enclosure that minimises reflections of the incoming beam and maximises the incoming power to be scattered into the sensor, was used to measure the PCal power that was reflected from the LIGO optic. This was a NIST traceable power metre that was designed to measure the laser power to sub-percent levels of precision and accuracy. The PCal laser deliverers a power stabilised beam that is divided equally before being steered onto the LIGO optic. The two beams are referred to as the inner and outer beams. The PCal system directly informs all of the time dependent correction factors, denoted with κ's. One example is κ_C which is one of calibration real-time time dependent correction factors used as a probe for the optical gain.

The PCal system is not exclusively used for calibration. The PCal can inject a multitude of signals into the IFO including custom waveforms. Thus, the PCal system is used to inject GW waveforms into the IFO as part of the GW pipeline characterisation.

The optimal location of the PCal beams on the ETMs was calculated through FEA simulations. Furthermore, the drive location was chosen to minimise the excitation of the test mass drumhead mode. The sinusoidal PCal-induced displacements are required to be accurate within 5% in amplitude and 16 μs in timing over 2σ confidence intervals [169]. The displacement x_{pcal} [m] of the ETMs as a result of a PCal injection can be expressed in the form given in Berliner et al. [169]:

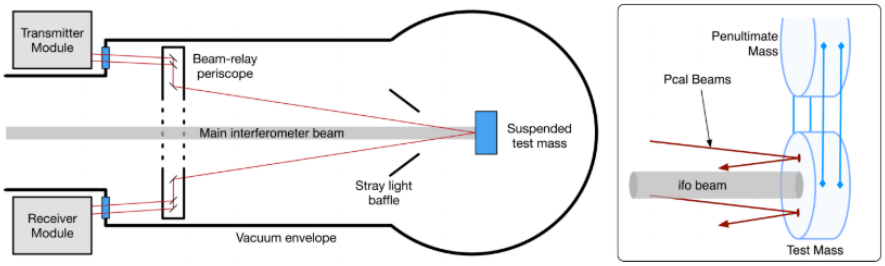

Figure 5.2: Schematic of the optical injection of the PCal laser in interferometer GW observatories with a top down perspective (left) and an isometric close up at the test mass (right). Light is generated in the transmitter module and is split into two beams - in air - then being sent into the vacuum envelope via a window. The beam-relay periscope directs the beams into the test mass. The beams reflect off the test mass towards the opposite side of the vacuum envelope and steered by the beam-relay periscope towards the receiver module. Here the beams are combined and measured with the power sensor. Credit: [10].

$$x_{\mathrm{pcal}} = -\frac{2p_0}{c}\frac{1}{M\omega^2}\left(\cos\left(\theta\right)\right) \tag{5.8}$$

Where: p_0 is the amplitude of the periodic laser power modulation; c [ms^{-1}] the speed of light in a vacuum; M [kg] the mass of the test mass optic; ω [Hz] the angular frequency of the amplitude modulation and, $\cos(\theta)$ the cosine of the angle of incidence between the PCal and the optic. The negative sign denotes a π phase difference between the amplitude of modulation and the driving force.

5.1.4 PCal Alignment Drifts

The stability of the alignment of the PCal was one concern over the O3 run. Drifts in the PCal spot position on the LIGO optic would have two detrimental effects. One is that the control signals will need to be increase to compensate for the induced torque therefore increasing noise in the h(t). Secondly, this would increase the uncertainty on the PCal calibration because the initial PCal calibration was set to a particular spot position on the optic and deviations away from these spot positions would induce uncertainty in the recovered power from the PCal laser. In extreme circumstances, the PCal beam would clip the integrating sphere. This would lead to mis-calibration however these effects are accounted for in the error budget.

One method used to capture the alignment of PCal laser spot in case of laser failures, was to use kinematic mounts with mirrors installed in them to reflect the PCal back into the iris. This was installed on the transmission side (TX) side of the PCal at LIGO Livingston at the EY end. The exact positioning of the new optics were discussed over several weekly calibration meetings. It was decided to use kinematic mounts over flip mounts

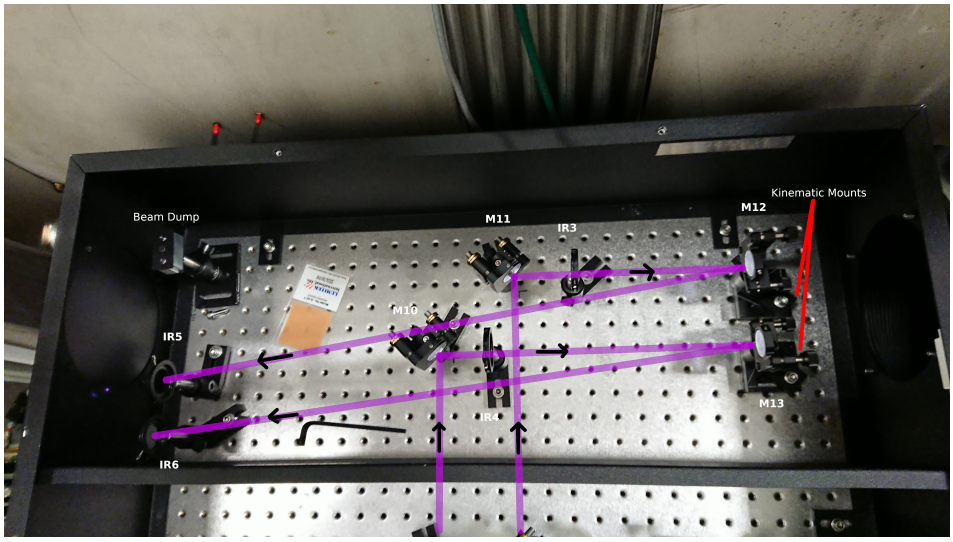

Figure 5.3: Top end of the PCal Transmission (TX) Box at LLO at the EY end. The purple line shows the beam path when the kinematic mounts are installed. The mirror and iris labelling conventions is a continuation of the established labelling notation in the PCal Optical Layout [11].

Before stating the installation of the iris and mirrors, a reference photo was taken of the alignment before starting the work and this is given in LIGO document G1901075 (from pages 2-4). This was done by opening up the RX side and photographing the beam position with both beams, blocking the outer beam with the beam dump and blocking the inner beam. The mounts and posts with the mirrors are assembled onto kinematic mounts. The lower base of the kinematic mount for M12 is bolted into place on the inner beam path then IR3 is bolted in place on the inner beam path. The iris IR3 alignment is checked using a beam viewer such that when the iris is at its' smallest aperture, the beam is centred through the aperture. Mirror M12 is installed on the top part of the kinematic mount then lowered onto the lower half that is bolted onto the breadboard. The height of M12 is adjusted and using an IR card and the beam retro-reflected back, between M11 and M10. Iris IR5 is bolted in and aligned using the beam viewer as well as the aperture of the iris set to the smallest aperture. We checked that the alignment is unaffected by the use of the kinematic mount by removing the top part of the kinematic mount (attached to the mirror) and replacing it. The alignment is checked with the beam-viewer and it appears that the alignment is unaffected. The installation process was repeated for the outer beam.

Another method of understanding the PCal stability was to use a CCD camera on the receiver side (RX). The final steering mirrors were used as the pick off point. The camera was set up on an additional channel in the LIGO data stream.

(a) Front view of the PCAL with the integrating sphere and the CCD camera.

(b) Additional mirror placed behind the PCAL steering mirror on the RX side.

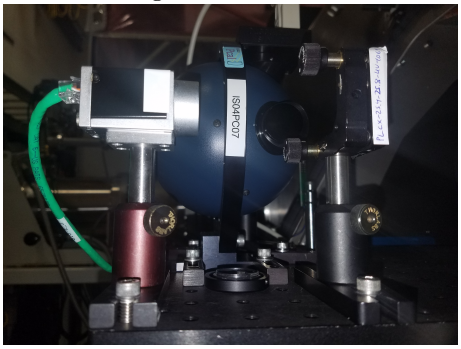

(c) Side view showing the CCD camera next to the integrating sphere.

Figure 5.4: LLO PCAL EY with the CCD camera installed using residual light from behind the steering mirrors.

The iris were a useful tool during the weekly PCal maintenance to see if the PCal alignment had drifted significantly. When the kinematic mounts were placed into position, a beam card was used to trace the beam path to the iris and inspect the beam spot in the iris. The beam would be nominally centred within the iris and the iris would be closed such the aperture was the same size as the beam spot. Using a beam camera, when looking at the iris, if there were bright spots clipping the iris aperture, it was possible to see the how much the beam had drifted over the week. The worse case scenario would be that the beam spot would be fully out of the iris aperture therefore, it would result in having to adjust the steering mirrors to re-align the PCal though, this was never observed.

It is unclear how effective the camera was able to measure the alignment drift. Whilst it was integrated into the LIGO software infrastructure, the camera was not utilised for measuring alignment drifts. This is mainly due to a lack of person power to dedicate the time to fully characterise the system.

5.1.5 PCal Injections for Calibration

At each GW observatory, a working standard is used to calibrate the power sensors used in the PCal scheme. During the weekly maintenance of the power sensors, the working standard is used to characterise the two PCal beams at both the transmitted (TX) and receiving (RX) side of the PCal laser. An additional integrating sphere, is used in-place of the power sensor used during the run. A full procedure is documented in T1500062.

Furthermore, weekly injections with the PCal system, known as PCal sweeps, were used to characterise the IFO response function. These are injected using

the DTT software tool whereby a discrete frequency and amplitude are injected periodically over the sensitive range of the IFO, 20-2000 Hz. The amplitudes of each injections were tuned to achieve a SNR > 8. The SNR chosen is to maximise the coherence between the injection and the output photo-detector of the IFO whilst minimising injection run time. The amplitude of the injection cannot be set too high as this will saturate the electronic drive of the PCal laser, in other words going beyond the range of the optical fillover servo, thereby injecting a comb of lines into the IFO. Whilst this does not impact the measurement of the response function of the IFO, the saturated drive could reduce the lifetime of the PCal electronics and introduce instabilities in the IFO. Such instabilities could be exciting undesirable resonances, such as violin modes, test mass body modes or suspension resonances. Furthermore, due to the stricter requirement that mandated that the IFO should minimise non-observation time, the PCal calibration injections were shortened. This was done by reducing the number of points the PCal injected across the sensitivity band - from 30 to 18 points. Furthermore, the injections at the tails of the IFO sensitivity band were reduced. At low frequency, $< 20\,\mathrm{Hz}$, the many overlapping control signals, filters and suspension resonances make this regions unsuitable for search analysis. Similarly, at high frequencies, $>$ 2kHz, the spectrum is contaminated with forests of peaks from multiple instrumental noise sources.

During O3, an automated system was integrated into the LIGO guardian system at LIGO Livingston. The settings for the PCal sweeps remain constant therefore, it was more efficient to allow the automated system handle the injections. In addition, the automated system also handled configuring the IFO to be ready for the injections, restoring IFO setting required for science observation to resume and data extraction of the injections ready for ingestion by the calibration pipeline. There were additional benefits to the automation of the injections. The first is that it removed the single point failure of the dedicated calibration member having to be present to run the injections. Secondly, it reduced the down-time associated with running the injections thereby allowing time to prototype new injections or returning to observational mode. Thirdly, the reliability of automation reduced erroneous injections as well as reducing the time to process the injections and update the IFO calibration parameters. The main downside of the automated system was that it was not possible to observe the real-time transfer function during the injections. One would want to watch these in order confirm that the measurements were reasonable and no irregularities were occurring during the injections. This is mitigated by the injection templates, used to inform the PCal how to drive signals into the IFO, were fully tested previously during engineering runs and during maintenance periods therefore there should not be any abnormal behaviour. Any such abnormalities will be caught by the various real-time monitoring systems, built into the injection automation and the wider IFO monitoring systems, and the injections will cease and the IFO restored to observation ready mode.

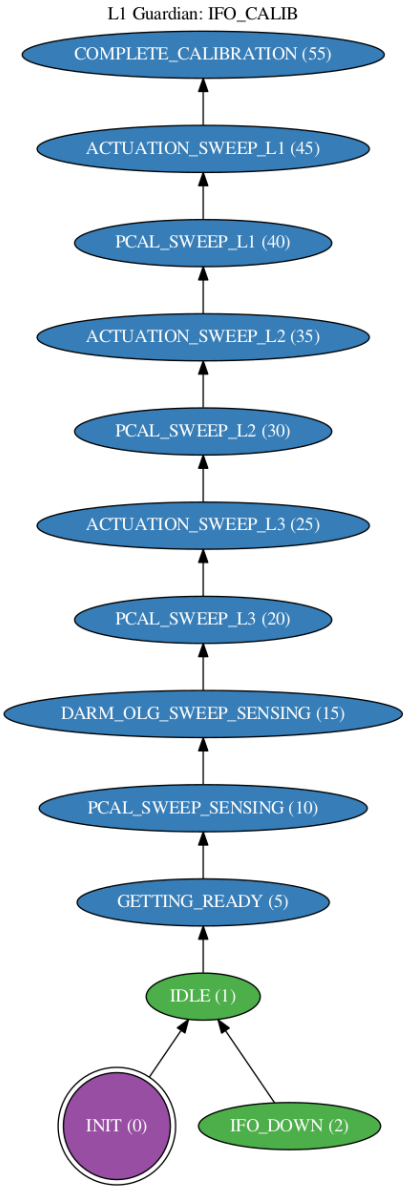

(a) Graphical states of calibration automation.

(b) Main control guardian screen.

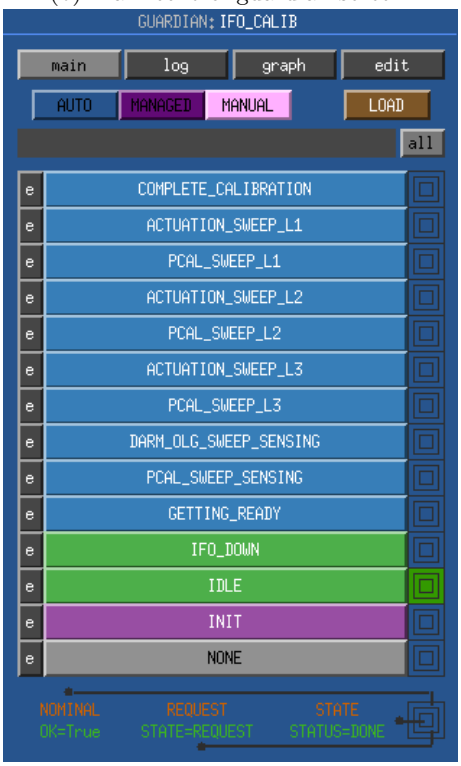

(c) Selectable states for calibration.

Figure 5.5: LLO calibration automation implemented using GUARDIAN.(a) A graphical representation of path of states

Moreover, persistent frequencies are injected into the IFO through the science run of the observatory. These aid in monitoring the status of the IFO and used in computing the real-time time dependent correction factors. These are controlled by a separate automated system, also integrated into the guardian system. These injections are closely spaced together at < 20Hz and at a few hundred Hz and a around 1100 Hz. Since the injections are sine waves, it is simple to filter them out later in the cleaned calibration data product.

The careful characterisation, maintenance and injection campaigns of the PCal has resulted in the O3 PCal system having an overall uncertainty $< 1\%$. This impressive feat of precision measurement with the PCal results in an overall cal-

ibration that is not limited by the PCal system. Nevertheless, there are many areas to improve the PCal system further. As mentioned in previous sections, the alignment is also one of the largest sources of uncertainty as it is difficult to precisely know where the spots are on the test mass. Moreover, improve the stability of the laser, as well as, the increasing the drive stability and capabilities will allow greater flexibility for the PCal system.

5.1.6 Alternative Absolute Calibration References

The aforementioned PCal system is the primary source of absolute calibration reference that has been established since S6 of LIGO. Other calibration absolute references have been explored. During O1, three methods were explored: ALS Diff, Free Swinging Michaelson (FSM) and the PCal. While the PCal remains the most favourable method for calibration, the ALS Diff and FSM methods remain useful for verification of the PCal calibration. During O3, the ALS Diff and FSM methods were revived however, insufficient time resulted in only a limited range of the LIGO bandwidth being treated with all three methods was available for comparisons.

5.2 The Newtonian Calibrator

5.2.0.1 Motivation

The Newtonian Calibrator (NCal) is the latest R&D effort for another absolute calibration reference. The simplicity of the NCal is the main key advantage for consideration. This is because, the geometry has been designed for cost effective manufacturing whilst maintaining high machining tolerances as well as easy access to the most critical parts - useful for maintenance. More importantly, the basic morphology of the hardware greatly simplifies the modelling calculations in order to predict the force the NCal will exert on the LIGO test mass thereby reducing computational load and systematic error.

The basic geometry of an NCal device uses a constellation of rotating masses configured to exert gravitational forces on a test mass (or sensor). The exact arrangement of masses will yield an outer hexapole and inner quadruple moment on the test mass. Furthermore, the force exerted on the test object will fall off according to the Newtonian inverse square law.

The use of an NCal style device has seen adoption in a multitude of detectors, not exclusively for gravitational-wave detection. Applications such as calibration of gravitational gradiometers [170] and measuring the universal Gravitational constant, G.

Whilst the Virgo and KAGRA gravitational-wave observatories have such a system integrated into their calibration for dimensionless strain [119, 171–173], the LIGO system is purely a pathfinder project. The NCal was not part of the AdvLIGO design consequently, there is not a dedicated mounting location for the device. In the following section, we will explore the installation, commissioning and initial first tests of the LIGO NCal system.

5.2.1 Installation

The optimal location for the NCal was the closest, in air, location to the test mass. To that end, the most suitable location was the BSC pier, the supports that hold the vacuum chamber. The BSC pier has four posts that would allow the NCal to be mounted upon. Despite the tight packaging constraints, shown in Figure (5.7), there was sufficient clearance to have the NCal rotor at the same horizontal plane as the LIGO optic.

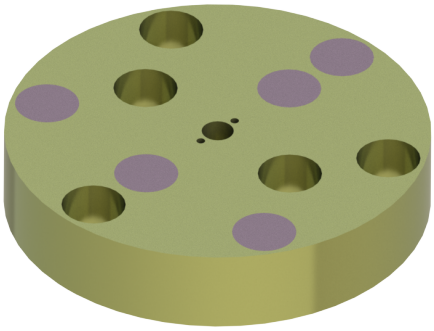

(a) CAD NCal rotor render

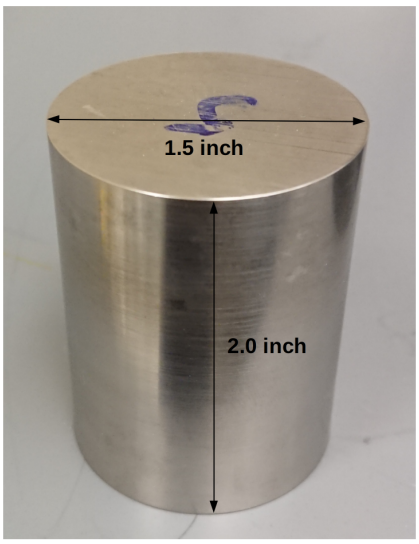

(b) One of the tungsten masses used in the NCal rotor.

Figure 5.6: (a) A CAD rendering of the NCal rotor with the tungsten mass configuration. The colour is purely for dissociating the two materials where the gold represents the Aluminium rotor and, the purple is the tungsten masses.

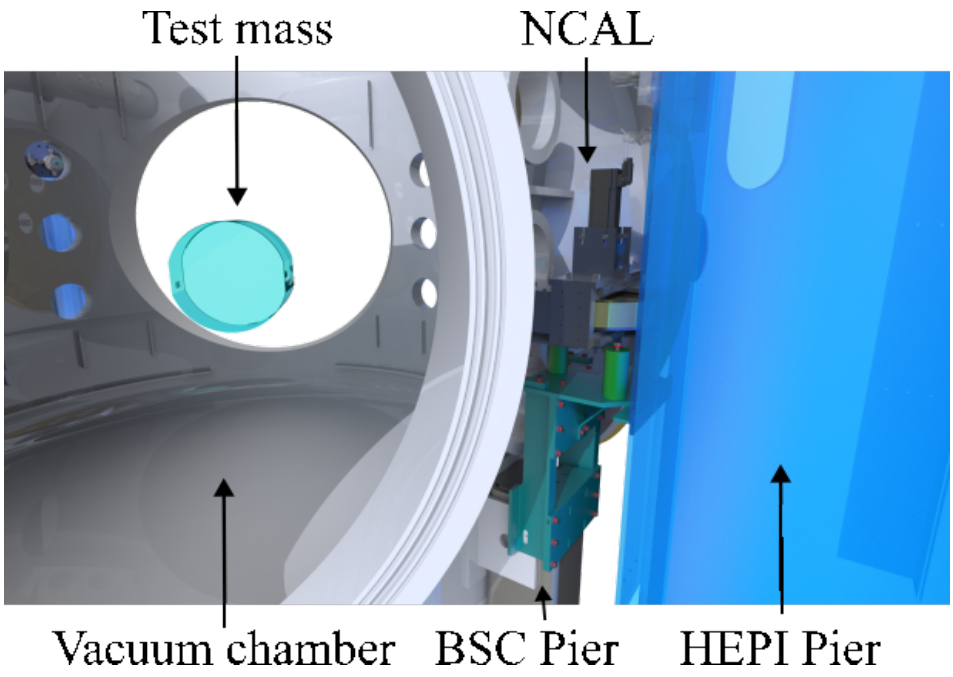

Figure 5.7: CAD rendering of the location of the H1 NCal Prototype in its proposed location. The NCAL assembly is located between the HEPI leg (blue) and the vacuum chamber (grey). The test mass (turquoise) is shown with the full quadruple suspension suppressed. A slice has been cut out of the NCAL housing to show the internal NCal rotor with respect to the ETMX optic.

The NCal was installed atop a custom mount structure and this assembly was bolted to the BSC pier. The mount structure is mainly constructed from aluminium, apart from a strengthening bracket which is made of steel. Slots on the side rail and front plate allowed the mount structure to be translated vertically thereby allowing for height adjustability such that the NCal (rotor) can be located as close to the same horizontal plane as the test mass centre of mass (COM). Although the z degree of freedom had the least impact on the NCAL force injection, it was important to align the NCal as close to the same plane as the test mass in order to reduce the uncertainties in the force modelling. A systems level simulation was used verify the integrity of the NCal mount structure. It also identified resonant modes that may arise during NCal operation. This was not experimentally verified however due to time constraints. B&K hammering would be used to experimentally determine the internal resonant modes by tapping the structure with a hammer and measuring the acoustic modes with a transducer sensor [174]. This is a common method utilised in LIGO for varying resonant modes of components.

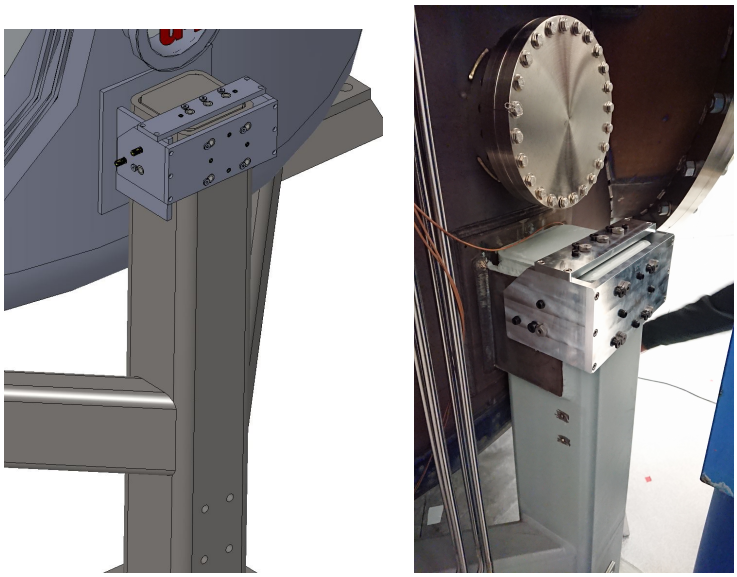

(a) CAD render of the drill fixture as it should be mounted on the BSC pier.

(b) The drill fixture being used to drill the NCal holes on the BSC pier.

Figure 5.8: CAD render and the actual drill fixture for locating the precise location for drilling the holes for mounting the NCal on the BSC pier.

The BSC pier was drilled and tapped, in a pre-determined bolt pattern, in order to constrain all the degrees of freedom. A custom drill fixture (jig), Figure 5.8, was used to precisely locate and drill the holes on the BSC pier. The bespoke tool was constructed of aluminium with precise holes to accommodate drill bushings and set screws. These would ensure the holes was drilled as tangentially as possible. For fine tuning, set screws were implemented into the drill fixture to allow for fine tuning of the positioning of the drill fixture on the BSC pier.

5.2.2 Hardware and Commissioning

The NCal arrived at LHO on the 1st September 2019, delivered from The University of Washington by Krishna Venkateswara [175]. The unit consists of a spinning aluminium rotor with precise cylindrical holes machined to accommodate Tung-

sten slugs, whose geometry precisely fits the machined holes in the aluminium rotor via interference (friction) fit. Surrounding the disc is 3/8" inch thick aluminium covers. These covers attach to 1" thick aluminium chassis. The NCal is driven with a syncro-servo motor from a commercial supplier (Beckhoff). The rotor has been drilled in a configuration to allow a quadrupole and hexapole distribution of masses such that the signals generated will appear two frequencies at twice and three times the spin velocity of the NCal drive.

At this stage, the rotor did not have the tungsten masses inserted within it. A method was demonstrated whereby a ring heater was placed over a designated rotor hole. Using a dial power supply, the ring heater was brought up to $\sim$ 60°C. With a laser spot digital thermometer, the walls of the given rotor hole was monitored until it had reached a thermal equilibrium. At this point, the a dedicated tungsten mass was test fit inside the rotor. If there was any resistance, more time was allowed to allow for the hole to thermally expand. In the cases where sufficient time had passed and the tungsten mass would not fit into the hole, the power was incrementally increased to the ring heater until the temperature has increased by $\sim$ 20°C.

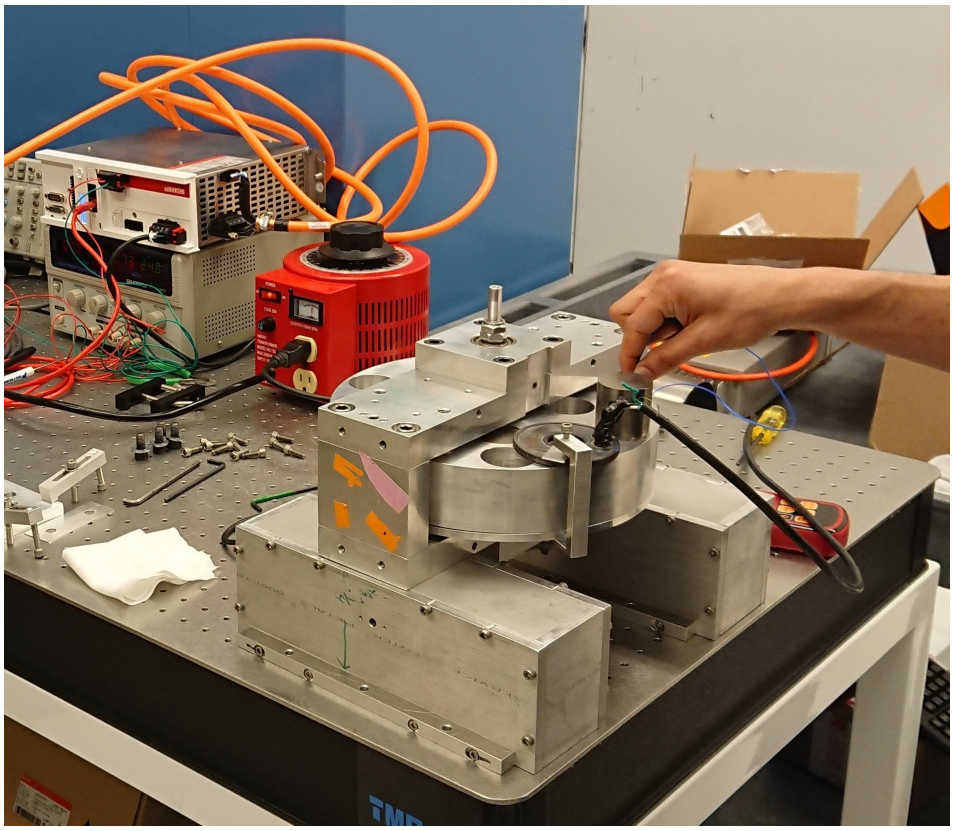

Figure 5.9: Krishna Venkateswara (right) demonstrating the use of the ring heater to inset the NCal tungsten masses into the NCal rotor.

This method was found to be slow and cumbersome. One of the flaws of this method was that the ring heater could not be placed directly over the hole of the rotor ergo, the walls of the hole expanded at different rates. This meant it took a long time for the walls to reach thermally equilibrium before test fitting the tungsten mass. In addition, to finding a suitable place to clamp the ring heater. This became particularly apparent when trying to find a ring heater location to heat the inner 2f holes as the clamp did not have enough clearance to hold the ring

heater at the required 2f hole. Furthermore, the edges of the tungsten cylinders were not bevelled therefore, if one did not precisely align the tungsten mass with the hole (ie, drop the mass in the hole at a slight angle), the tungsten mass sharp edges would scratch the walls of the holes and in some cases, would disfigure the hole preventing the tungsten mass to smoothly fit. Moreover, if there were contaminants (such as metal filing left over from machining) on the tungsten cylinder or in the rotor hole, similar fitments issues arose. It was demonstrated that lightly tapping the mass with a soft hammer would overcome this issue however, after removing the tungsten masses that required tapping, the walls of the rotor and the tungsten masses showed signs of damage that required reworking the affected areas. This raised concern because the rotor hole and the tungsten cylinder were precisely machined to fit therefore, any rework may cause a detrimental fitment issue whereby the tungsten mass would no longer be securely held by the rotor via an interference fit.

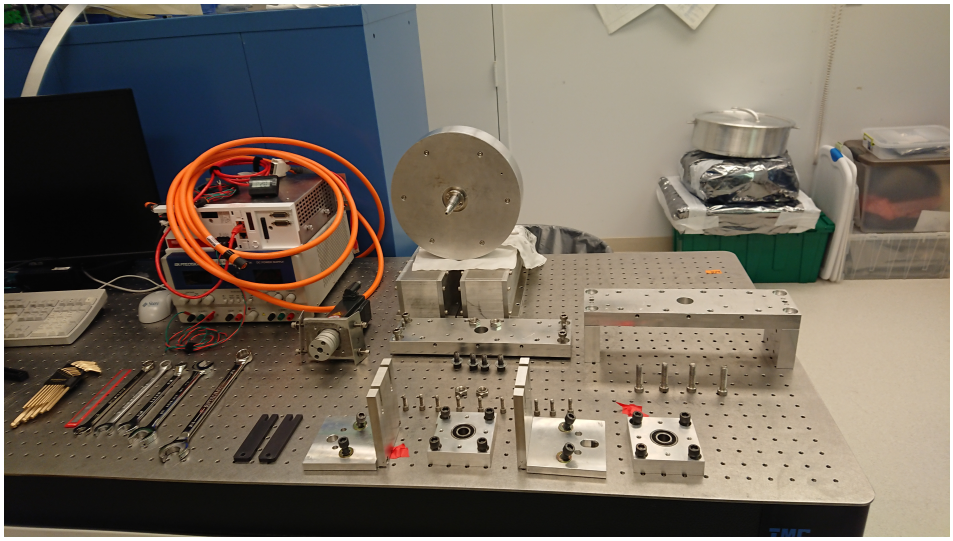

Figure 5.10: NCal after clean and bake, ready for final assembly.

An improved method of inserting the tungsten masses into the rotor was implemented whereby the rotor was baked in an oven, set to 60°C. The rotor remained in the oven for 60 minutes and the masses were carefully lowered into the holes. This was substantially easier to insert the tungsten mass without damaging the walls of the aluminium rotor. Once the tungsten masses were inserted, the rotor was removed from the oven and left to cool in at standard room temperature and pressure (SRTP).

A rotary encoder, shown in Figure 5.11c, is attached to the NCal that will measure the spin velocity of the NCal independently of the Beckhoff internal readback. A proposed plan was to use the encoder data stream, in a feedback loop, to control the NCal more precisely. One of the limitations of the Beckhoff system, that is LIGO specific, is that the Beckhoff channels are capped at the slow sampling rate of 16 Hz thereby loosing a lot of information about the drive. Using the encoder, it is possible to extract the phase of the NCal rotation, useful for torque estimates on the test masses. This is only possible with the encoder since, the encoder signal is a sawtooth signal. Inside the encoder, a calibrated internal disc is measured by an optical sensor that has a unique signature that corresponds to the angle of rotation. Therefore, the readout from the optical encoder is a repetitive ramp from 0 to 360 degrees for one cycle, hence the sawtooth signal output. A custom electronics encoder readout box interprets the signal and this forms the sawtooth

waveform since the phase readout will drop to zero after one full revolution.

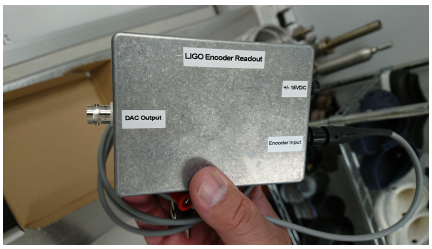

(a) Rotary encoder readout box that contain the analogue electronics to convert the encoder pulses into voltage.

(b) Sawtooth signal from the rotary encoder readout box measured on a spectrum analyser.

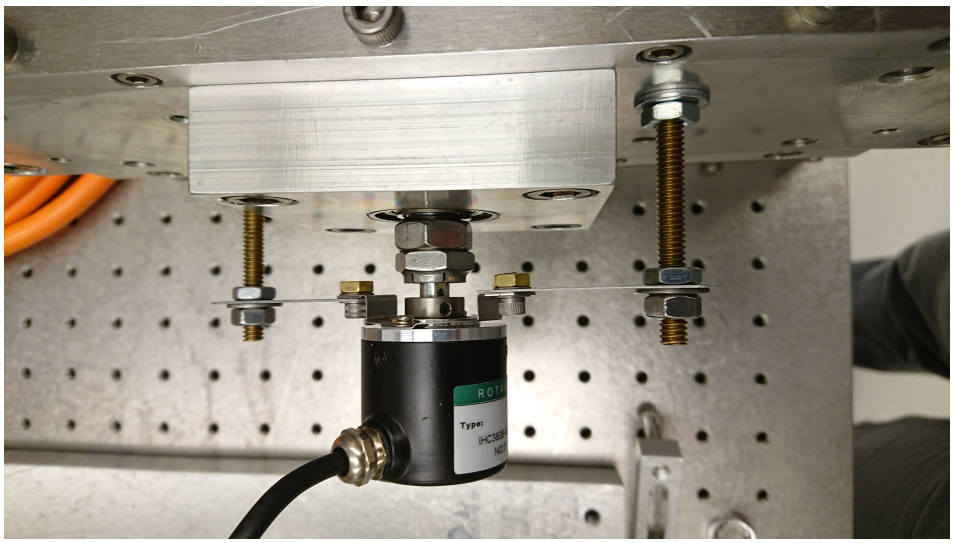

(c) Rotary encoder attached at the underside of the NCal.

Figure 5.11: used to measure the NCal spin velocity independently of the Beckhoff readback. The shaft that the motor connects to also protrudes underneath he unit, where the encoder is attached.

In addition, before final installation at the EX VEA, a full strip down and reassembly of the unit was undertaken. This accomplished two main objectives. One was to clean and bake the the individual components ensuring that no contaminants enter the end station. Additionally, this process allowed for minor re-works to some parts as well as improve the safety of the device. Namely, this required the use of thread-locking and torquing all the bolts to LIGO specification. Moreover, it allowed for precise measurements of the device using micrometres, dial indicators and height gauges. Unfortunately, it was not possible to carefully weigh the masses due to the unavailability of a precise scale. Therefore, it was only possible

to verify the masses to the gram level. As will be seen in further sections, the mass is a key parameter and the precise measurement of the mass will allow for the NCal to deliver a calibration with small uncertainty.

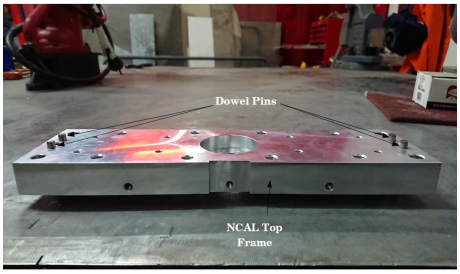

(a) Reworking of the alignment pins.

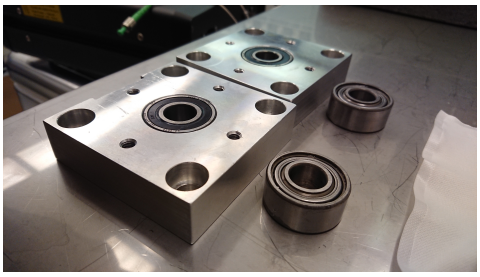

(b) Reworking of bearings.

Figure 5.12: Examples of parts that required reworking. (a) The alignment dowels used to ensure the NCal chassis is accurately assembled. (b) Replacing the bearings that allow the main shaft to rotate freely.

The NCal was integrated into the LIGO digital network, Figure 5.14 and, through EPICS via the use of a custom MEDM screen (Figure 5.15). This allowed remote operation of the NCal either via a remote workstation at the end station or at the LHO control room as well as, saving the data to the LIGO frames. Fail-safes were built into the Beckhoff code as well as the EPICS to monitor parameters such as current usage, spin velocity and communication connection. Should any of the fail-safe parameter exceed their nominal range, the NCal was set to shut down automatically.

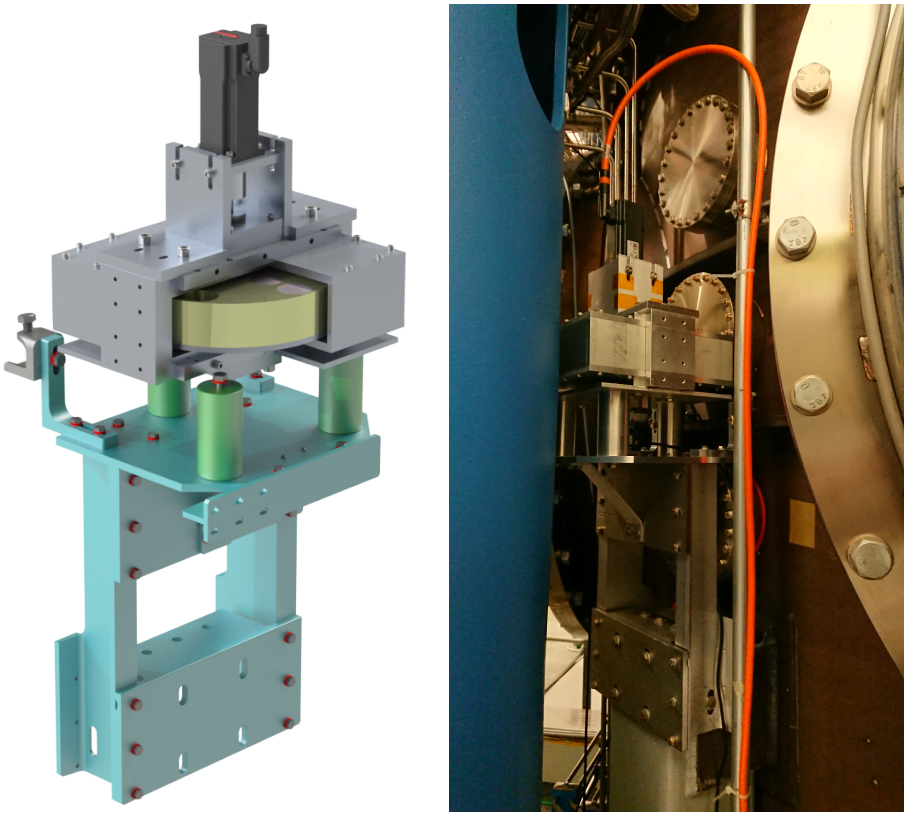

(a) CAD render of the NCal.

(b) Final Install of the NCal at EX.

Figure 5.13: Side by side view of the NCal in CAD and in the final installation at the EX chamber. (a) CAD rendering of the NCAL (grey), with a slice cut out to see the rotor (gold) and the tungsten masses (purple), The NCAL is bolted to cylindrical supports (green) which in turn are bolted to the NCAL mount (turquoise). Two 'L' brackets hold beam clamps (grey) that will attach to the ribbing of the LIGO vacuum chamber. The motor that drives the NCAL (black) is attached to the shaft at the top of the unit. (b) Final installation of the NCal Prototype at LIGO Hanford. On the left is the HEPI pier, in the middle is the NCal and on the right is the chamber vacuum door.

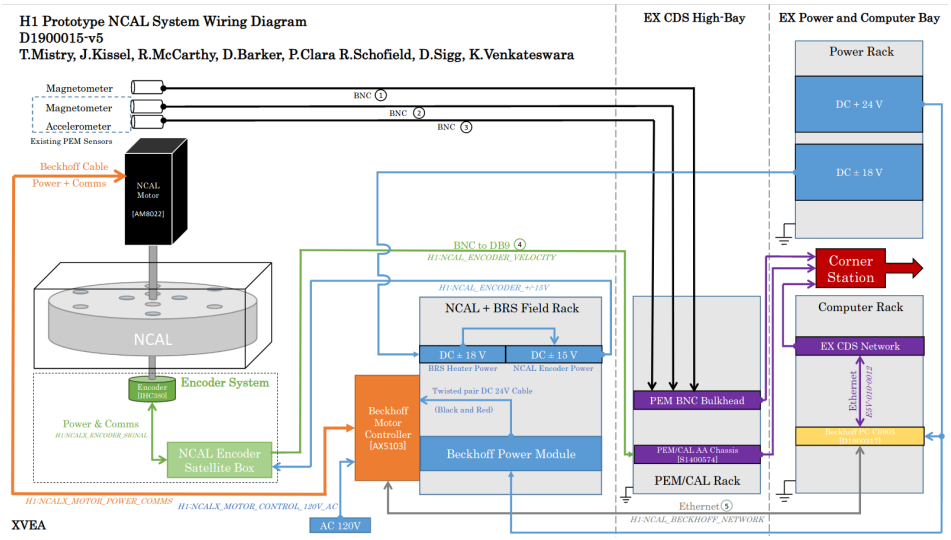

Figure 5.14: H1 NCal prototype wiring diagram for the LHO EX end station. The left side depicts the electronics installed inside the VEA. The middle column denotes the electronics installed in the dedicated electronics bay. The right hand column shows the power and control locations for the NCal and Beckhoff systems.

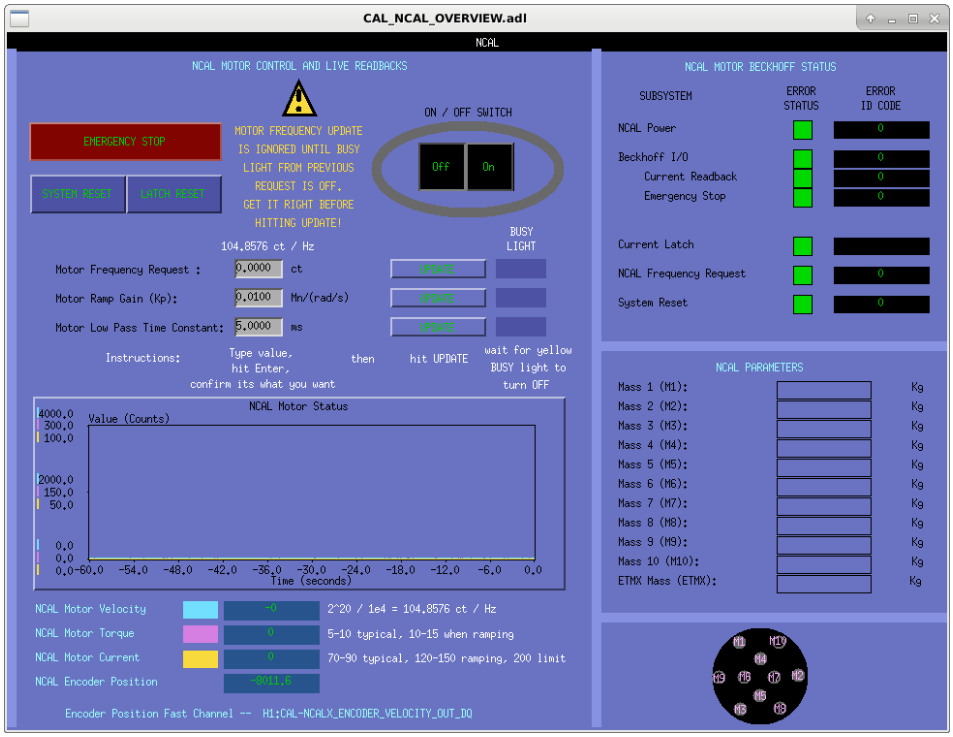

Figure 5.15: Latest iteration of the NCAL MEDM screen used to operate the NCal remotely.

5.2.3 Vibrational and Magnetic Couplings

One requirement of the H1 NCal prototype is to not excite or induce substantial vibrational or magnetic coupling that would reduce the IFO sensitivity. The main concern is exciting the QUAD suspension whilst the NCal is operational however,

the concerns also extend to the impact of the electronics that support and drive the NCal. A good example of electronic noise is the 60Hz line caused by the frequency of mains power. Whilst this noise source is quasi stationary and can be mitigated with relative ease, other non-stationary noise couplings in LIGO can contaminate the sensitive band preventing accurate GW detection. Moreover, for long duration GW sources, such as continuous GWs, persistent low levels of noise can quickly integrate into large unsuitable regions of the LIGO spectrum.

The majority of the aLIGO suspension resonances lie between a bandwidth of 5-20Hz. Each frequency corresponds to a particular suspension stage in the LIGO suspension chain (that ranges from HEPI through to the QUAD suspension) therefore, exciting these stages will cause excessive motion and cause the IFO to ultimately loose lock. Ergo, not only must the primary velocity of the NCAL (spin frequency) not excite the suspension modes, the NCAL harmonics (2f, 3f etc) must also avoid these modes. The suspension modes are intimately modelled though a combination of FEA simulations and controlled excitations, resulting in a state-space model. A reference document, containing all the suspension resonances across all degrees-of-freedom, is constructed as informed by the state-space model.

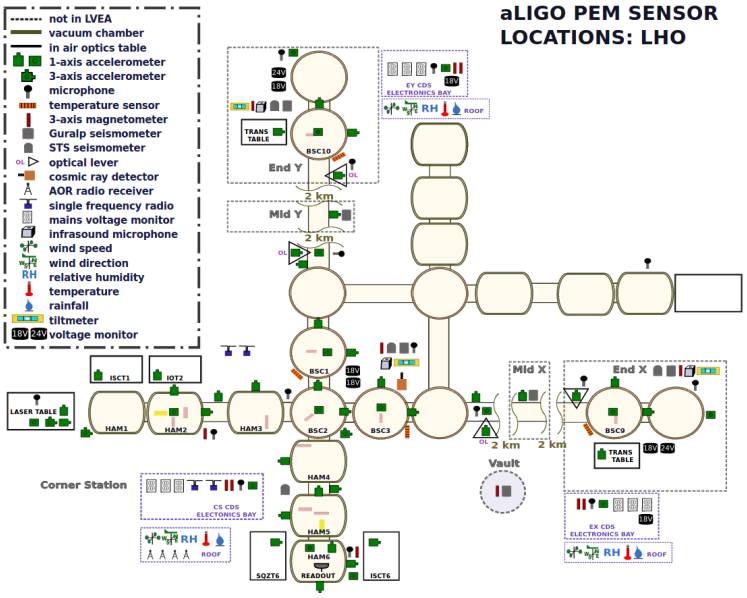

Figure 5.16: Map of the LIGO PEM sensors at the LIGO Hanford Observatory. Credit:

5.2.3.1 Coupling Functions

In order to determine the sensitivity of the LIGO to magnetic and vibrational noise, a coupling function is constructed. The coupling function is a combination of multiple, broadband, injections made with a known noise source. Fixed sensors, placed throughout the LIGO buildings, form the PEM network of sensors. As shown by Figure 5.16, sensors are placed to measure orthogonal degrees of freedom, X,Y and Z. The accelerometers are unidirectional whereas the magnetometers are sensitive in all three degrees of freedom. Overall, the coupling functions allow for calibration of the sensed magnetic and vibrational noise into units of mirror motion, in using of metres. A brief overview of how the coupling functions are obtained will be given first before devolving into their application on estimating the vibrational and magnetic coupling of the NCal.

For evaluating the vibration coupling function, there are two types of injec-

tions. The first is an acoustic injection made with megaphones that are installed within the VEA buildings. The acoustic injections are used to probe the low frequency, $2 - 10$Hz, regions of the LIGO spectrum. The second type of injection is shaker injections. A mechanical shaker is places a set locations thought the LIGO infrastructure and driven a set frequencies to inject signals at higher frequencies, $20 - 2000$Hz. The locations for the shaker can include the beam tubes, chamber surfaces, ground and table-top locations.

The magnetic coupling function is evaluated by injecting combs into the LIGO spectrum using large coils. These coils are are made of a copper wire wound around a bracket located on the VEA walls. Due to the force of the injections falling off at an inverse-square relationship, the coils are several meters in diameter. Despite the coils size, the injections are only sufficient to induce a response in the detector at the most sensitive region 20-1000Hz. Insufficient SNR in the low frequency region, $<$ 20Hz, yield an inconclusive coupling function. As a result, multiple injections are combined to form a best estimate coupling function is formed across the 20-1000Hz region of LHO. In order to probe the lower frequencies, a longer injection time would be required, $\sim$hours in order to achieve sufficient SNR to form a reasonable estimate. Moreover, the current installation of the coils are lack the strength to inject low frequency signals into the IFO however upgrades to the coils during the break between O3b and O4 will aim to resolve this issue. The result of this current limitation means that it is not possible to give a precise estimate of the magnetic coupling but only a best estimate based on the limited data from the coupling function.

5.2.3.2 Computing NCal PEM Coupling

The accelerometers and magnetometer sensors must first be calibrated into units of Force. This is done by taking the raw sensor counts, calculating the Actual Spectral Density, and multiplying it by the coupling function.

$$X_{\mathrm{acc}}(f) = A(f) * CF_{\mathrm{acc}}(f) \tag{5.9}$$
$$X_{\mathrm{mag}}(f) = M(f) * CF_{\mathrm{mag}}(f) \tag{5.10}$$

Both the magnetometer and accelerometers ASDs', now is units of metres, can be converted into Newtons of force by multiplying the ASD by Equation 5.11:

$$F(x) = \frac{1}{m * (2\pi f)^2} \tag{5.11}$$

Where m[kg] is the mass of the test mass, f[Hz] is the frequency vector of the ASD. The results of this calculation is plotted in Figure 5.18 for all degrees of freedom for the accelerometers and magnetometers. Furthermore, the DARM sensitivity is plotted - in units of Force - along with the accelerometers and magnetometers.

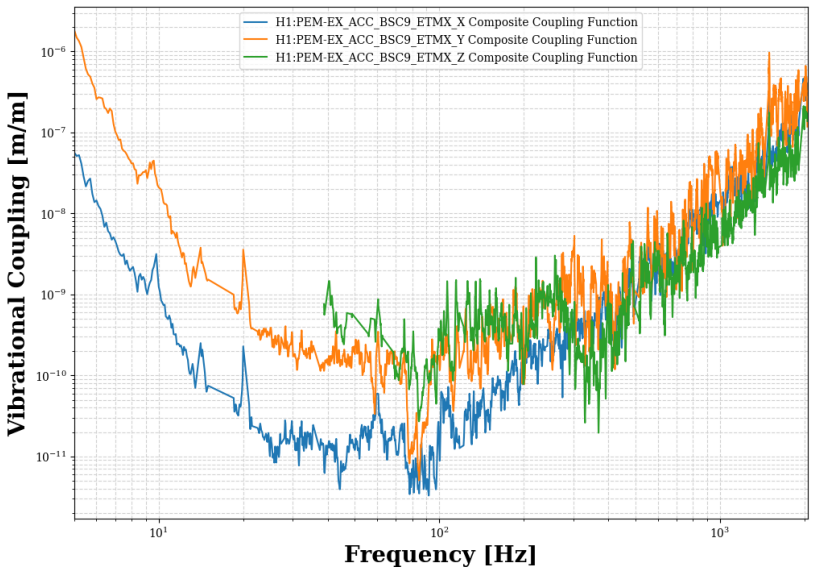

(a) PEM accelerometer coupling function.

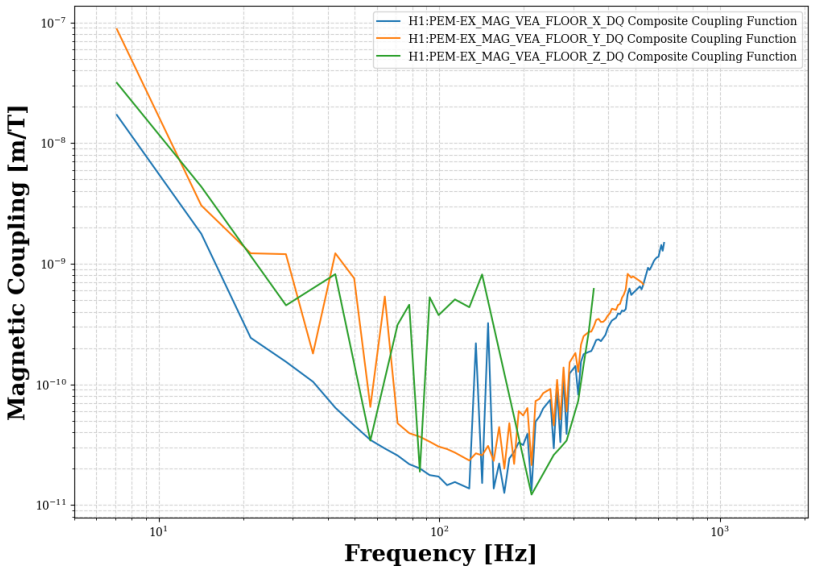

(b) PEM magnetometer coupling function.

Figure 5.17: (a) The XYZ coupling functions of the PEM accelerometers calibrated into units of metres of mirror motion. (b) The XYZ coupling functions of the PEM magnetometer calibrated into units of metres of mirror motion.

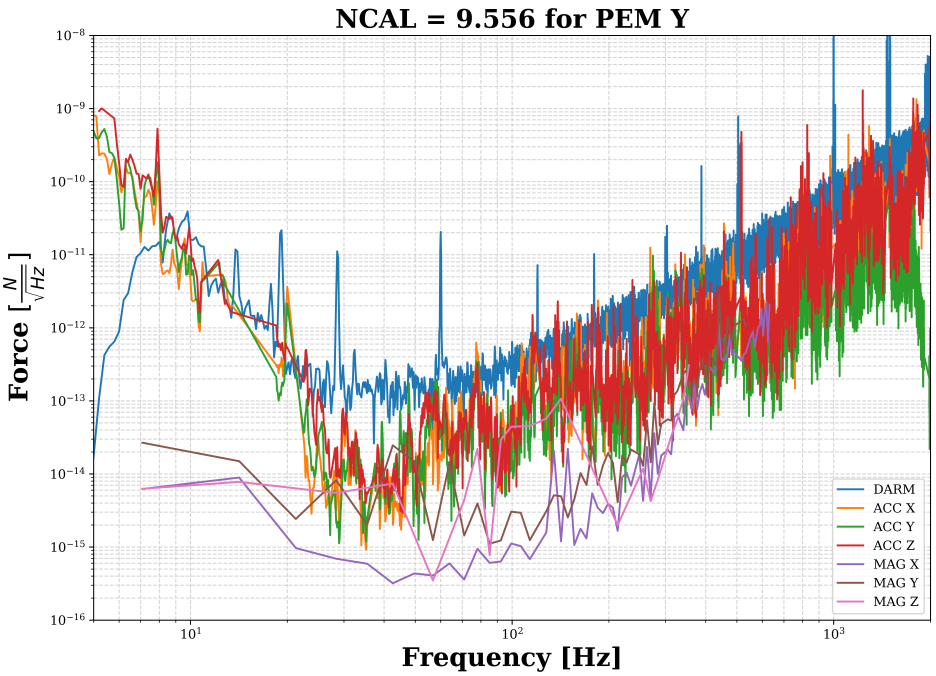

Figure 5.18: ASD's calibrated into units of Force for the accelerometers, magnetometers and LHO DARM during the NCal injection, where the spin velocity was set to 9.556Hz.

The fastest NCal spin velocity was used to provide an upper limit of the NCal magnetic and vibrational impact on the IFO and this is shown in Figure 5.18. The initial implications suggest that NCal is injecting vibrational noise into the IFO at high frequencies, > 60Hz. This can be seen as there are peaks that break above the blue line. In closer inspection, as a result of how the PEM coupling are constructed, the peaks are more than likely artifacts of the coupling function. This is further supported by the fact that the peaks from the sensor do not overlap or correspond with the same peaks seen in DARM. Currently, it is safe to assume that the NCal does not introduce any excessive noise during the short term operation of the device. Further investigation is required to evaluate the long term impact of the NCal and its' subsystems.

5.2.3.3 NCal Electronics Investigations

In order to eliminate the NCal electronics as a source of noise in DARM, a series of ON/OFF tests were performed. This involved switching the power to the NCal electronics ON/OFF over a period of hours, with 20 minute intervals for each power state. The NCal rotor would not be spun, simply, the electronics are being power cycled. Of main concern was the LIGO sensitivity band however, any increase in the background levels or additional spectral features would limit the feasibility of this system in the future. These tests were conducted whilst the IFO was fully locked and in Nominal Low Noise (NLN). With aid of the continuous wave search group, the on-off spectra were relatively indistinguishable from one another across the sensitivity band. This conclusion is drawn tentatively since there are many factors that have yet to be considered as well as many channels that could be potential witnesses to the electronics. One factor to note is that scattering arches contaminate the $35 - 45$Hz region of the spectrum and are sufficiently loud that when taking a power spectrum, they are the dominant feature(s). Moreover, the short 20 minutes integration time may not be enough time for sub-

tle features to be resolvable. To that end, the NCal electronics were left powered on, but the NCal was not spinning for a few days. This time, there are some new spectral features that arise in the $10-100$Hz sensitivity band, Figure 5.19. Whilst these investigations were preliminary, are require future follow-up, it was better to be cautious and switch the NCal off and unplug all the cables. A portable magnetometer was placed next to the NCal and further coherence investigations with this sensor could aid identifying the coupling.

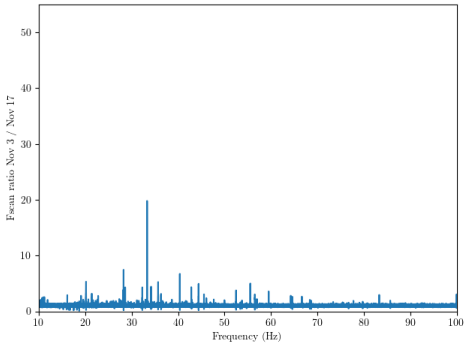

(a) Ratio of Fscan weekly average Nov. 3-10 / Nov. 17-25

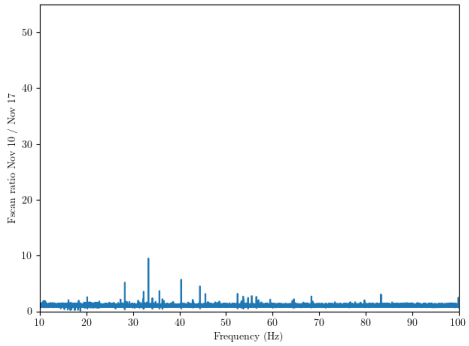

(b) Ratio of Fscan weekly average Nov. 10-17 / Nov. 17-25

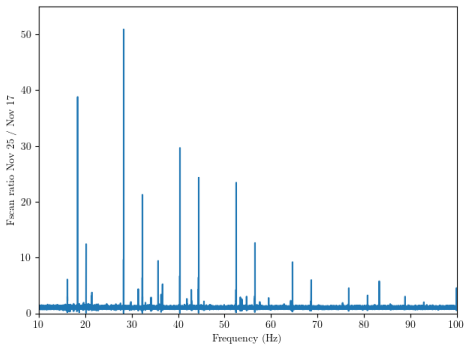

(c) Ratio of Fscan weekly average Nov. 25-30 / Nov. 17-25

Figure 5.19: FScan ratios of weekly averages during the NCal electronics On-Off tests. (a) two weeks prior to tests (b) one week before tests (c) week of the tests - NCal electronics remain on from November 27^{th}.

5.2.4 Metrology

A shown in Equation (5.40), the distance is one of the key parameters that affect the force prediction of the NCal. Therefore careful measurement of the distance of the NCal centre of mass (COM) from it's as-built location to the ETMX COM is required. In this section, we shall cover the method by which we resolved the distance of the NCAL to the LHO EMTX using metrology.

The LIGO sites have been built to millimetre level precision, in part due to the use of metrology (surveying) equipment. During construction and continued infrastructure upgrades, there have been two types of co-ordinates that define the location of all the necessary components and infrastructure. The first type is called the ZEEMAX co-ordinates - the build specification for LIGO (the ideal location where planners wanted the parts to be built or placed). The second is the LIGO Global Co-ordinates that define the 'as-built' positions of the LIGO infrastructure and hardware. This section will describe how the LIGO NCAL was integrated into

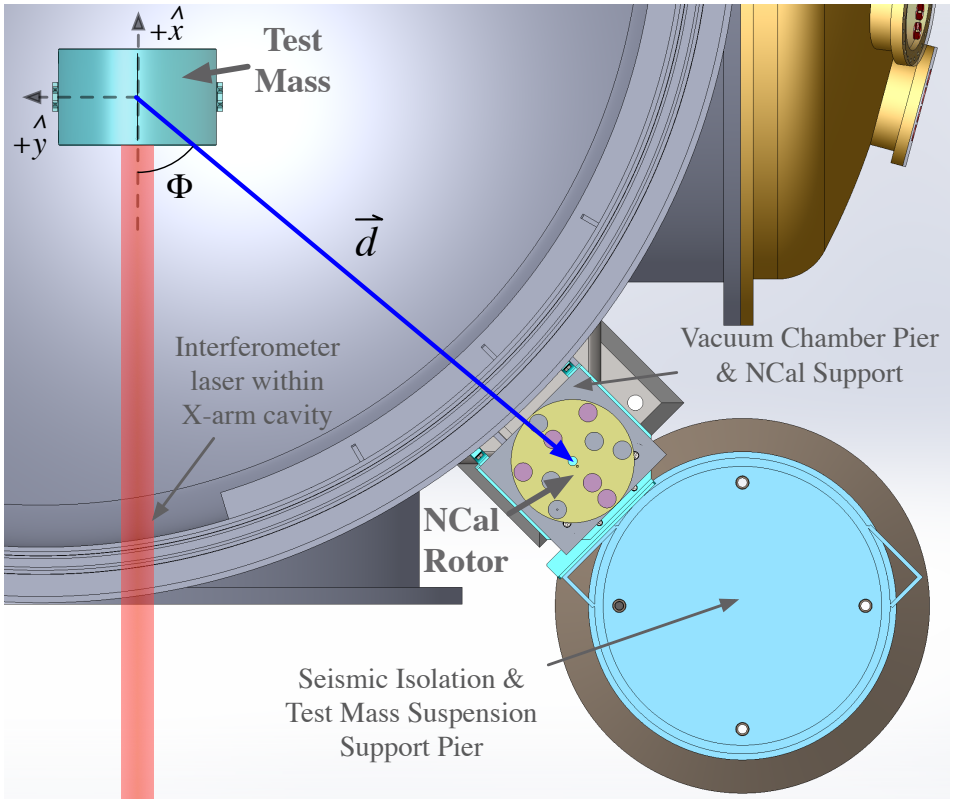

Figure 5.20: Top-down view of a CAD rendering of the NCal and test mass. The enclosure of the NCal as well as the suspension have been suppressed in the CAD model for clarity. The main interferometer laser resonating within the X-arm cavity is shown as it would be when the interferomter is locked. The distance vector, $\vec{d}$, between the NCal center of rotation and Test Mass Center of Mass $\vec{d}$ is indicated in blue, as well as its angle with respect to the $\hat{x}$, interferometer beam, direction (The only component of the NCal force that is measured). Not represented in this rendering is the z offset of the NCal and, in reality, the NCal $\hat{x}\hat{y}$-plane is slightly above of the $\hat{x}\hat{y}$-plane centered on the vertical center of mass of the test mass, and the interferometer beam is not perfectly centered on the front surface of the test mass.

the LIGO Global Co-ordinate system using a SETX total station[176]. A highly detailed account of the surveying process can be found in Mistry et al..

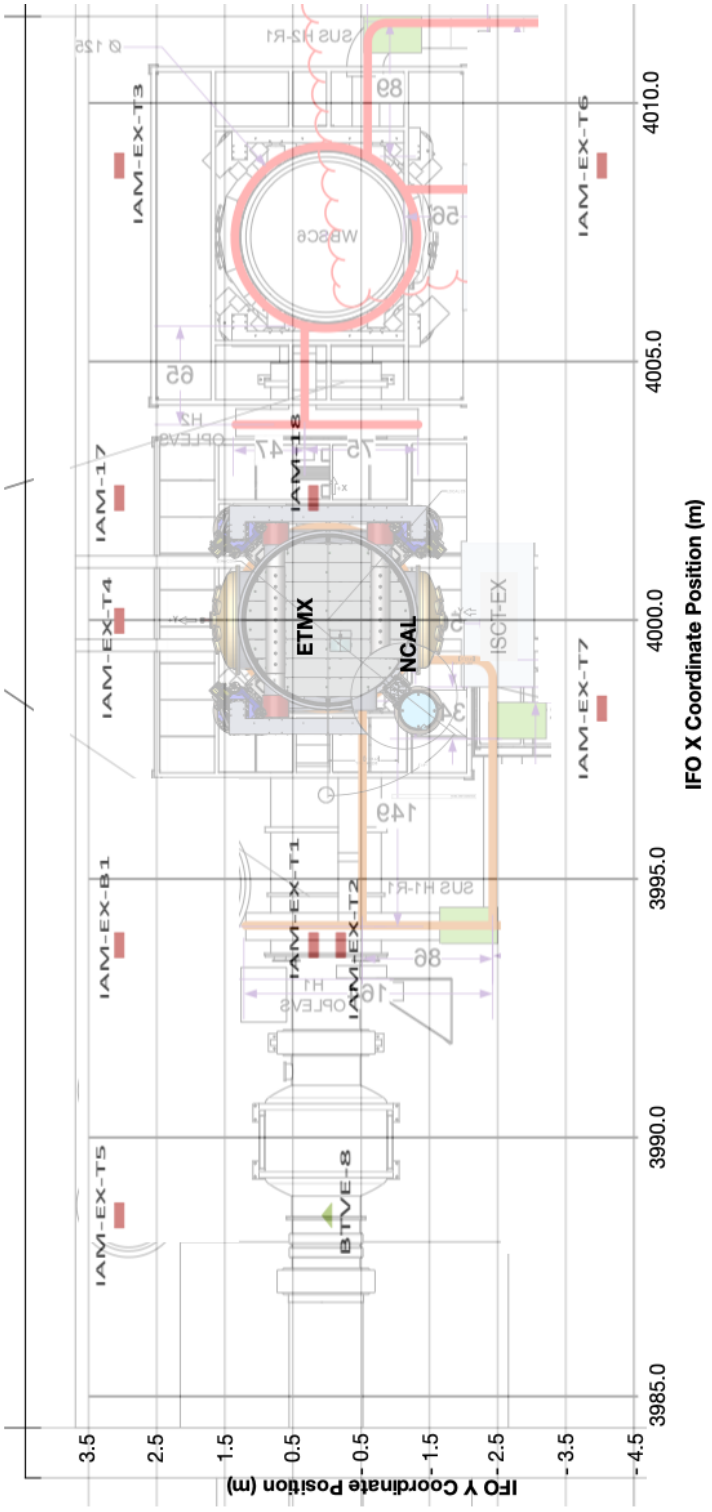

Figure 5.21: The approximate constellation of X/Y position monuments in the LIGO H1 EX VEA building. The NCal and the ETMX optic is also demarcated for additional reference. Note that the X co-ordinate is $\sim$ 4km for ETMX showing us we are at the end of the IFO arm. Moreover, due to constrains during initial construction of the IFO, the ETMX optic located slightly $<$ 4km. The corner station, where the main laser is located, is left of the image.

The following sections will describe how we obtained the key measurements required to survey the NCal into the LIGO global co-ordinates - including the propagation of uncertainties. Once the measurements are defined, a conversion matrix must be constructed. This matrix uses three co-located points common in both co-ordinates systems to establish a matrix transform between the NCal SolidWorks drawing and the total station co-ordinates - which has been calibrated for the LIGO global co-ordinates.

5.2.4.1 Key Measurements for NCal Positioning

In order to define the NCal location in the LIGO global co-ordinates, we must characterise the NCal such that we can express the centre of the NCal rotor in a manor that can transformed into the LIGO global co-ordinates. Therefore, we must establish three orthogonal positions on the NCal that can be externally referenced (sighted) by the surveying total station, Figure 5.22. The following mathematics is taken verbatim from the LIGO NCal surveying documentation [177] which holds more detailed with regards to the surveying process.

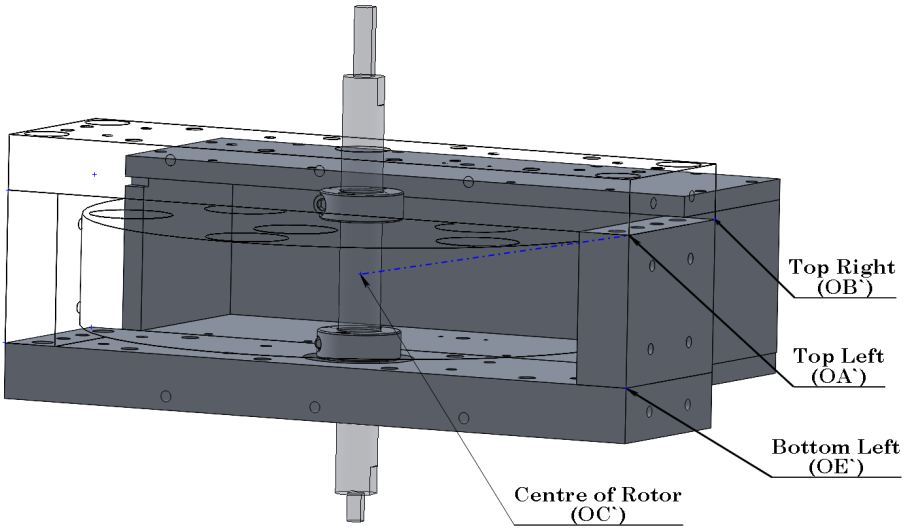

Figure 5.22: A SolidWorks (CAD) view of the NCAL with labels showing the key points on the NCAL frame. All SolidWorks measurements will be denoted with a prime. The centre of the rotor OC is the geometric centre of the NCal rotor.

Naturally, the total station measures in polar co-ordinates [176, 178]. Therefore, in order to match the LIGO global co-ordinate system, we must convert this into Cartesian XYZ co-ordinates before applying them to the NCal. We call the total station raw polar measurements S, θ_H, θ_V (and their uncertainty), which are the distance, the horizontal angle and the vertical angle respective. One caveat to consider is that the total station angles are reported in Degrees Minutes Seconds (DMS) format therefore a further conversion to decimal degrees is required for θ_H and θ_V. Thus, one can then use trigonometry to obtain the XYZ position, S_x, S_y, and S_x of the newly measured point:

$$S_x = S \sin\theta_V \cos(2\pi - \theta_H) \quad (5.12)$$

$$S_y = S \sin\theta_V \sin(2\pi - \theta_H) \quad (5.13)$$

$$S_z = S \cos\theta_V \quad (5.14)$$

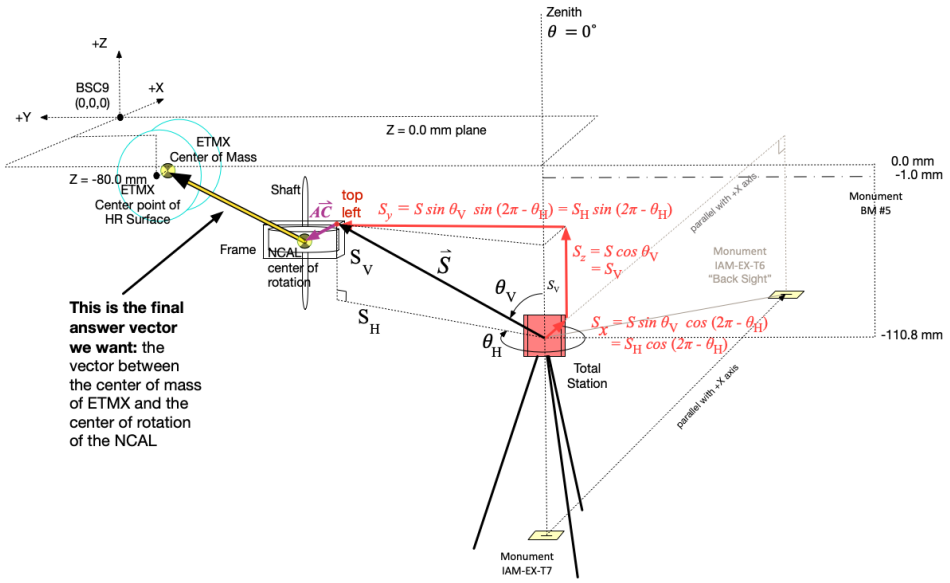

Figure 5.23: Isometric view of the location of the surveying total station with respect to the LHO ETMX optic and NCal. The vector arrow from the total station to the NCal shows the measurement laser direction along with the raw-polar co-ordinates. The red annotations are the conversions required for Cartesian transformation of the measurements. For completeness, we also show the vector from the NCal to the ETMX optic, highlighting the ultimate goal is to survey the distance of the centre of the NCal to the centre of the ETMX optic.

where θ_H is defined within the trigonometric as $-\theta_H$ or equivalently $2\pi - \theta_H$ because of the position of the NCAL system w.r.t. Total Station in our setup, and because the total station defines $+\theta_H$ in the clockwise-as-viewed-from-above direction. Figure 5.23 demonstrates how the total station uses the constellation of monuments, shown in Figure 5.21, to obtain a measurement.

After conversion, the XYZ co-ordinates are only local to the reference monuments. To get the relationship between the new surveyed position, $\overrightarrow{P}$, w.r.t. the global IFO origin $\overrightarrow{O}$, one must add the position of the monument to get the final LIGO global co-ordinate position:

$$\overrightarrow{OP} = \overrightarrow{OM} + \overrightarrow{S} \tag{5.15}$$

5.2.4.2 Combining Co-ordinates for NCal Position

Now we must turn our attention to how to combine the measurements such that we can express the centre of the NCal rotor in LIGO global co-ordinates. First we define the unit-normal coordinate system aligned with LIGO global co-ordinates, such that:

$$\hat{x} \equiv \begin{bmatrix} 1 \\ 0 \\ 0 \end{bmatrix}; \hat{y} \equiv \begin{bmatrix} 0 \\ 1 \\ 0 \end{bmatrix}; \hat{z} \equiv \begin{bmatrix} 0 \\ 0 \\ 1 \end{bmatrix}; \tag{5.16}$$

where:

$$|\hat{x}| = |\hat{y}| = |\hat{z}| = 1 \tag{5.17}$$

Now, with the measurements described in [177] we establish the vectors $\overrightarrow{AB}$ and $\overrightarrow{AE}$ that are located on the NCal frame, as informed by the top left, top right and bottom left total station measurements:

Top Left to Top Right ($\overrightarrow{AB}$):

$$\overrightarrow{AB} \equiv [\overrightarrow{OB} - \overrightarrow{OA}] \equiv AB_x\hat{x} + AB_y\hat{y} + AB_z\hat{z} \tag{5.18}$$

Where:

$$AB_x = (OB_x + \delta OB_x) - (OA_x + \delta OA_x) \tag{5.19a}$$

$$AB_y = (OB_y + \delta OB_y) - (OA_y + \delta OA_y) \tag{5.19b}$$

$$AB_z = (OB_z + \delta OB_z) - (OA_z + \delta OA_z) \tag{5.19c}$$

and

$$|\overrightarrow{AB}| = \sqrt{(AB_x + \delta AB_x)^2 + (AB_y + \delta AB_y)^2 + (AB_z + \delta AB_z)^2} \tag{5.20a}$$

$$\begin{aligned} |\overrightarrow{AB}| \quad = \quad & \Big\{ \Big([OB_x + \delta OB_x] - [OA_x + \delta OA_x] \Big)^2 \\ & + \Big([OB_y + \delta OB_y] - [OA_y + \delta OA_y] \Big)^2 \\ & + \Big([OB_z + \delta OB_z] - [OA_z + \delta OA_z] \Big)^2 \Big\}^{1/2}. \end{aligned} \tag{5.20b}$$

Top Left to Bottom Left ($\overrightarrow{AE}$):

$$\overrightarrow{AE} \equiv [\overrightarrow{OE} - \overrightarrow{OA}] \equiv AE_x\hat{x} + AE_y\hat{y} + AE_z\hat{z} \tag{5.21}$$

Where:

$$AE_x = (OE_x + \delta OE_x) - (OA_x + \delta OA_x) \tag{5.22a}$$

$$AE_y = (OE_y + \delta OE_y) - (OA_y + \delta OA_y) \tag{5.22b}$$

$$AE_z = (OE_z + \delta OE_z) - (OA_z + \delta OA_z) \tag{5.22c}$$

and:

$$|\overrightarrow{AE}| = \sqrt{(AE_x + \delta AE_x)^2 + (AE_y + \delta AE_y)^2 + (AE_z + \delta AE_z)^2} \tag{5.23a}$$

$$\begin{aligned} |\overrightarrow{AB}| \quad = \quad & \Big\{ \Big([OE_x + \delta OE_x] - [OA_x + \delta OA_x] \Big)^2 \\ & + \Big([OE_y + \delta OE_y] - [OA_y + \delta OA_y] \Big)^2 \\ & + \Big([OE_z + \delta OE_z] - [OA_z + \delta OA_z] \Big)^2 \Big\}^{1/2}. \end{aligned} \tag{5.23b}$$

Note that a representative uncertainty term in the measured values of each component, δOA_i (etc) are carried around in the mathematical formalism to help convey where and how each uncertainty will appear. Numerical evaluation, by sampling from the distribution of calculated frame positions, carries the uncertainty.

With these vectors $\overrightarrow{AB}$ and $\overrightarrow{AE}$, we can create an orthonormal basis set of unit vectors that can be directly mapped on to the SolidWorks model using $\overrightarrow{AB}$, $\overrightarrow{AE}$. Their cross-product – defining that the origin of the SolidWorks coordinate system is the top-left point in both $\overrightarrow{OA}$ and $\overrightarrow{OA'}$), and that the frame piece along which $\overrightarrow{AB}$ and $\overrightarrow{AE}$ lie is square and the vectors are perpendicular such that $\overrightarrow{AB}$ = $\overrightarrow{AB'}$ and $\overrightarrow{AE}$ = $\overrightarrow{AE'}$.

Define $\hat{m}$ in terms of $\hat{x}, \hat{y}, \hat{z}$ components of $\overrightarrow{AB}$:

$$\hat{m} \equiv \frac{\overrightarrow{AB}}{|\overrightarrow{AB}|} = m_x\ \hat{x} + m_y\ \hat{y} + m_z\ \hat{z} \tag{5.24}$$

$$= \frac{AB_x}{|\overrightarrow{AB}|}\ \hat{x} + \frac{AB_y}{|\overrightarrow{AB}|}\ \hat{y} + \frac{AB_z}{|\overrightarrow{AB}|}\ \hat{z} \tag{5.25}$$

$$\begin{aligned}\hat{m} = & \frac{(OB_x + \delta OB_x) - (OA_x + \delta OA_x)}{|\overrightarrow{AB}|}\ \hat{x} \\ & + \frac{(OB_y + \delta OB_y) - (OA_y + \delta OA_y)}{|\overrightarrow{AB}|}\ \hat{y} \\ & + \frac{(OB_z + \delta OB_z) - (OA_z + \delta OA_z)}{|\overrightarrow{AB}|}\ \hat{z}\end{aligned} \tag{5.26}$$

Define $\hat{p}$ in terms of $\hat{x}, \hat{y}, \hat{z}$ components of $\overrightarrow{AE}$:

$$\hat{p} \equiv \frac{\overrightarrow{AE}}{|\overrightarrow{AE}|} = p_x\ \hat{x} + p_y\ \hat{y} + p_z\ \hat{z} \tag{5.27}$$

$$= \frac{AE_x}{|\overrightarrow{AE}|}\ \hat{x} + \frac{AE_y}{|\overrightarrow{AE}|}\ \hat{y} + \frac{AE_z}{|\overrightarrow{AE}|}\ \hat{z} \tag{5.28}$$

$$\begin{aligned}\hat{p} = & \frac{(OE_x + \delta OE_x) - (OA_x + \delta OA_x)}{|\overrightarrow{AE}|}\ \hat{x} \\ & + \frac{(OE_y + \delta OE_y) - (OA_y + \delta OA_y)}{|\overrightarrow{AE}|}\ \hat{y} \\ & + \frac{(OE_z + \delta OE_z) - (OA_z + \delta OA_z)}{|\overrightarrow{AE}|}\ \hat{z}\end{aligned} \tag{5.29}$$

Define $\hat{n}$ from $\hat{m}$ and $\hat{p}$:

$$\hat{n} \equiv \hat{m} \times \hat{p} = n_x\,\hat{x} + n_y\,\hat{y} + n_z\,\hat{z} \tag{5.30}$$

$$= \begin{vmatrix} \hat{x} & \hat{y} & \hat{z} \\ m_x & m_y & m_z \\ p_x & p_y & p_z \end{vmatrix} \tag{5.31}$$

$$= \begin{vmatrix} m_y & m_z \\ p_y & p_z \end{vmatrix}\hat{x} + \begin{vmatrix} m_x & m_z \\ p_x & p_z \end{vmatrix}\hat{y} + \begin{vmatrix} m_x & m_y \\ p_x & p_y \end{vmatrix}\hat{z} \tag{5.32}$$

$$= +\left(m_y p_z - m_z p_y\right)\hat{x} - \left(m_x p_z - m_z p_x\right)\hat{y} + \left(m_x p_y - m_y p_x\right)\hat{z} \tag{5.33}$$

$$\begin{aligned}
\hat{n} = &+ \left[\frac{1}{|AB|}\frac{1}{|AE|}\Big(\big[(OB_y + \delta OB_y) - (OA_y + \delta OA_y)\big]\big[(OE_z + \delta OE_z) - (OA_z + \delta OA_z)\big]\right. \\
&\qquad \left. - \big[(OB_z + \delta OB_z) - (OA_z + \delta OA_z)\big]\big[(OE_y + \delta OE_y) - (OA_y + \delta OA_y)\big]\Big)\right]\hat{x} \\
&- \left[\frac{1}{|AB|}\frac{1}{|AE|}\Big(\big[(OB_x + \delta OB_x) - (OA_x + \delta OA_x)\big]\big[(OE_z + \delta OE_z) - (OA_z + \delta OA_z)\big]\right. \\
&\qquad \left. - \big[(OB_z + \delta OB_z) - (OA_z + \delta OA_z)\big]\big[(OE_x + \delta OE_x) - (OA_x + \delta OA_x)\big]\Big)\right]\hat{y} \\
&+ \left[\frac{1}{|AB|}\frac{1}{|AE|}\Big(\big[(OB_x + \delta OB_x) - (OA_x + \delta OA_x)\big]\big[(OE_y + \delta OE_y) - (OA_y + \delta OA_y)\big]\right. \\
&\qquad \left. - \big[(OB_y + \delta OB_y) - (OA_y + \delta OA_y)\big]\big[(OE_x + \delta OE_x) - (OA_x + \delta OA_x)\big]\Big)\right]\hat{z}
\end{aligned} \tag{5.34}$$

With the definition of the SolidWorks co-ordinate system in terms of the measured external frame positions in LIGO global coordinate system, we can map the components of the SolidWorks vector between the $\hat{n}, \hat{m}, \hat{p}$ basis and the center of rotation, $\overrightarrow{AC'}$, and incorporate the uncertainty from the frame measurement.

With these definitions, we can project the values of $\overrightarrow{AC'}$ in the $\hat{n}$, $\hat{m}$, $\hat{p}$ basis we have from Section 5.2.4.1 in to the $\hat{x}$, $\hat{y}$, $\hat{z}$ basis – or, in other words, create the vector $\overrightarrow{OC}$, the vector from the IFO global coordinate system origin to the center of rotation – and we've correctly included the uncertainty in doing so. The following

five systems of equations are all equivalent expressions for the projections.

$$\begin{aligned} OC_x &= AC_n \cos\theta_x + AC_m \cos\psi_x + AC_p \cos\phi_x \\ OC_y &= AC_n \cos\theta_y + AC_m \cos\psi_y + AC_p \cos\phi_y \\ OC_z &= AC_n \cos\theta_z + AC_m \cos\psi_z + AC_p \cos\phi_z \end{aligned} \tag{5.35}$$

$$\overrightarrow{OC} = \mathbf{M}\ \overrightarrow{AC} \tag{5.36}$$

$$\begin{bmatrix} OC_x \\ OC_y \\ OC_z \end{bmatrix} = \begin{bmatrix} \hat{x}\cdot\hat{n} & \hat{x}\cdot\hat{m} & \hat{x}\cdot\hat{p} \\ \hat{y}\cdot\hat{n} & \hat{y}\cdot\hat{m} & \hat{y}\cdot\hat{p} \\ \hat{z}\cdot\hat{n} & \hat{z}\cdot\hat{m} & \hat{z}\cdot\hat{p} \end{bmatrix} \begin{bmatrix} AC_n \\ AC_m \\ AC_p \end{bmatrix} \tag{5.37}$$

$$\begin{aligned} OC_x &= (\hat{x}\cdot\hat{n})\, AC_n + (\hat{x}\cdot\hat{m})\, AC_m + (\hat{x}\cdot\hat{m})\, AC_p \\ OC_y &= (\hat{y}\cdot\hat{n})\, AC_n + (\hat{y}\cdot\hat{m})\, AC_m + (\hat{y}\cdot\hat{p})\, AC_p \\ OC_z &= (\hat{z}\cdot\hat{n})\, AC_n + (\hat{z}\cdot\hat{m})\, AC_m + (\hat{z}\cdot\hat{p})\, AC_p \end{aligned} \tag{5.38}$$

$$\begin{aligned} OC_x &= n_x\ AC_n + m_x\ AC_m + p_x\ AC_p \\ OC_y &= n_y\ AC_n + m_y\ AC_m + p_y\ AC_p \\ OC_z &= n_z\ AC_n + m_z\ AC_m + p_z\ AC_p \end{aligned} \tag{5.39}$$

where from Eq. 5.39 it's clear that we can just multiply the components of $\overrightarrow{AC'}$ by the correct $\hat{x}$, $\hat{y}$, $\hat{z}$ components from Eqs. 5.26, 5.29, and 5.34 of $\hat{m}$, $\hat{n}$, $\hat{p}$, basis to arrive at projection of $\overrightarrow{AC'}$ in to $\overrightarrow{OC}$. Incidentally, the uncertainty of each surveyed frame point's physical position OA, OB, and OE is baked in.

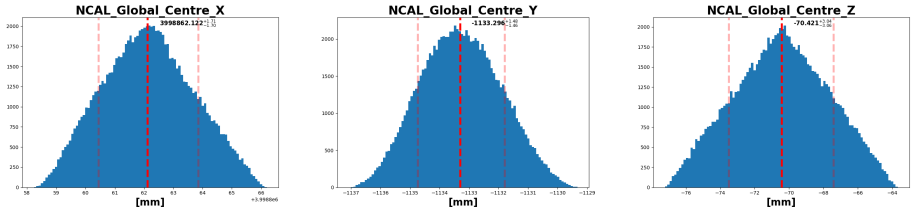

(a) The X co-ordinate of the COM of the H1 NCal rotor.

(b) The Y co-ordinate of the COM of the H1 NCal rotor..

(c) The Z co-ordinate of the COM of the H1 NCal rotor.

Figure 5.24: The centre of the H1 LIGO NCal Prototype rotor given in LIGO global co-ordinates. The distribution is a result of nested sampling from uniform parameters.

The morphology of the distributions in Figure 5.24 are not Gaussian. Curiously, the Z co-ordinate evolves into a triangular shape rather than the bell like curves of the X an d Y co-ordinates. This is mainly because the Z co-ordinate is only translated linearly whereas the X and Y co-ordinates are non-linear transformations. The resulting distributions, yielded from maths in Section 5.2.4, are a compound of the multiple linear and non-linear transforms. As mentioned in Section 5.2.3, the uncertainties are built into the distributions therefore sampling form these distributions adequately characterise the as-built location of the centre of the NCal to the centre of the LHO ETMX optic.

5.2.5 Modelling

The Newtonian Calibrator (NCal) is a mechanical calibration technique, used as an independent reference for absolute length calibration for the LIGO interferometer. The core principle of the device utilises the inverse square law of Newtonian Gravity:

$$F = \frac{GM_i m_j}{r^2} \tag{5.40}$$

Where $F\,[\mathrm{Nm}^{-2}]$ is the magnitude of the attractive force, $G\,[\mathrm{kg}^{-1}\mathrm{m}^3\mathrm{s}^{-2}]$ is the universal Gravitational Constant, $M_i\,[\mathrm{kg}]$ is the mass of the primary object, $m_j\,[\mathrm{kg}]$ is the mass of the secondary object and, $r\,[\mathrm{m}]$ is the radial distance between the two mass objects. Three methods have been developed to model the NCAL force on the test mass: FEA modelling; point mass and, multipole analysis. All methods are numerically evaluated. This allows for the propagation of uncertainties to be built into sampled distributions. In the next few sections, each of the methods will be outlined. A comparison of the different methods can be found in Section IV of Kennedy [154]. The affects of the uncertainties in the force modelling will be briefly described before moving into applying the models to the first injection of a NCal signal in DARM.

5.2.5.1 Point Mass Approximation

This is the simplest form of modelling the NCal force on the test mass. The quadrupole (2f) model is adopted from Matone et al and Estevez et al, and following a similar treatment, to extend the techniques to the hexapole (3f) model. Equations 5.41 and 5.41 are the results of expansions to second and third order in r_q/d and r_h/d, respectively. A comprehensive derivation can be found in Datrier et al therefore, the final solutions are shown here. Underpinning these equations lies two key assumptions: The NCal rotor is in the same plane as the test mass and, the geometry of the masses is ignored. Therefore, the resulting numerical outputs from Equations 5.41 and 5.41 are used as consistency check for the more details models in the next two sections.

$$\begin{aligned} F_x^{(2f)} &= \frac{9}{2}\frac{GMmr_q^2}{d^4} \\ &\quad \times\ \zeta^{-5/2}\left[\left(\frac{5}{6}\frac{1}{\zeta} - \frac{2}{3}\right)\cos(2\theta - \Phi)\right. \\ &\quad \left. +\ \frac{5}{6}\frac{1}{\zeta}\cos(2\theta - 3\Phi)\right], \end{aligned} \tag{5.41}$$

where G is the gravitational constant, M is the mass of the test mass, m is the mass of a tungsten cylinder, d is the distance between the rotor and test mass, Φ and z are the azimuthal and vertical position of the rotor (as in Figure 5.20), r_q is the quadrupole radius, and $\zeta = 1 + (z/d)^2$. The angle of the rotor, θ, cycles once per rotation (i.e. $\theta = 2\pi f t$).

Under the same assumptions, the x-component of the hexapole force is:

$$\begin{aligned} F_x^{(3f)} &= \frac{15}{2}\frac{GMmr_h^3}{d^5} \\ &\quad \times\ \zeta^{-7/2}\left[\left(\frac{7}{8}\frac{1}{\zeta} - \frac{3}{4}\right)\cos(3\theta - 2\Phi)\right. \\ &\quad \left. +\ \frac{7}{8}\frac{1}{\zeta}\cos(3\theta - 4\Phi)\right] \end{aligned} \tag{5.42}$$

where r_h is the radius of the hexapole mass arrangement.

5.2.5.2 Finite Element Analysis

This method deconstructs the geometry of the NCal and the test mass into a 'cloud' of finite elements. The final force is modelled by summing over elements from the 'source' cloud of points (the NCal) to the 'test cloud' of points (the ETMX optic). Here, 'cloud' means an even distribution of points, much like a finite element mesh in 3-D however, the density and parameters or the points can be tweaked to better reflect the real hardware. Therefore, we define the modelled Force F as:

$$\vec{F} = \sum_i \sum_j \frac{G m_i M_j}{d_{ij}^2} \, \hat{d}_{ij} \tag{5.43}$$

where m_i is a point mass within the source cloud (the NCal), M_j is a point mass within the test cloud (the test mass), and d_{ij} is the magnitude of the position vector from the i-th point to the j-th point.

5.2.5.3 Multipole Analysis

In addition to the finite-element simulation, we developed a multipole-based analysis which calculates the force by breaking each object into its gravitational multipole moments. With this method, the force can be found with:

$$\vec{F} = 4\pi G \sum_{l=0}^{\infty} \sum_{m=-l}^{l} \frac{1}{2l+1} Q_{lm} \nabla q_{lm} \tag{5.44}$$

where Q_{lm} is the "outer" multipole and q_{lm} is the "inner" multipole. For our geometry the inner multipole corresponds to the NCal while the outer corresponds to the test mass.

5.2.5.4 Impact of Uncertainties

A final step in modelling the NCal force is to consider the gravitational and non-gravitational couplings. Quantification of the uncertainties applied to the modelling force are given in Table III in Ross et al. Here, a brief explanation to the origins of each of the effects are detailed.

The gravitational coupling refer to excess mirror motion as a result of the NCal force affecting the QUAD suspension thereby transferring the energy via the mechanical hard points (such as suspension fibres). The main source of the indirect gravitational coupling, though the penultimate mass, yields $< 0.18\%$ uncertainty at the $2f$ and $< 1\%$ at the $3f$. The non-gravitational couplings take the form of magnetic and vibrational effects - which we have already addressed in Section 5.2.3.

One of the main sources of uncertainties that persist is the precision of the distance measurement. Table 5.2 highlights that, using the total station, inherits the largest uncertainty in the distance (z) parameter. One novel idea to potentially overcome this is using the ratio of the $2f$ and $3f$ signals. In order to achieve this, the $2f$ and $3f$ signals must be at the same frequency in the LIGO spectrum. Furthermore, since the NCal can only inject a single frequency at a time, the IFO must remain locked thought the injection of both injections. Moreover, the integration time required to reduce the uncertainty below that of the total station surveying would require ~ 56 hours per frequency [37,38 in Ross et al.].

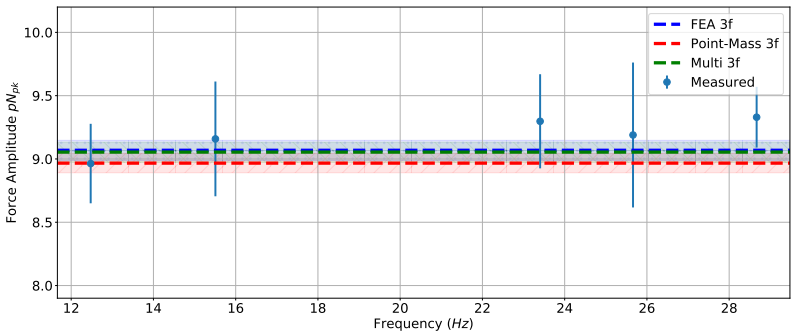

(a) NCAL second harmonic (2F) measured vs model.

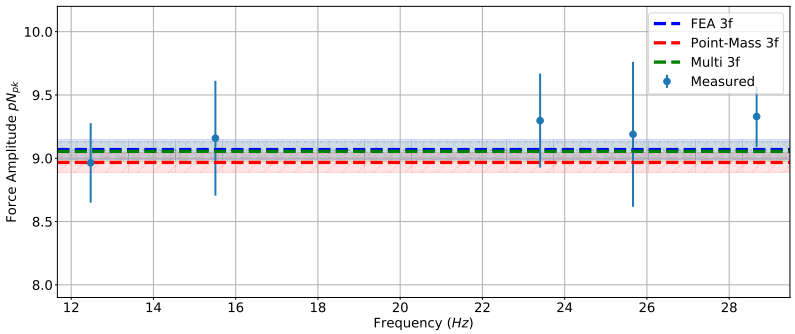

(b) NCAL third harmonic (3F) measured vs model.

Figure 5.25: (a) The modelled vs measured forces of the NCal for the quadrupole arrangement of masses. (b) The modelled vs measured forces of the NCal for the hexapole arrangement of masses. In both cases, the model and the measured show frequency independence of the Force in the LIGO optic.

Parameter	**Mean**	**Uncertainty**	**Distribution**
Tungsten Cylinder Mass m	1.0558 kg	0.3 g	Gaussian
Tungsten Cylinder Radius r_c	1.968 cm	2.5 μm	Uniform
Tungsten Cylinder Length l_c	5.08 cm	5 μm	Uniform
Quadrupole Radius r_q	6.033 cm	5 μm	Uniform
Hexapole Radius r_h	10.478 cm	5 μm	Uniform
Test Mass M	39.680 kg	10 g	Uniform
Test Mass Length l_{tm}	199.8 mm	0.1 mm	Uniform
Test Mass Radius r_{tm}	170.11 mm	0.05 mm	Uniform
Test Mass Flat Width w_{tm}	326.5 mm	0.05 mm	Uniform
Rotor Radial Position ρ	1180.2 mm	2.4 mm	Numerical
Rotor Angle Φ	52.24 deg	0.08 deg	Numerical
Rotor Vertical Position z	10.0 mm	3.0 mm	Numerical

Table 5.2: Parameters of the NCal rotor and LIGO test mass, uncertainties, and their corresponding distribution types that are used in the Force modelling of the NCal on the Test Mass. For parameter uncertainties described by a Gaussian distribution the stated uncertainty indicates the σ-value; for uniform it indicates the half-width; and for uncertainties estimated numerically, the 68% credible interval. Reproduced from Ross et al..

GPS Time	UTC Time	NCal 1f (Drive) [Hz]	NCal 2f [Hz]	NCal 3f [Hz]
1259535305	04-10-2019 22:54:47	3.252	6.504	9.756
1259535460	04-10-2019 22:57:22	4.158	8.316	12.474
1259535595	04-10-2019 22:59:37	5.169	10.338	15.507
1259535725	04-10-2019 23:01:47	7.804	15.602	23.403
1259535880	04-10-2019 23:04:22	8.554	17.109	26.663
1259536015	04-10-2019 23:06:37	9.556	19.111	28.667

Table 5.3: The date and time of NCal drive velocity (injections). The 2f and 3f columns are calculated from the 1f drive. These are plotted in Figure 5.27.

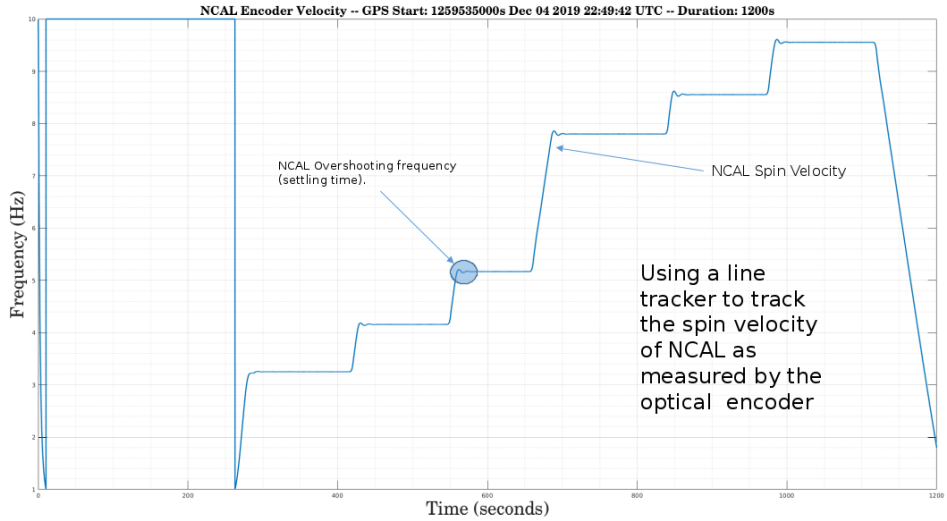

Figure 5.26: Using IWAVE to track the spin velocity of the NCal as measured by the optical encoder. The highlighted circle shows where the NCal velocity slightly overshoots the requested frequency and the motor drive damps the velocity to compensate for this.

5.2.6 Signals and Systematics

The NCAL was controlled remotely from the LHO control room using a dedicated MEDM screen, 5.15. Since the NCAL is always set to a low power state, the NCAL needs to be remotely activated. Before the NCAL was enabled, the LHO IFO needed to be configured into a particular state to ensure minimal impact to sensitive subsystems and as to not contaminate the science (calibrated strain) data. First, the IFO had to be locked for a least 60 minutes. This was ensure that the IFO was sufficiently thermally equilibrated. Next, the IFO had to be in Nominal Low Noise (NLN), a state whereby the LHO IFO was being held in resonance (locked) by the various control systems. In addition, the IFO must not be in observing mode to ensure no NCAL injected signals are contaminating the science frames.

While it was possible to have the guardian system automate the NCAL injection scheme, we opted to run the injections manually. Since this would be the first time such as system has been implemented, manually operating the NCAL would allowed greater flexibility in controlling and monitoring the IFO and the NCAL. A pre-determined list of drive frequencies were selected to avoid key frequency hotspots such as suspension resonances and control lines. The drive frequencies are reported in Table 5.3.

Earlier, we mentioned that the NCal has a rotary encoder attached to the

same shaft that connects the motor to the rotor. The signal from the encoder is a sawtooth signal since it measures the phase of rotation using a calibrated disc This encoder is given a dedicated channel, Figure 5.14, that is saved at a faster sampling rate (4096Hz). This is required so that we can precisely measure the NCal velocity which, whilst not so important for force modelling, serves as a useful probe for the stability of the drive. The fast sampling rate allows greater spatial resolution in frequency space meaning, we can capture higher order effects such as jitter when the NCal reaches a steady state. In Figure 5.26, we show that we can measure the spin velocity be using IWAVE to track the sawtooth wave. The abilty to do this has two main implications. One is that we can use this signal to form a quick real-time NCal systemic error calculation, much in the same way as PCal, using Equation 5.7. The other impication is that we can measure, with a high degree of accuacy thanks to the fast sampling rate, the stability of the drive in real time (i.e. not need to use Fourier Analysis and take long duration FFTs). We can see in Figure 5.26 that as the drive approaches the requested frequency, it overshoots slightly and is damped by the Beckhoff controller until it reaches equilibrium. It could be possible to adjust the motor parameters to remove this overshoot and IWAVE can give real-time analysis on the success of the tuning.

The first injection was completed on 04 Dec 2019 and a second, much longer NCal injection was made on 03 September 2020. The first injection was a short stint of 6 different spin velocities each lasting 120 seconds, summarised in Table 5.3. During the analysis of this data, Figure 5.27, whist we had good prediction between out estimate of the signal, the lack of sufficient integration time resulted in large uncertainties - mainly due to low SNR. The second injection we intend to improve our methods and compare NCAL against PCAL, with high SNR.

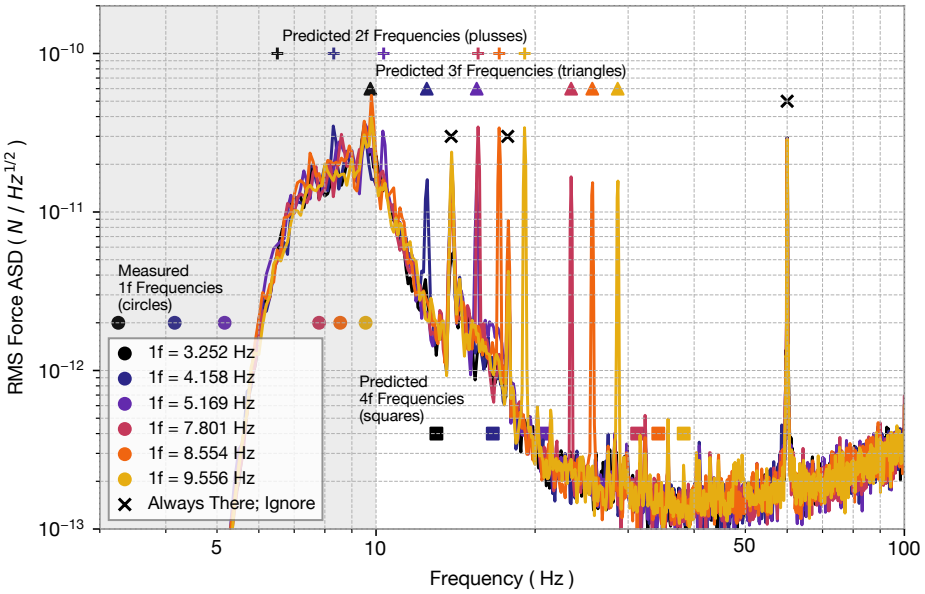

Figure 5.27: First injection campaign if the H1 NCal prototype. The triangles and the plus symbols show the predicted location of the 2f, 3f and the 4f signal respectively. However, the amplitude is not predicted and the symbol location on the y-axis is purely for ease of viewing. The black crosses denote frequency features that are already known and therefore can be ignored and not form part of further analysis. Additionally, the circles are the NCal 1f drive frequencies that will produce the higher harmonic signals. Again, the amplitude is not of importance since the amplitude is fixed by the NCal physically installed location.

$1f$ (Hz)	$2f$ (Hz)	$F_x^{(2f)}$ (pN)	$3f$ (Hz)	$F_x^{(3f)}$ (pN)
4.16	8.32	–	12.45	$8.79^{\pm 0.32}_{\pm 3.61\%}$
5.17	10.34	$16.59^{\pm 2.33}_{\pm 14.05\%}$	15.51	$8.98^{\pm 0.46}_{\pm 5.07\%}$
7.80	15.60	$19.28^{\pm 0.30}_{\pm 1.56\%}$	23.40	$9.12^{\pm 0.37}_{\pm 4.10\%}$
8.55	17.11	$19.10^{\pm 0.47}_{\pm 2.44\%}$	25.66	$9.01^{\pm 0.57}_{\pm 6.36\%}$
9.56	19.11	$19.28^{\pm 0.21}_{\pm 1.12\%}$	28.67	$9.15^{\pm 0.24}_{\pm 2.66\%}$

Table 5.4: Measured force amplitudes, $F_x^{(2f)}$ and $F_x^{(3f)}$, with corrections applied for extraneous couplings at the expected quadrupole $2f$ and hexapole $3f$ frequencies.

5.2.6.1 Absolute Calibration

In order to use the NCal as a source of absolute length reference, we adopt the current techniques used in the full production of the calibration. Namely, taking the response ratio of the IFO to the injection described by Equation 5.7. This was briefly introduced in Section 5.1.1 however further details can be found in Sun et al.

The dimensionless strain recorded by the IFO can be converted into force with:

$$F_x = \frac{L_x h}{S} \tag{5.45}$$

Where: F_x [N] is the force in the x-direction; L_x [m] is the length of the x-arm; h is the dimensionless strain measured by the IFO and, S is the force-to-displacement response of the quadruple suspension.

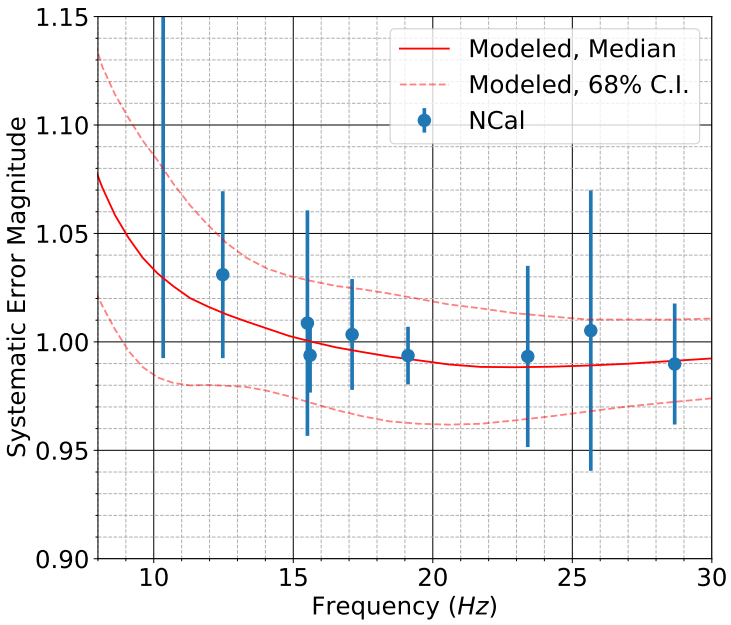

Figure 5.28: Comparison of the NCal measured systematic error against the calibration pipeline model of the systematic error - in magnitude. We are currently unable to ascertain the phase systematic error due to the rotary encoder not being calibrated to the NCal rotor.

In the ideal case, $\eta_R = 1$. This would indicate no systematic error is present. From Figure 5.28, the NCal is in agreement with the calibration systematic error across the NCal measurement range. Figure 5.28 is only half the picture and ideally, we would like to evaluate the phase systematic error. Unfortunately, the absolute phase of the NCal, at the time of these measurements, was unknown due to the rotary encoder not being calibrated to the NCal rotor.

5.2.7 Limitations

One of the main limitations of the NCal is the ability to inject signals beyond 100Hz. This is in part due to safety concerns around spinning masses close to the LIGO vacuum chamber. This means it is not possible to calibrate the full sensitivity band of the IFO using the NCal alone. Additionally, the amplitude of the injection cannot be controlled since the amplitude is inversely proportional to the distance of the NCal - which is currently fixed in place. Whilst the rotary encoder is attached to the NCal to record the phase, it was not calibrated to the rotor position. As a result, it is possible to cross-check the calibration however only in magnitude and not the phase.

5.3 Future Work, Upgrades and Impact

The ultimate goal is for the NCAL to form part of the consensus estimate for calibration by becoming another absolute length scale calibration. This involves combining absolute calibration from different sources of absolute references. Such a challenging task will allow a larger bandwidth of the LIGO strain to be available for searching for GW sources. In order for the NCal to become a full time integrated system, precise modelling and evaluation of the NCal and its' subsystems will need to be completed. This would include: full mechanical system modelling for stress analysis; B&K modelling and experimental verification for frequency mode identification; full vibrational and magnetic estimation and characterisation and, improved distance measurement.

The direct drive of the NCal motor is highly configurable, with options to control the velocity and acceleration of rotation. Better understanding of how to use the motor settings to drive the NCal could not only improve the efficiency of the motor but also allow for alternative injection regimes (such as swept signals). Moreover, the electronics themselves will better isolation in order to prevent noise from entering the strain data. For this, class A/B transistor amplifiers could be instead of the switching FET amplifiers used in the motor controller. This is an active area of research that would have been undertaken at the University of Sheffield however there was not sufficient time to complete this. Whilst further investigations are required to definitively prove the existence of NCal induced noise, reducing the noise impact of the NCal will increase the likelihood that the NCal can be operational during science runs.

Improving the distance measurement is important to reducing the uncertainty in the force estimation. Since it is currently the largest source of uncertainty in the force modelling analysis, reducing this uncertainty will greatly improve the force estimate thereby improving the NCal calibration. Since it was shown that using the ratio of the $2f$ and $3f$ would be unfeasible, another method is being investigated. This stems from the VIRGO and KAGRA implementation whereby multiple NCals are used in tandem. In addition, varying the distance of the NCal to the test mass in order to vary the amplitude of injection.

The full impact of an NCal type device, beyond calibration, is an ongoing investigation. Whilst VIRGO and KAGRA have already adopted NCal style systems into their full production calibration, LIGO has yet to integrate such a system.

Primarily, the PCal exceeds the NCal in multiple requirements. This doesn't mean the NCal is obsolete. Mainly, using the NCal to verify the PCal is a useful asset to validate the calibration of the IFO. The relatively low cost, simplicity of the NCal has proved that it can compete with the PCal system.

5.3.1 Future of Calibration for LIGO

The calibration of gravitational wave interferometers is an ever evolving conundrum that attempts to balance precision instrument science with accurate strain data. The method to compute the calibrated strain has become more robust with the implementation of automation. Going forward into O4 and beyond, the calibration pipeline aims to become a fully automated, one-and-done calibration. In order to achieve this, continuous measurement of the IFO response with minimal impact to search pipelines, needs to be devised methods which are currently under investigation.

Furthermore, faithful reconstruction of the strain is only half the story. With GW search pipelines becoming more sophisticated, follow-up (EM) searches of GW candidates require accurate sky positions within a few seconds of the event. Therefore, the calibration pipeline is being assessed in order to determine the feasibility of a single low latency calibration data produce. The impact of calibration uncertainties on GW search parameters are being investigated.

Chapter 6

Conclusions and Future Work

> If you no longer go for a gap that exists, you are no longer a racing driver
>
> Ayerton Senna

Since the landmark discovery of gravitational waves by LIGO, observatories have become more sensitive and understanding of their operation has improved. The work presented here marks a experimental and instrument design contributions to aspects of the detector critical to future enhancements in performance and sensitivity.

Line (frequency) tracking is becoming a wider topic of discussion amongst the LIGO/VIGO working groups. The simplicity in the tool lies only one free parameter that the user need to concern themselves with (τ) and the performance can be easily interpreted with the transfer function. IWAVE is computationally cheap such that the multi-line tracker has been implemented onto the LIGO front end. IWAVE has been demonstrated to be a competent tool for tracking frequencies in a number of LIGO applications in real-time using the front end version and offline using the LIGO FRAME data. It can accurately resolve the double peaks of violin modes, that are often very tightly spaced in frequency that usually require very long FFTs.

The tracking of the test mass body modes has resulted in a novel metric to evaluate the thermal performance of the LIGO optics. Since it is not possible to attach a temperature sensor to the optics, as they are too noisy, proxy measurements are necessary in order to determine the thermal state of the optics. As laser power increases in the arm cavities of interferometers, thermal heating effects such as thermo-optic lenses, absorption of laser power by the HR surfaces and scattered light become more problematic. The use of the test mass thermometers can give commissioners a useful measure of the effectiveness of Thermal Control System (TCS) employed to suppress thermal effects. Furthermore, the tracking of the test mass body modes can be integrated into a large scale effort to extract thermal parameters such as power absorption, form factors and higher order effect such as differential heating from point absorbers. Moreover, for future planning of GW observatories, the test mass thermometers can be useful for modelling thermal performance - particularly important for cryogenic and large baseline observatories.

The LIGO NCal received a lot of interest from the wider calibration working group. This is mainly in part of the initial results being much better than expected and the installation occurred in a rather short time scale. The installation and

commissioning was possible by working closely with LIGO Hanford electronic, vacuum, mechanical and software engineers to full integrate the NCal into the LIGO architecture. It will continue to receive updates and a dedicated group of individual developing the next generation of the device. Whilst the distance estimate of the NCal to the test mass remains the main source of uncertainty, the precise measurement using surveying equipment along with a full numerical pipeline to evaluate the systematic error on the distance has resulted in a $\sim$ 1 mm level of uncertainty. Other areas of improvement for the NCal can include: calibrating the phase of the NCal rotor with the optical encoder for improved torque modelling and, reducing the electronic noise coupling through the use of class A/B amplifiers. Furthermore, despite the short initial data set used to obtain an NCal systematic error vs PCal informed calibration of the LIGO strain - the longer NCal integration data will improve this result of the NCal considerably. Furthermore, this new data set will also be able to produce the first NCal calibration of the LIGO interferometer. The success of the NCal at LIGO has prompted a wider collaboration between the LIGO NCal working group and that of VIRGO, KAGRA and LIGO India.

Bibliography

[1] Edward J. Daw, Ian J. Hollows, Elliot L. Jones, Ross Kennedy, Timesh Mistry, Tega B. Edo, Maxime Fays, and Lilli Sun. Iwave – an adaptive filter approach to phase lock and the dynamic characterisation of pseudo-harmonic waves. 2021. doi: 10.48550/ARXIV.2109.00104. URL https://arxiv.org/abs/2109.00104. Accepted for publication in RSI but has yet to be listed.

[2] Ling Sun, Evan Goetz, Jeffrey S Kissel, Joseph Betzwieser, Sudarshan Karki, Aaron Viets, Madeline Wade, Dripta Bhattacharjee, Vladimir Bossilkov, Pep B Covas, Laurence E H Datrier, Rachel Gray, Shivaraj Kandhasamy, Yannick K Lecoeuche, Gregory Mendell, Timesh Mistry, Ethan Payne, Richard L Savage, Alan J Weinstein, Stuart Aston, Aaron Buikema, Craig Cahillane, Jenne C Driggers, Sheila E Dwyer, Rahul Kumar, and Alexander Urban. Characterization of systematic error in advanced LIGO calibration. *Classical and Quantum Gravity*, 37(22):225008, oct 2020. doi: 10.1088/1361-6382/abb14e. URL https://doi.org/10.1088/1361-6382/abb14e.

[3] A. Buikema et al. Sensitivity and performance of the advanced ligo detectors in the third observing run. *Phys. Rev. D*, 102:062003, Sep 2020. doi: 10.1103/PhysRevD.102.062003. URL https://link.aps.org/doi/10.1103/PhysRevD.102.062003.

[4] Michael P. Ross, Timesh Mistry, Laurence Datrier, Jeff Kissel, Krishna Venkateswara, Colin Weller, Kavic Kumar, Charlie Hagedorn, Eric Adelberger, John Lee, Erik Shaw, Patrick Thomas, David Barker, Filiberto Clara, Bubba Gateley, Tyler M. Guidry, Ed Daw, Martin Hendry, and Jens Gundlach. Initial results from the ligo newtonian calibrator. *Phys. Rev. D*, 104:082006, Oct 2021. doi: 10.1103/PhysRevD.104.082006. URL https://link.aps.org/doi/10.1103/PhysRevD.104.082006.

[5] J Aasi et al. Advanced LIGO. *Classical and Quantum Gravity*, 32(7):074001, mar 2015. doi: 10.1088/0264-9381/32/7/074001. URL https://doi.org/10.1088/0264-9381/32/7/074001.

[6] S M Aston et al. Update on quadruple suspension design for advanced LIGO. *Classical and Quantum Gravity*, 29(23):235004, oct 2012. doi: 10.1088/0264-9381/29/23/235004. URL https://doi.org/10.1088/0264-9381/29/23/235004.

[7] Lisamission.org. URL https://www.elisascience.org/.

[8] M. Armano et al. Beyond the required lisa free-fall performance: New lisa pathfinder results down to 20 μHz. *Phys. Rev. Lett.*, 120:061101, Feb 2018. doi: 10.1103/PhysRevLett.120.061101. URL https://link.aps.org/doi/10.1103/PhysRevLett.120.061101.

[9] Carl Darius Blair. *Parametric instability in gravitational wave detectors*. PhD thesis, The University of Western Australia, 2017.

[10] D Bhattacharjee, Y Lecoeuche, S Karki, J Betzwieser, V Bossilkov, S Kandhasamy, E Payne, and R L Savage. Fiducial displacements with improved accuracy for the global network of gravitational wave detectors. *Classical and Quantum Gravity*, 38(1):015009, nov 2020. doi: 10.1088/1361-6382/aba9ed. URL https://doi.org/10.1088/1361-6382/aba9ed.

[11] Richard Savage. Procedure for upgrading pcal transmitter module layout to reduce the impact of depolarized light downstream of the aom. *DCC*, 2015. URL https://dcc.ligo.org/cgi-bin/private/DocDB/ShowDocument?.submit=Identifier&docid=T1500144&version=.

[12] Jolien D. E. (Jolien Donald Earl) Creighton. *Gravitational-wave physics and astronomy [electronic resource] : an introduction to theory, experiment and data analysis*. Wiley series in cosmology. Wiley-VCH, Weinheim, Germany, 2011. ISBN 1-283-86984-5.

[13] Peter Fritschel et al. Instrument science white paper 2021. *DCC*, pages 1–180, Jul 2021. URL https://dcc.ligo.org/LIGO-T2100298. Updated by Patrick Brady.

[14] Sir Isacc Newton. *Philosophiæ Naturalis Principia Mathematica*. Jussu Societatis Regiæ ac Typis Joseph Streater, Londini, first edition, 1687.

[15] Bernard F Schutz. *Gravity from the ground up*. Cambridge University Press, Cambridge, 2002. ISBN 0521455065.

[16] Bernard F Schutz. *A first course in general relativity*. Cambridge University Press, Cambridge, 2nd ed. edition, 2009. ISBN 9780521887052.

[17] Hugh D. Young, Roger A. Freedman, and A. Lewis Ford. *University Physics*. Addison-Wesley, San Francisco, 13 ed. edition, 2012.

[18] Charles W. Misner, Kip S. Thorne, and John A. Wheeler. *Gravitation*. Princeton University Press, first edition, 2017. Original edition published in 1973 by W.H. Freeman and Company.

[19] Eric Poisson and Clifford M. Will. *Gravity: Newtonian, Post-Newtonian, Relativistic*. Cambridge University Press, 2014. doi: 10.1017/CBO9781139507486.

[20] Edward J Daw. *A General Relativity Coursebook*. Cambridge University Press, Cambridge, 1st ed. edition, 2022. Accepted for publication communication with author.

[21] Edwin Hubble. A relation between distance and radial velocity among extragalactic nebulae. *Proceedings of the National Academy of Sciences*, 15(3): 168–173, 1929. doi: 10.1073/pnas.15.3.168. URL https://www.pnas.org/doi/abs/10.1073/pnas.15.3.168.

[22] Planck Collaboration et al. Planck 2018 results - vi. cosmological parameters. *A&A*, 641:A6, 2020. doi: 10.1051/0004-6361/201833910. URL https://doi.org/10.1051/0004-6361/201833910.

[23] Planck Collaboration et al. Planck 2018 results - i. overview and the cosmological legacy of planck. *A&A*, 641:A1, 2020. doi: 10.1051/0004-6361/201833880. URL https://doi.org/10.1051/0004-6361/201833880.

[24] R. Abbott et al. Gwtc-2: Compact binary coalescences observed by ligo and virgo during the first half of the third observing run. *Phys. Rev. X*, 11: 021053, Jun 2021. doi: 10.1103/PhysRevX.11.021053. URL https://link.aps.org/doi/10.1103/PhysRevX.11.021053.

[25] The LIGO Scientific Collaboration, The Virgo Collaboration, and The KAGRA Collaboration. Gwtc-3: Compact binary coalescences observed by ligo and virgo during the second part of the third observing run, 2021. URL https://arxiv.org/abs/2111.03606.

[26] B. P. Abbott et al. Observation of gravitational waves from a binary black hole merger. *Phys. Rev. Lett.*, 116:061102, Feb 2016. doi: 10.1103/PhysRevLett.116.061102. URL https://link.aps.org/doi/10.1103/PhysRevLett.116.061102.

[27] The Nobel Prize in Physics 2017. URL https://www.nobelprize.org/prizes/physics/2017/press-release/.

[28] B. P. Abbott et al. Multi-messenger observations of a binary neutron star merger. *The Astrophysical Journal*, 848(2):L12, oct 2017. doi: 10.3847/2041-8213/aa91c9. URL https://doi.org/10.3847/2041-8213/aa91c9.

[29] Darren J. White, E. J. Daw, and V. S. Dhillon. A List of Galaxies for Gravitational Wave Searches. *Class. Quant. Grav.*, 28:085016, 2011. doi: 10.1088/0264-9381/28/8/085016.

[30] Eric Thrane, Shivaraj Kandhasamy, Christian D. Ott, Warren G. Anderson, Nelson L. Christensen, Michael W. Coughlin, Steven Dorsher, Stefanos Giampanis, Vuk Mandic, Antonis Mytidis, Tanner Prestegard, Peter Raffai, and Bernard Whiting. Long gravitational-wave transients and associated detection strategies for a network of terrestrial interferometers. *Phys. Rev. D*, 83:083004, Apr 2011. doi: 10.1103/PhysRevD.83.083004. URL https://link.aps.org/doi/10.1103/PhysRevD.83.083004.

[31] S. J. Bell. *The measurement of radio source diameters using a diffraction method*. PhD thesis, University of Cambridge, 1968.

[32] S Klimenko, I Yakushin, A Mercer, and G Mitselmakher. A coherent method for detection of gravitational wave bursts. *Classical and Quantum Gravity*, 25 (11):114029, may 2008. doi: 10.1088/0264-9381/25/11/114029. URL https://doi.org/10.1088/0264-9381/25/11/114029.

[33] Eric Sowell, Alessandra Corsi, and Robert Coyne. Multiwaveform cross-correlation search method for intermediate-duration gravitational waves from gamma-ray bursts. *Phys. Rev. D*, 100:124041, Dec 2019. doi: 10.1103/PhysRevD.100.124041. URL https://link.aps.org/doi/10.1103/PhysRevD.100.124041.

[34] B P Abbott et al. All-sky search for long-duration gravitational wave transients in the first advanced LIGO observing run. *Classical and Quantum Gravity*, 35(6):065009, feb 2018. doi: 10.1088/1361-6382/aaab76. URL https://doi.org/10.1088/1361-6382/aaab76.

[35] B. P. Abbott et al. All-sky search for long-duration gravitational-wave transients in the second advanced ligo observing run. *Phys. Rev. D*, 99:104033, May 2019. doi: 10.1103/PhysRevD.99.104033. URL https://link.aps.org/doi/10.1103/PhysRevD.99.104033.

[36] Michele Maggiore, Chris Van Den Broeck, Nicola Bartolo, Enis Belgacem, Daniele Bertacca, Marie Anne Bizouard, Marica Branchesi, Sebastien Clesse, Stefano Foffa, Juan Garciá-Bellido, Stefan Grimm, Jan Harms, Tanja Hinderer, Sabino Matarrese, Cristiano Palomba, Marco Peloso, Angelo Ricciardone, and Mairi Sakellariadou. Science case for the einstein telescope. *Journal of cosmology and astroparticle physics*, 2020(3):50–50, 2020. ISSN 1475-7516.

[37] S. W. Hawking and W. Israel. *Three Hundred Years of Gravitation*. 1989.

[38] Peter R. Saulson. *Fundamentals of Interferometric Gravitational Wave Detectors*. World Scientific Publishing Co., 2nd edition edition, 2017.

[39] Ligo. `https://www.ligo.caltech.edu/`, . Accessed: 2022-03-26.

[40] M Agathos et al. Advanced virgo: a second-generation interferometric gravitational wave detector, 2014. ISSN 0264-9381.

[41] Virgo. `https://www.virgo-gw.eu/`. Accessed: 2022-03-26.

[42] K L Dooley et al. Geo 600 and the geo-hf upgrade program: successes and challenges. *Classical and quantum gravity*, 33(7):75009, 2016. ISSN 0264-9381.

[43] Geo 600 gravitational wave detector. `https://www.geo600.org/`. Accessed: 2022-03-26.

[44] Tama300 interferometer. `http://tamago.mtk.nao.ac.jp/spacetime/tama300_e.html`. Accessed: 2022-03-24.

[45] Mitsuru Musha, Akitoshi Ueda, Masatake Ohashi, and Ken ichi Ueda. Interferometric gravitational wave detector TAMA-300 and the frequency-stabilized laser with high-finesse optical resonator. In Alexis V. Kudryashov, editor, *Laser Resonators II*, volume 3611, pages 65 – 72. International Society for Optics and Photonics, SPIE, 1999. doi: 10.1117/12.349274. URL `https://doi.org/10.1117/12.349274`.

[46] Masaki Ando et al. Observation results by the tama300 detector on gravitational wave bursts from stellar-core collapses. *Phys. Rev. D*, 71:082002, Apr 2005. doi: 10.1103/PhysRevD.71.082002. URL `https://link.aps.org/doi/10.1103/PhysRevD.71.082002`.

[47] T Akutsu et al. The status of kagra underground cryogenic gravitational wave telescope. *Journal of physics. Conference series*, 1342(1):12014, 2020. ISSN 1742-6588.

[48] Davide Castelvecchi. Gravitational-wave observatory ligo set to double its detecting power. *Nature (London)*, 566(7744):305–305, 2019. ISSN 0028-0836.

[49] Ligo india - a gravitational wave detector on indian soil. `https://www.ligo-india.in/`, . Accessed: 2022-03-24.

[50] Tarun Souradeep. Ligo-india: An indian mega-project for gravitational-wave science. *Resonance*, 21(3):225–231, 2016. ISSN 0971-8044.

[51] M Saleem et al. The science case for ligo-india. *Classical and quantum gravity*, 39(2):25004, 2021. ISSN 0264-9381.

[52] S Araki et al. Kagra: 2.5 generation interferometric gravitational wave detector. *Nature Astronomy*, 3(1):35–40, 2019. ISSN 2397-3366.

[53] K. Danzmann. Lisa — an esa cornerstone mission for the detection and observation of gravitational waves. *Advances in Space Research*, 32(7):1233–1242, 2003. ISSN 0273-1177. doi: https://doi.org/10.1016/S0273-1177(03)90323-1. URL https://www.sciencedirect.com/science/article/pii/S0273117703903231. Fundamental Physics in Space.

[54] Matt Abernathy, F Acernese, P Ajith, B Allen, P Amaro Seoane, N Andersson, S Aoudia, P Astone, B Krishnan, L Barack, et al. Einstein gravitational wave telescope conceptual design study. 2011.

[55] K. Ackley et al. Neutron star extreme matter observatory: A kilohertz-band gravitational-wave detector in the global network. *Publications of the Astronomical Society of Australia*, 37:e047, 2020. doi: 10.1017/pasa.2020.39.

[56] R X Adhikari, P Ajith, Y Chen, J A Clark, V Dergachev, N V Fotopoulos, S E Gossan, I Mandel, M Okounkova, V Raymond, and J S Read. Astrophysical science metrics for next-generation gravitational-wave detectors. *Classical and Quantum Gravity*, 36(24):245010, nov 2019. doi: 10.1088/1361-6382/ab3cff. URL https://doi.org/10.1088/1361-6382/ab3cff.

[57] R X Adhikari et al. A cryogenic silicon interferometer for gravitational-wave detection. *Classical and Quantum Gravity*, 37(16):165003, jul 2020. doi: 10.1088/1361-6382/ab9143. URL https://doi.org/10.1088/1361-6382/ab9143.

[58] B. Abbott et al. First cross-correlation analysis of interferometric and resonant-bar gravitational-wave data for stochastic backgrounds. *Phys. Rev. D*, 76:022001, Jul 2007. doi: 10.1103/PhysRevD.76.022001. URL https://link.aps.org/doi/10.1103/PhysRevD.76.022001.

[59] J Antoniadis et al. The International Pulsar Timing Array second data release: Search for an isotropic gravitational wave background. *Monthly Notices of the Royal Astronomical Society*, 510(4):4873–4887, 01 2022. ISSN 0035-8711. doi: 10.1093/mnras/stab3418. URL https://doi.org/10.1093/mnras/stab3418.

[60] H.T Cromartie et al. Relativistic shapiro delay measurements of an extremely massive millisecond pulsar. *Nature Astronomy*, 4(1):72–76, 2020. ISSN 2397-3366.

[61] A Basu, B Shaw, D Antonopoulou, M J Keith, A G Lyne, M B Mickaliger, B W Stappers, P Weltevrede, and C A Jordan. The Jodrell bank glitch catalogue: 106 new rotational glitches in 70 pulsars. *Monthly Notices of the Royal Astronomical Society*, 510(3):4049–4062, 11 2021. ISSN 0035-8711. doi: 10.1093/mnras/stab3336. URL https://doi.org/10.1093/mnras/stab3336.

[62] Robert Braun, T Bourke, James Green, Evan Keane, and Jeff Wagg. Advancing astrophysics with the square kilometre array. page 174, 05 2015. doi: 10.22323/1.215.0174.

[63] J. P. W. Verbiest, S. Osłowski, and S. Burke-Spolaor. *Pulsar Timing Array Experiments*, pages 1–42. Springer Singapore, Singapore, 2020. ISBN 978-981-15-4702-7. doi: 10.1007/978-981-15-4702-7_4-1. URL https://doi.org/10.1007/978-981-15-4702-7_4-1. https://arxiv.org/pdf/2101.10081.pdf.

[64] M. E. Gertsenshteĭn and V. I. Pustovoĭt. On the Detection of Low-Frequency Gravitational Waves. *Soviet Journal of Experimental and Theoretical Physics*, 16:433, January 1963.

[65] B F Schutz. Gravitational wave astronomy. 16(12A):A131–A156, nov 1999. doi: 10.1088/0264-9381/16/12a/307. URL https://doi.org/10.1088/0264-9381/16/12a/307.

[66] R. W. P. Drever. *Laser Interferometer Gravitational Wave Detectors*, pages 397–412. Springer Netherlands, Dordrecht, 1984. ISBN 978-94-009-6469-3. doi: 10.1007/978-94-009-6469-3_23. URL https://doi.org/10.1007/978-94-009-6469-3_23.

[67] Pierre Meystre and Marian O Scully. *Quantum optics, experimental gravity, and measurement theory*, volume 94. Springer Science & Business Media, 2012.

[68] R. Benford, M. Burka, N. Christensen, M. Eisgruber, P. Fritschel, A. Jeffries, J. Kovalik, P. Linsay, J. Livas, P. Saulson, and R. Weiss. Progress on the MIT 5-meter interferometer. In *Experimental Gravitational Physics*, pages 312–315, January 1988.

[69] D. J. Muehlner and Rainer Weiss. Gravitation research. *Massachusetts Institute of Technology. Research Laboratory of Electronics. Quarterly Progress Report*, 105:17, Apr 1972. URL http://hdl.handle.net/1721.1/56271.

[70] Jeffrey C. Livas and Boude C. Moore. Ligo vacuum system study. *15th Space Simulation Conference: Support the Highway to Space Through Testing*, January 1988. URL https://ntrs.nasa.gov/citations/19890003228.

[71] F Matichard et al. Seismic isolation of advanced LIGO: Review of strategy, instrumentation and performance. *Classical and Quantum Gravity*, 32(18): 185003, aug 2015. doi: 10.1088/0264-9381/32/18/185003. URL https://doi.org/10.1088/0264-9381/32/18/185003.

[72] L Carbone, S M Aston, R M Cutler, A Freise, J Greenhalgh, J Heefner, D Hoyland, N A Lockerbie, D Lodhia, N A Robertson, C C Speake, K A Strain, and A Vecchio. Sensors and actuators for the advanced LIGO mirror suspensions. *Classical and Quantum Gravity*, 29(11):115005, may 2012. doi: 10.1088/0264-9381/29/11/115005. URL https://doi.org/10.1088/0264-9381/29/11/115005.

[73] MV Plissi, CI Torrie, M Barton, NA Robertson, A Grant, CA Cantley, KA Strain, PA Willems, JH Romie, KD Skeldon, et al. An investigation of eddy-current damping of multi-stage pendulum suspensions for use in interferometric gravitational wave detectors. *Review of scientific instruments*, 75 (11):4516–4522, 2004.

[74] Rich Abbott, Rana Adhikari, Stefan Ballmer, Lisa Barsotti, Matt Evans, Peter Fritschel, Valera Frolov, Guido Mueller, Bram Slagmolen, and Sam Waldman. Advligo interferometer sensing and control conceptual design. *LIGO Technical Document, T070247-01-I*, 2008.

[75] R Bork, M Aronsson, D Barker, J Batch, J Heefner, A Ivanov, R McCarthy, V Sandberg, and K Thorne. New control and data acquisition system in the advanced ligo project. In *Proc. of industrial control and large experimental physics control system (ICALEPSC) conference*, 2011.

[76] Calum I. Torrie et al. Manufacturing process for cantilever spring blades for advanced ligo. E0900023, July 2010. URL https://dcc.ligo.org/public/0000/E0900023/013/E0900023-v13_Manufacturing%20Process%20Spec%20for%20Cantilever%20Spring%20Blades.pdf. Updated by Norna Robertson.

[77] Dennis Coyne. Suspension blade spring internal modes (advanced ligo). T050078, May 2005. URL https://dcc.ligo.org/public/0027/T050078/000/T050078-01.pdf. LIGO internal technical note made public.

[78] Krishna Venkateswara, Charles A. Hagedorn, Matthew D. Turner, Trevor Arp, and Jens H. Gundlach. A high-precision mechanical absolute-rotation sensor. *Review of Scientific Instruments*, 85(1):015005, 2014. doi: 10.1063/1.4862816. URL https://doi.org/10.1063/1.4862816.

[79] B P Abbott et al. A guide to LIGO–virgo detector noise and extraction of transient gravitational-wave signals. *Classical and Quantum Gravity*, 37(5): 055002, feb 2020. doi: 10.1088/1361-6382/ab685e. URL https://doi.org/10.1088/1361-6382/ab685e.

[80] Michael Ross, Krishna Venkateswara, Conor Mow-Lowry, Sam Cooper, Jim Warner, Brian Lantz, Jeffrey Kissel, Hugh Radkins, Thomas Shaffer, Richard Mittleman, Arnaud Pele, and Jens Gundlach. Towards windproofing ligo: reducing the effect of wind-driven floor tilt by using rotation sensors in active seismic isolation. *Classical and Quantum Gravity*, 37, 09 2020. doi: 10.1088/1361-6382/ab9d5c.

[81] Michael P Ross. *Precision Mechanical Rotation Sensors for Terrestrial Gravitational Wave Observatories*. PhD thesis, University of Washington, 08 2020.

[82] Kyung-Ha Lee, Giles Hammond, James Hough, Russell Jones, Sheila Rowan, and Alan Cumming. Improved fused silica fibres for the advanced LIGO monolithic suspensions. *Classical and Quantum Gravity*, 36(18):185018, aug 2019. doi: 10.1088/1361-6382/ab28bd. URL https://doi.org/10.1088/1361-6382/ab28bd.

[83] A Heptonstall et al. Enhanced characteristics of fused silica fibers using laser polishing. *Classical and Quantum Gravity*, 31(10):105006, apr 2014. doi: 10.1088/0264-9381/31/10/105006. URL https://doi.org/10.1088/0264-9381/31/10/105006.

[84] Peter R. Saulson. Thermal noise in mechanical experiments. *Phys. Rev. D*, 42:2437–2445, Oct 1990. doi: 10.1103/PhysRevD.42.2437. URL https://link.aps.org/doi/10.1103/PhysRevD.42.2437.

[85] Clarence Zener. Internal friction in solids. i. theory of internal friction in reeds. *Phys. Rev.*, 52:230–235, Aug 1937. doi: 10.1103/PhysRev.52.230. URL https://link.aps.org/doi/10.1103/PhysRev.52.230.

[86] G. Cagnoli and P. A. Willems. Effects of nonlinear thermoelastic damping in highly stressed fibers. *Phys. Rev. B*, 65:174111, Apr 2002. doi: 10.1103/PhysRevB.65.174111. URL https://link.aps.org/doi/10.1103/PhysRevB.65.174111.

[87] A Dmitriev, S Mescheriakov, Kirill Tokmakov, and V. Mitrofanov. Controllable damping of high-q violin modes in fused silica suspension fibers. *Classical and Quantum Gravity*, 27:025009, 12 2009. doi: 10.1088/0264-9381/27/2/025009.

[88] Gregory M Harry and. Advanced LIGO: the next generation of gravitational wave detectors. *Classical and Quantum Gravity*, 27(8):084006, apr 2010. doi: 10.1088/0264-9381/27/8/084006. URL https://doi.org/10.1088/0264-9381/27/8/084006.

[89] P. Kwee, C. Bogan, K. Danzmann, M. Frede, H. Kim, P. King, J. Pöld, O. Puncken, R. L. Savage, F. Seifert, P. Wessels, L. Winkelmann, and B. Willke. Stabilized high-power laser system for the gravitational wave detector advanced ligo. *Opt. Express*, 20(10):10617–10634, May 2012. doi: 10.1364/OE.20.010617. URL http://www.osapublishing.org/oe/abstract.cfm?URI=oe-20-10-10617.

[90] I Freitag, A Tünnermann, and H Welling. Power scaling of diode-pumped monolithic nd:yag lasers to output powers of several watts. *Optics Communications*, 115(5):511–515, 1995. ISSN 0030-4018. doi: https://doi.org/10.1016/0030-4018(95)00020-9. URL https://www.sciencedirect.com/science/article/pii/0030401895000209.

[91] Thomas J. Kane and Robert L. Byer. Monolithic, unidirectional single-mode nd:yag ring laser. *Opt. Lett.*, 10(2):65–67, Feb 1985. doi: 10.1364/OL.10.000065. URL http://www.osapublishing.org/ol/abstract.cfm?URI=ol-10-2-65.

[92] L Winkelmann, O Puncken, R Kluzik, C Veltkamp, P Kwee, J Poeld, C Bogan, B Willke, M Frede, J Neumann, P Wessels, and D Kracht. Injection-locked single-frequency laser with an output power of 220 w. *Applied physics. B, Lasers and optics*, 102(3):529–538, 2011. ISSN 0946-2171.

[93] M. Tse et al. Quantum-enhanced advanced ligo detectors in the era of gravitational-wave astronomy. *Phys. Rev. Lett.*, 123:231107, Dec 2019. doi: 10.1103/PhysRevLett.123.231107. URL https://link.aps.org/doi/10.1103/PhysRevLett.123.231107.

[94] Rolf Bork, Jonathan Hanks, David Barker, Joseph Betzwieser, Jameson Rollins, Keith Thorne, and Erik von Reis. advligorts: The advanced ligo real-time digital control and data acquisition system. *SoftwareX*, 13:100619, 2021. ISSN 2352-7110. doi: https://doi.org/10.1016/j.softx.2020.100619. URL https://www.sciencedirect.com/science/article/pii/S2352711020303320.

[95] Rolf Bork. An Overview of the LIGO Control and Data Acquisition Systems (Invited). In Hamid Shoaee, editor, *Accelerator and Large Experimental Physics Control Systems*, page 19, January 2001.

[96] R Bork, M Aronsson, and A Ivanov. aligo cds real-time code generator (rcg) application developer's guide. *DCC*, 2013.

[97] Rolf Bork and Kieth Thorne. aligo cds real-time software sysadmin guide. *DCC*, 2010.

[98] Rolf Bork. Advligo cds networking architecture. *DCC*, 2014.

[99] J G Rollins. Distributed state machine supervision for long-baseline gravitational-wavedetectors. 2008. arXiv:1604.01456v2.

[100] Inc The MathWorks. Simulink simulation and model-based design - matlab & simulink, 1994-2021. URL https://uk.mathworks.com/products/simulink.html.

[101] EPICS. Epics controls. https://epics-controls.org/, 2020. Accessed: 2020-12-14.

[102] Jamie Rollins. Advanced ligo guardian documentation. *DCC*, 2014. URL https://dcc.ligo.org/LIGO-T1500292/public.

[103] CERN. Storage. What data to record?, 2022. https://home.cern/science/computing/storage.

[104] LIGO Data, Computing Group, and Virgo Data Acquisition Group. Specification of a common data frame format forinterferometric gravitational wave detectors (igwd). *DCC*, Feb 2019. URL https://dcc.ligo.org/public/0000/T970130/002/T970130-v2.pdf.

[105] The HDF Group. Hierarchical Data Format, version 5, 1997-2022. https://www.hdfgroup.org/HDF5/.

[106] LIGO Scientific Collaboration. LIGO Algorithm Library - LALSuite. free software (GPL), 2022.

[107] Alex Nitz et al. gwastro/pycbc:, August 2021. URL https://doi.org/10.5281/zenodo.5347736.

[108] Duncan Macleod. GWpy, 2022. https://gwpy.github.io/docs/v0.1/index.html.

[109] J Aasi et al. Advanced LIGO. 32(7):074001, mar 2015. doi: 10.1088/0264-9381/32/7/074001. URL https://doi.org/10.1088/0264-9381/32/7/074001.

[110] H. J. Kimble, Yuri Levin, Andrey B. Matsko, Kip S. Thorne, and Sergey P. Vyatchanin. Conversion of conventional gravitational-wave interferometers into quantum nondemolition interferometers by modifying their input and/or output optics. *Phys. Rev. D*, 65:022002, Dec 2001. doi: 10.1103/PhysRevD.65.022002. URL https://link.aps.org/doi/10.1103/PhysRevD.65.022002.

[111] Alessandra Buonanno and Yanbei Chen. Quantum noise in second generation, signal-recycled laser interferometric gravitational-wave detectors. *Phys. Rev. D*, 64:042006, Jul 2001. doi: 10.1103/PhysRevD.64.042006. URL https://link.aps.org/doi/10.1103/PhysRevD.64.042006.

[112] Herbert B. Callen and Richard F. Greene. On a theorem of irreversible thermodynamics. *Phys. Rev.*, 86:702–710, Jun 1952. doi: 10.1103/PhysRev.86.702. URL https://link.aps.org/doi/10.1103/PhysRev.86.702.

[113] Herbert B. Callen and Theodore A. Welton. Irreversibility and generalized noise. *Phys. Rev.*, 83:34–40, Jul 1951. doi: 10.1103/PhysRev.83.34. URL https://link.aps.org/doi/10.1103/PhysRev.83.34.

[114] Janyce Franc, Nazario Morgado, Raffaele Flaminio, Ronny Nawrodt, Iain Martin, Liam Cunningham, Alan Cumming, Sheila Rowan, and James Hough. Mirror thermal noise in laser interferometer gravitational wave detectors operating at room and cryogenic temperature. 12 2009.

[115] Scott A. Hughes and Kip S. Thorne. Seismic gravity-gradient noise in interferometric gravitational-wave detectors. *Phys. Rev. D*, 58:122002, Nov 1998. doi: 10.1103/PhysRevD.58.122002. URL https://link.aps.org/doi/10.1103/PhysRevD.58.122002.

[116] Peter R. Saulson. Terrestrial gravitational noise on a gravitational wave antenna. *Phys. Rev. D*, 30:732–736, Aug 1984. doi: 10.1103/PhysRevD.30.732. URL https://link.aps.org/doi/10.1103/PhysRevD.30.732.

[117] R Spero, M M Nieto, W C Haxton, C M Hoffman, E W Kolb, V D Sandberg, and J W Toevs. Science underground (los alamos, 1982). 1 1983. URL https://www.osti.gov/biblio/6305179.

[118] Kagra large-scale cryogenic gravitational wave telescope project. http://www.et-gw.eu/index.php. Accessed: 2022-03-24.

[119] T Akutsu et al. Overview of KAGRA: Calibration, detector characterization, physical environmental monitors, and the geophysics interferometer. *Progress of Theoretical and Experimental Physics*, 2021(5), 02 2021. ISSN 2050-3911. doi: 10.1093/ptep/ptab018. URL https://doi.org/10.1093/ptep/ptab018. 05A102.

[120] T Akutsu et al. Overview of KAGRA: Detector design and construction history. *Progress of Theoretical and Experimental Physics*, 2021(5), 08 2020. ISSN 2050-3911. doi: 10.1093/ptep/ptaa125. URL https://doi.org/10.1093/ptep/ptaa125. 05A101.

[121] T Akutsu et al. Overview of KAGRA: KAGRA science. *Progress of Theoretical and Experimental Physics*, 2021(5), 08 2020. ISSN 2050-3911. doi: 10.1093/ptep/ptaa120. URL https://doi.org/10.1093/ptep/ptaa120. 05A103.

[122] LIGO-India Scientific Collaboration. Ligo india - a gravitational wave detector project on indian soil, 2021. URL https://www.ligo-india.in/.

[123] M Saleem, Javed Rana, V Gayathri, Aditya Vijaykumar, Srashti Goyal, Surabhi Sachdev, Jishnu Suresh, S Sudhagar, Arunava Mukherjee, Gurudatt Gaur, Bangalore Sathyaprakash, Archana Pai, Rana X Adhikari, P Ajith, and Sukanta Bose. The science case for LIGO-india. *Classical and Quantum Gravity*, 39(2):025004, dec 2021. doi: 10.1088/1361-6382/ac3b99. URL https://doi.org/10.1088/1361-6382/ac3b99.

[124] IndIGO. Indigo, 2021. URL http://www.gw-indigo.org.

[125] O Jennrich. LISA technology and instrumentation. *Classical and Quantum Gravity*, 26(15):153001, jul 2009. doi: 10.1088/0264-9381/26/15/153001. URL https://doi.org/10.1088/0264-9381/26/15/153001.

[126] Pau Amaro-Seoane et al. Low-frequency gravitational-wave science with eLISA/NGO. *Classical and Quantum Gravity*, 29(12):124016, jun 2012. doi: 10.1088/0264-9381/29/12/124016. URL https://doi.org/10.1088/0264-9381/29/12/124016.

[127] National Research Council. *New Worlds, New Horizons in Astronomy and Astrophysics*. The National Academies Press, Washington, DC, 2010. ISBN 978-0-309-15799-5. doi: 10.17226/12951. URL https://www.nap.edu/catalog/12951/new-worlds-new-horizons-in-astronomy-and-astrophysics.

[128] T. A. Prince, P. Binétruy, J. Centrella, L. S. Finn, C. Hogan, G. Nelemans, E. S. Phinney, and B. Schutz. LISA: Probing the Universe with Gravitational Waves. In *2007 AAS/AAPT Joint Meeting*, volume 38, page 990, Seattle, United States, January 2007. AAS publications. URL http://hal.in2p3.fr/in2p3-00172922. 2007 AAS/AAPT Joint Meeting, American Astronomical Society Meeting 209, 74.01.

[129] Lisa Pathfinder. Lisa pathfinder: First steps to observing gravitational waves from space. *Journal of physics. Conference series*, 840(1):12001, 2017. ISSN 1742-6588.

[130] M. Armano et al. Sub-femto-g free fall for space-based gravitational wave observatories: Lisa pathfinder results. *Phys. Rev. Lett.*, 116:231101, Jun 2016. doi: 10.1103/PhysRevLett.116.231101. URL https://link.aps.org/doi/10.1103/PhysRevLett.116.231101.

[131] Jun Luo, Li-Sheng Chen, Hui-Zong Duan, Yun-Gui Gong, Shoucun Hu, Jianghui Ji, Qi Liu, Jianwei Mei, Vadim Milyukov, Mikhail Sazhin, Cheng-Gang Shao, Viktor T Toth, Hai-Bo Tu, Yamin Wang, Yan Wang, Hsien-Chi Yeh, Ming-Sheng Zhan, Yonghe Zhang, Vladimir Zharov, and Ze-Bing Zhou. Tianqin: a space-borne gravitational wave detector. *Classical and Quantum Gravity*, 33(3):035010, jan 2016. doi: 10.1088/0264-9381/33/3/035010. URL https://dx.doi.org/10.1088/0264-9381/33/3/035010.

[132] Wen-Rui Hu and Yue-Liang Wu. The Taiji Program in Space for gravitational wave physics and the nature of gravity. *National Science Review*, 4 (5):685–686, 10 2017. ISSN 2095-5138. doi: 10.1093/nsr/nwx116. URL https://doi.org/10.1093/nsr/nwx116.

[133] S. Kawamura and DECIGO working group. *Space gravitational wave antenna DECIGO and B-DECIGO*, pages 3254–3260. doi: 10.1142/9789811269776_0267. URL https://www.worldscientific.com/doi/abs/10.1142/9789811269776_0267.

[134] Vaishali Adya, Matthew Bailes, Carl Blair, David Blair, Johannes Eichholz, Joris van Heijningen, Eric Howell, Li Ju, Paul Lasky, Andrew Melatos, David Ottaway, and Chunnong Zhao. Ground based gravitational wave astronomy in the asian region. version 2, April 2020.

[135] The et (einstein telescope) project web site. https://gwcenter.icrr.u-tokyo.ac.jp/en/. Accessed: 2022-03-24.

[136] M Punturo et al. The einstein telescope: a third-generation gravitational wave observatory, 2010. ISSN 0264-9381.

[137] M Abernathy et al. Scientific objectives of einstein telescope. *Classical and quantum gravity*, 29(12):124013, 2012. ISSN 0264-9381.

[138] Jean-Baptiste-Joseph. Fourier. Mémoire sur la propagation de la chaleur dans les corps solides. *Nouveau Bulletin des Sciences par la Société Philomathique*, 1(6):112–116, 1807.

[139] I. Grattan-Guinness. Chapter 26 - joseph fourier, théorie analytique de la chaleur (1822). In I. Grattan-Guinness, Roger Cooke, Leo Corry, Pierre Crépel, and Niccolo Guicciardini, editors, *Landmark Writings in Western Mathematics 1640-1940*, pages 354–365. Elsevier Science, Amsterdam, 2005. ISBN 978-0-444-50871-3. doi: https://doi.org/10.1016/B978-044450871-3/50107-8. URL https://www.sciencedirect.com/science/article/pii/B9780444508713501078.

[140] Jean Baptiste Joseph Fourier. *Mémoire sur la propagation de la chaleur dans les corps solides*, volume 2 of *Cambridge Library Collection - Mathematics*, page 213–222. Cambridge University Press, 2013. doi: 10.1017/CBO9781139568159.009.

[141] Alejandro Dominguez. Highlights in the history of the fourier transform [retrospectroscope]. *IEEE pulse*, 7(1):53–61, 2016. ISSN 2154-2287.

[142] H. J. J. (Henry John James) Braddick. *Vibrations, waves and diffraction.* McGraw-Hill, London, 1965.

[143] James W Cooley and John W Tukey. An algorithm for the machine calculation of complex fourier series. *Mathematics of computation*, 19(90):249–259, 1965. ISSN 0025-5718.

[144] G. D Bergland. A guided tour of the fast fourier transform. *IEEE spectrum*, 6(7):41–52, 1969. ISSN 0018-9235.

[145] Gilbert Strang. Wavelet transforms versus fourier transforms. *Bulletin (new series) of the American Mathematical Society*, 28(2):288–305, 1993. ISSN 0273-0979.

[146] Eric W. Weisstein. Fast fourier transform, 1999-2021. URL `https://mathworld.wolfram.com/FastFourierTransform.html`. Accessed: 2021-12-28.

[147] K. M. M. Prabhu. *Window functions and their applications in signal processing*. CRC Press/Taylor & Francis, Boca Raton, [Florida], 1st edition. edition, 2014. ISBN 1-351-83227-1.

[148] R. Moses and P. Stoica. Pearson Education Inc., 1st edition. edition, 2005.

[149] Steven M Kay. *Modern spectral estimation : theory and application*. Prentice Hall signal processing series. Prentice Hall, Englewood Cliffs, N.J., 1988. ISBN 013598582X.

[150] S. Lawrence Marple. *Digital spectral analysis : with applications*. Prentice-Hall signal processing series. Prentice-Hall ; Prentice-Hall International, Englewood Cliffs : London, 1987. ISBN 0132141493.

[151] Floyd Martin Gardner. *Phaselock techniques*. Wiley, Hoboken, N.J. ; Chichester, 3rd ed. edition, 2005. ISBN 9780471430636.

[152] Brian W Kernighan. *The C programming language*. Prentice Hall, Englewood Cliffs, N.J., 2nd ed. edition, 1988. ISBN 9780131103627.

[153] Charles R Harris et al. Array programming with numpy. *Nature (London)*, 585(7825):357–362, 2020. ISSN 0028-0836.

[154] Ross Kennedy. *Line tracking applications for Gravitational Wave data and searching for long-duration burst signals*. PhD thesis, 2018.

[155] A V Cumming, B Sorazu, E Daw, G D Hammond, J Hough, R Jones, I W Martin, S Rowan, K A Strain, and D Williams. Lowest observed surface and weld losses in fused silica fibres for gravitational wave detectors. *Classical and Quantum Gravity*, 37(19):195019, sep 2020. doi: 10.1088/1361-6382/abac42. URL `https://doi.org/10.1088/1361-6382/abac42`.

[156] Ross Kennedy. Line tracking applications for gravitational wave data and searching for long-duration burst signals. December 2018. URL `https://etheses.whiterose.ac.uk/23103/`.

[157] Aidan F Brooks, Benjamin Abbott, Muzammil A Arain, Giacomo Ciani, Ayodele Cole, Greg Grabeel, Eric Gustafson, Chris Guido, Matthew Heintze, Alastair Heptonstall, Mindy Jacobson, Won Kim, Eleanor King, Alexander Lynch, Stephen O'Connor, David Ottaway, Ken Mailand, Guido Mueller, Jesper Munch, Virginio Sannibale, Zhenhua Shao, Michael Smith, Peter Veitch, Thomas Vo, Cheryl Vorvick, and Phil Willems. Overview of advanced ligo adaptive optics. *Applied optics (2004)*, 55(29):8256–8265, 2016. ISSN 1559-128X.

[158] A. Paolone, E. Placidi, E. Stellino, M.G. Betti, E. Majorana, C. Mariani, A. Nucara, O. Palumbo, P. Postorino, I. Rago, F. Trequattrini, M. Granata, J. Teillon, D. Hofman, C. Michel, A. Lemaitre, N. Shcheblanov, G. Cagnoli, and F. Ricci. Effects of the annealing of amorphous ta2o5 coatings produced by ion beam sputtering concerning the effusion of argon and the chemical composition. *Journal of Non-Crystalline Solids*, 557: 120651, 2021. ISSN 0022-3093. doi: https://doi.org/10.1016/j.jnoncrysol.2021.120651. URL https://www.sciencedirect.com/science/article/pii/S0022309321000107.

[159] Aidan F Brooks, David Hosken, Jesper Munch, Peter J Veitch, Zewu Yan, Chunnong Zhao, Yaohui Fan, Li Ju, David Blair, Phil Willems, Bram Slagmolen, and Jerome Degallaix. Direct measurement of absorption-induced wavefront distortion in high optical power systems. *Applied Optics*, 48(2): 355–364, 2009. ISSN 1559-128X.

[160] M. Evans, L. Barsotti, and P. Fritschel. A general approach to optomechanical parametric instabilities. *Physics Letters A*, 374(4):665–671, 2010. ISSN 0375-9601. doi: https://doi.org/10.1016/j.physleta.2009.11.023. URL https://www.sciencedirect.com/science/article/pii/S0375960109014558.

[161] Carl Blair, Yuri Levin, and Eric Thrane. Constraining temperature distribution inside ligo test masses from frequencies of their vibrational modes. *Phys. Rev. D*, 103:022003, Jan 2021. doi: 10.1103/PhysRevD.103.022003. URL https://link.aps.org/doi/10.1103/PhysRevD.103.022003.

[162] Mitchell Schiworski, Vladimir Bossilkov, Carl Blair, Daniel Brown, Aaron Jones, David Ottaway, and Chunnong Zhao. Observing the optical modes of parametric instability. Workingpaper, arXiv, United States, January 2022.

[163] Terra Christine Hardwick. *High Power and Optomechanics in Advanced LIGO Detectors*. PhD thesis, Louisiana State University, 2019. URL https://digitalcommons.lsu.edu/gradschool_dissertations/5107.

[164] S. Biscans, S. Gras, C. D. Blair, J. Driggers, M. Evans, P. Fritschel, T. Hardwick, and G. Mansell. Suppressing parametric instabilities in ligo using low-noise acoustic mode dampers. *Phys. Rev. D*, 100:122003, Dec 2019. doi: 10.1103/PhysRevD.100.122003. URL https://link.aps.org/doi/10.1103/PhysRevD.100.122003.

[165] Gabriele Vajente et al. Point absorbers in advanced ligo. *Applied optics (2004)*, 60(13):4047–4063, 2021. ISSN 1559-128X.

[166] H Wang, C Blair, M Dovale Álvarez, A Brooks, M F Kasprzack, J Ramette, P M Meyers, S Kaufer, B O'Reilly, C M Mow-Lowry, and A Freise. Thermal modelling of advanced LIGO test masses. 34(11):115001, may 2017. doi: 10.1088/1361-6382/aa6e60. URL https://doi.org/10.1088/1361-6382/aa6e60.

[167] Matthew Evans, Slawek Gras, Peter Fritschel, John Miller, Lisa Barsotti, Denis Martynov, Aidan Brooks, Dennis Coyne, Rich Abbott, Rana X. Adhikari, Koji Arai, Rolf Bork, Bill Kells, Jameson Rollins, Nicolas Smith-Lefebvre, Gabriele Vajente, Hiroaki Yamamoto, Carl Adams, Stuart Aston, Joseph Betzweiser, Valera Frolov, Adam Mullavey, Arnaud Pele, Janeen Romie, Michael Thomas, Keith Thorne, Sheila Dwyer, Kiwamu Izumi, Keita Kawabe, Daniel Sigg, Ryan Derosa, Anamaria Effler, Keiko Kokeyama, Stefan Ballmer, Thomas J. Massinger, Alexa Staley, Matthew Heinze, Chris

Mueller, Hartmut Grote, Robert Ward, Eleanor King, David Blair, Li Ju, and Chunnong Zhao. Observation of parametric instability in advanced ligo. *Phys. Rev. Lett.*, 114:161102, Apr 2015. doi: 10.1103/PhysRevLett.114.161102. URL https://link.aps.org/doi/10.1103/PhysRevLett.114.161102.

[168] Tega Boro Edo. *Advances in Ptychography*. PhD thesis, 2011.

[169] J Berliner, P Daveloza, R Savage, and J Gleason. Photon calibrator final design. December 2014. LIGO Document T1100068.

[170] I.S Sil'vestrov, V.F Fateev, and R.A Davlatov. Methods for the calibration of space-gravity gradiometers. *Measurement techniques*, 63(1):1–6, 2020. ISSN 0543-1972.

[171] K Agatsuma et al. Calibration of advanced virgo and reconstruction of the gravitational wave signal h(t) during the observing run o2. *Classical and quantum gravity*, 35(20):1–18, 2018. ISSN 0264-9381.

[172] D Estevez, B Mours, and T Pradier. Newtonian calibrator tests during the virgo o3 data taking. *Classical and Quantum Gravity*, 38(7):075012, mar 2021. doi: 10.1088/1361-6382/abe2da. URL https://doi.org/10.1088/1361-6382/abe2da.

[173] Yuki Inoue, Sadakazu Haino, Nobuyuki Kanda, Yujiro Ogawa, Toshikazu Suzuki, Takayuki Tomaru, Takahiro Yamanmoto, and Takaaki Yokozawa. Improving the absolute accuracy of the gravitational wave detectors by combining the photon pressure and gravity field calibrators. *Phys. Rev. D*, 98:022005, Jul 2018. doi: 10.1103/PhysRevD.98.022005. URL https://link.aps.org/doi/10.1103/PhysRevD.98.022005.

[174] K Holtz. B&k pulse mtc hammer instructions. *DCC*, June 2011. URL https://dcc.ligo.org/LIGO-T1100331/public.

[175] J Kissel. The ligo newtonian gravitational calibrator says hello, krishna says goodbye. https://alog.ligo-wa.caltech.edu/aLOG/index.php?callRep=50512. LHO ALOG 50512.

[176] LTD SOKKIA TOPCON CO. Setx. sokkia classic. 2009. LIGO Document T1100054.

[177] T Mistry, J Kissel, M P Ross, and L Datrier. Ncal prototype h1 surveying distance measurement. Aug 2020. LIGO Document T2000417.

[178] LTD SOKKIA TOPCON CO. *SETX Total Station Operator Manual*. 260-63 HASE, ATSUGI, KANAGAWA, 243-0036 JAPAN, 2 edition, 2007.